Composition and Chemistry of Pd-Ni-Co Thin Film Alloys for Hydrogen Related Applications

vorgelegt von

Diplom-Chemiker
Julius Kühn

geb. in Hennigsdorf

von der Fakultät II - Mathematik und Naturwissenschaften
der Technischen Universität Berlin
zur Erlangung des akademischen Grades

Doktor der Naturwissenschaften
- Dr. rer. nat. -

genehmigte Dissertation

Promotionsausschuss:

Vorsitzender: Prof. Dr. Thomas Friedrich
Gutachter: Dr. Wolfgang E. S. Unger (BAM)
Gutachter: Prof. Dr. Thorsten Ressler

Tag der wissenschaftlichen Aussprache: 02. November 2015

Berlin 2016

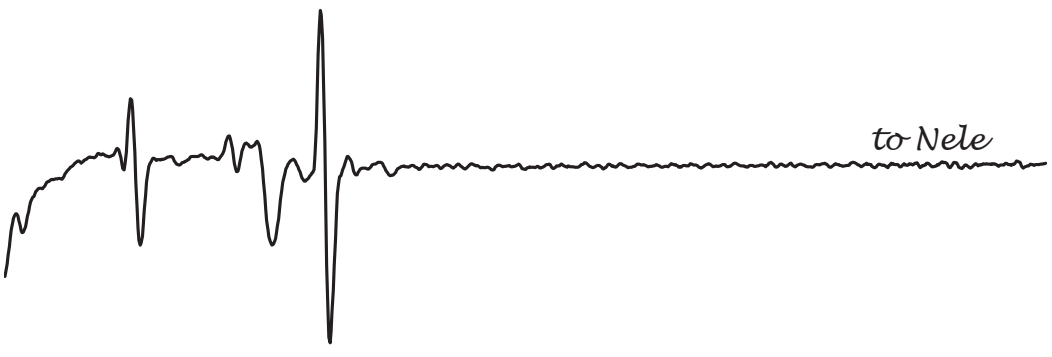
to Nele

Abstract

The discovery and design of high performance Pd-alloys is of great interest for the use of hydrogen as a future energy carrier. Therefore hydrogen has to be detected, separated from other gases and stored. In this respect this thesis presents the combinatorial synthesis and characterization of the ternary Pd-Ni-Co alloy system over a wide composition range based on so-called thin film alloy libraries. Those libraries are model systems to characterize a large number of alloy compositions at the same time. The sputter-deposition process is optimized for the gradient of the Pd concentration on the surface of the alloy library by the use of electron-excited Auger electron spectroscopy. The scientific goal of this work is the experimental investigation of adsorbate-induced surface segregation phenomena on alloy libraries. The surface and bulk compositions of an alloy library are studied after deposition, H_2 exposure and H_2S poisoning. The co-segregation of Ni and Co to the surface is observed. The segregation process is influenced by the oxidation of Ni and Co due to the contact with ambient air, by H_2 and by H_2S poisoning. Also at very high Pd concentrations in the range of 87 at.% to 97 at.%, which is interesting for the detection of very low H_2-concentrations in air, the co-segregation of Ni and Co takes place. The poisoning effects were investigated in detail on a pre-selected Pd-Ni-Co alloy by photoelectron spectroscopy (XPS, HAXPES) in addition to AES and EDX. The composition profile of the alloy on the nm scale is acquired and the surface and bulk chemistry is discussed before and after poisoning. The composition of the alloy only changed within the first 3 nm due to H_2S exposure. In the ternary Pd-Ni-Co alloy system Pd is present in its metallic state, while Ni and Co show several oxidation states. The presented concepts of ternary alloy development pave the way for the systematic synthesis and characterization of new ternary transition metal alloy systems.

Kurzfassung

Die Entwicklung leistungsfähiger Pd-Legierungen ist von großem Interesse für den Einsatz von Wasserstoff als Energieträger der Zukunft. Dafür muss Wasserstoff detektiert, von anderen Gasen getrennt und gespeichert werden. In diesem Zusammenhang verfolgt diese Arbeit die kombinatorische Synthese und Charakterisierung des ternären Pd-Ni-Co Legierungssystems über einen weiten Konzentrationsbereich basierend auf sogenannten Legierungsbibliotheken. Solche Bibliotheken dienen als Modellsysteme um möglichst viele Legierungskompositionen gleichzeitig zu charakterisieren. Der Herstellungsprozess ist mit Hilfe der elektronenangeregten Auger-Elektronspektroskopie hinsichtlich des Gradienten der Palladium-Konzentration an der Oberfläche der Legierungsbibliothek optimiert worden. Ein weiteres Ziel dieser Arbeit bestand darin, adsorbat-induzierte Oberflächensegregationsphänomene an diesen Legierungsbibliotheken experimentell zu untersuchen. Die Zusammensetzung der Legierungsbibliotheken wurde an der Oberfläche und im Volumen nach der Herstellung, nach der Behandlung mit H_2 und nach der Vergiftung mit H_2S untersucht. Die Segregation von Ni und Co zur Oberfläche wurde über den gesamten untersuchten Konzentrationsbereich beobachtet. Der Oberflächensegregationsprozess wird durch Wasserstoff und Schwefelwasserstoff beeinflusst und hängt mit der Oxidation von Ni und Co durch Luftsauerstoff zusammen. Auch bei sehr hohen Pd Konzentrationen zwischen 87 at.% und 97 at.%, interessant für die Wasserstoffdetektion an Luft, ließ sich die Segregation von Ni und Co beobachten. Ein besonderes Augenmerk lag auf der Vergiftung einer vorausgewählten Pd-Ni-Co Legierung. Diese wurde zusätzlich zu AES und EDX mit Methoden der Photoelektronenspektroskopie (XPS, HAXPES) untersucht. Das tiefenabhängige Zusammensetzungsprofil der Legierung vor und nach der Vergiftung konnte so aufgenommen und ein Einblick in die Oberflächen- und Volumenchemie des Systems gewonnen werden. Die Vergiftung veränderte die Legierungskomposition nur innerhalb der ersten 3 nm. Die gezielte Methodenkombination in dieser Arbeit ermöglicht eine umfassende und zerstörungsfreie Charakterisierung von ternären Legierungsbibliotheken und die Untersuchung von Oberflächensegregationsphänomenen.

Contents

1 Introduction

Pd-alloys are of great interest for the upcoming hydrogen economy [1]. Palladium itself has the unique ability to dissociatively absorb molecular H_2 on its surface and the very high diffusion rate of hydrogen atoms through its bulk even at room temperature and 1 atm [2]. Alloying palladium with other transition metals is a promising approach, because alloys often display properties superior of their individual components. Pd-alloys are employed for hydrogen separation membranes [2–4], solid-state hydrogen storage [5, 6], and are replacing expensive Pt-catalysts in fuel cells [7]. For example H_2S exposure causes about 80 % reduction of the hydrogen flux through a pure Pd membrane. Morreale *et al.* and Howard *et al.* reported that there is less than 10 % reduction of the hydrogen flux through $Pd_{70}Cu_{30}$ and $Pd_{45}Cu_{55}$ membranes [8, 9].

The study of single alloy compositions is a very time consuming task. For this reason in recent years combinatorial approaches and high-throughput screening methods have been developed in materials science [10–12]. A useful strategy is the combinatorial approach of depositing alloy libraries, from which a wide range of alloy compositions with respect to fixed processing parameters can be screened [13, 14].

An important characteristic of all alloys is that segregation of one or more components to the alloy surface causes the surface composition to differ significantly from the bulk composition. Surface segregation is a complex function of bulk composition and environmental factors such as temperature, pressure and the presence of gas molecules which can be adsorbed and react on the surface. Therefore, it is of great fundamental and technological interest to investigate this process in detail. An example for the screening of a binary Pd alloy system is given by Priyadarshini *et al.*, who investigated the surface segregation in binary Cu_xPd_{100-x} alloy over the continuous composition range from X_{Pd} = 5 - 95 at.% by high-throughput screening at equilibrium conditions [15]. Miller *et al.* investigated the surface segregation in the presence of adsorbed sulfur on binary Pd-Cu alloy libraries [16].

The starting point for the experiments in this thesis is the development of a design strategy for a ternary Pd-alloy for the improvement of a Pd-based hydrogen sensor [17]. The goal of alloying Pd with Ni and Co is to improve resistance of the hydrogen sensor against poisoning resulting in a stable sensor response and an increased sensor life time. From a previous high-throughput screening hydrogen sensitivity study on a Pd-Ni-Co alloy library the question aroused, if surface segregation phenomena occur under these experimental conditions and lead to sensitivity changes [18]. With the availability of powerful analytical methods such as electron excited Auger Electron Spectroscopy (AES), (Hard) X-Ray Photoelectron Spectroscopy (XPS, HAXPES), Energy-Dispersive X-ray spectroscopy (EDX) surface segregation phenomena of thin film alloys can be addressed. Thereby the determination of the surface and bulk composition of an alloy is the first step in understanding its chemistry.

In this thesis a combinatorial approach of quantitative high-throughput screening has been applied to study adsorbate-induced surface segregation phenomena on Pd-Ni-Co thin film alloy libraries related to air exposure, hydrogen exposure and hydrogen sulfide poisoning. The composition and chemistry of the Pd-Ni-Co thin film alloy system in form of alloy libraries is investigated systematically. Methods of surface (AES) and thin film analysis (EDX) are testified for their applicability to address these phenomena by the combinatorial approach of thin film alloy libraries. The deposition of alloy libraries with two different dc-magnetron sputter setups is presented. An AES high-throughput screening procedure is applied for compositional analysis of the surface. EDX is used together with the STRATAGEM software for thin films to screen the bulk composition. Both methods are combined to reveal adsorbate-induced surface segregation phenomena in the Pd-Ni-Co thin film alloy system. In addition to the high-throughput screening experiments photoelectron spectroscopy in the soft and hard X-ray range is used to address the surface, the surface near and the bulk composition and chemistry. A compositional and chemical depth profile on the nanometer scale of a single alloy is presented before and after poisoning. The thesis contributes to the fields of combinatorial materials science, surface and thin film analysis, adsorbate-induced surface segregation phenomena and ternary Pd-alloys for hydrogen related applications.

2 Pd-Ni-Co thin film alloy libraries

The thesis was based on a collaborative DFG project with the Chemical Sensor group at Humboldt-Universität zu Berlin (HUB). The samples were prepared at HUB and analyzed at BAM. Pd-Ni-Co thin films were deposited as composition spread alloys, so called alloy libraries. That means on one sample a range of ternary alloy compositions is deposited with a gradient. Samples from two different magnetron sputter deposition setups were investigated. Deposition setup 1 was operated by S. Linke and deposition setup 2 by Dr. K. Nörthemann [19]. In the following the sample systems produced with both sputter setups are presented.

2.1 Deposition setup 1: one magnetron sputter source

Ternary Pd-Ni-Co thin film alloy libraries were produced by magnetron dc-co-sputtering using a single mosaic sputter target equipped with Pd, Ni and Co. The setup is shown schematically in Figure 2.1 (a) together with the ternary plot of the deposited alloy compositions (b).

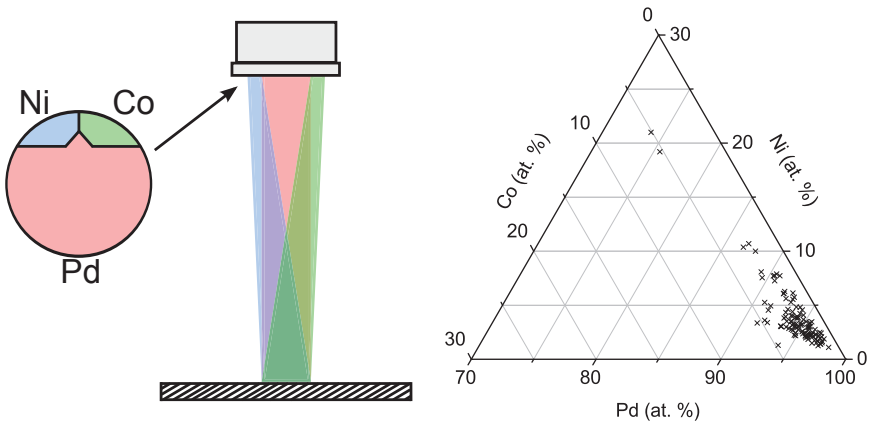

(a) (b)

Figure 2.1: Deposition setup 1: (a) Illustration of the magnetron dc-co-sputtering setup with a mosaic target of Pd, Ni and Co, (b) ternary plot of the deposited alloy compositions based on Auger electron spectroscopy.

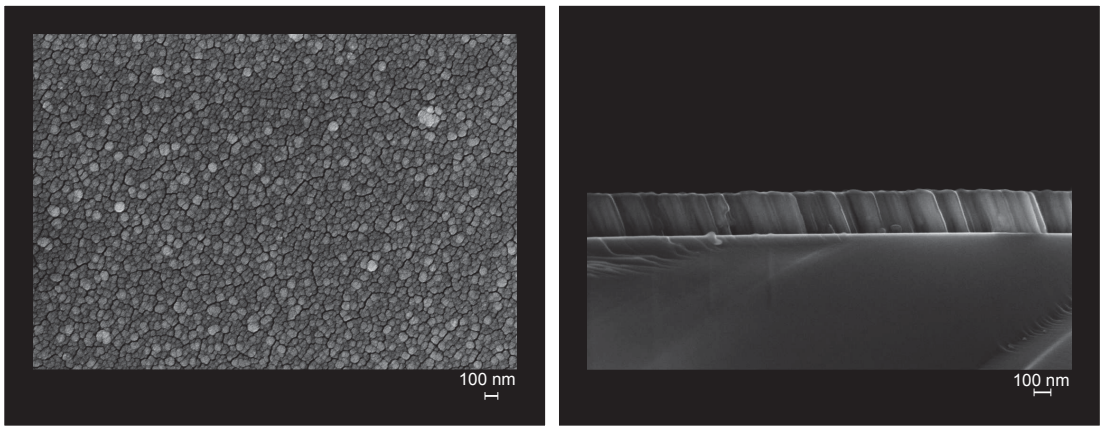

(a) (b)

Figure 2.2: (a) SEM micrograph of the surface of a Pd-Ni-Co alloy layer deposited with setup 1. (b) SEM micrograph of the cross section of a Pd-Ni-Co thin film alloy layer on Si after fracture.

The composition range accessible with this setup is limited to Pd-rich alloys from 75-97 at.%, and a Ni content from 1-21 at.% and Co from 1-5 at.%. The gradient in composition depends on the position of the substrate relative to the sputter source. The three elements are deposited at the same time on the substrate at room temperature under high vacuum conditions. The alloy libraries were deposited on single crystalline (100) silicon wafers with a size of 2.5 x 2.5 cm^2 to optimize the composition range. The native oxide layer on the Si substrate was removed by HF treatment before deposition. The surface morphology of the deposited Pd-Ni-Co alloy layer can be seen in Figure 2.2 (a). The grain size is smaller than 100 nm. A SEM image of the cross section of the alloy layer on a silicon wafer after fracture is shown in Figure 2.2 (b). From the cross section image the thickness of the alloy layer is verified. Electron excited Auger electron spectroscopy (AES) has been used for the optimization of the composition of the ternary alloy libraries. After compositional optimization Pd-Ni-Co thin film alloy libraries were deposited on a special multilayer substrate: $LaF_3/Si_3N_4/SiO_2/Si$. The tailored multilayer substrate was developed for gas sensor applications by the Chemical Sensor group at HUB over the last two decades. In the configuration with Pd as catalytically active gate metal it is used as a hydrogen sensor [17]. In this project the Pd layer was replaced by the Pd-Ni-Co alloy layer to investigate the hydrogen sensor performance depending on the alloy composition [18, 19]. A detailed TEM study was carried out on a cross section of the multilayer based on a TEM lamella prepared by the focused ion beam (FIB) technique. The TEM study was carried out by Dr. I. Dörfel at BAM, Division 5.1.

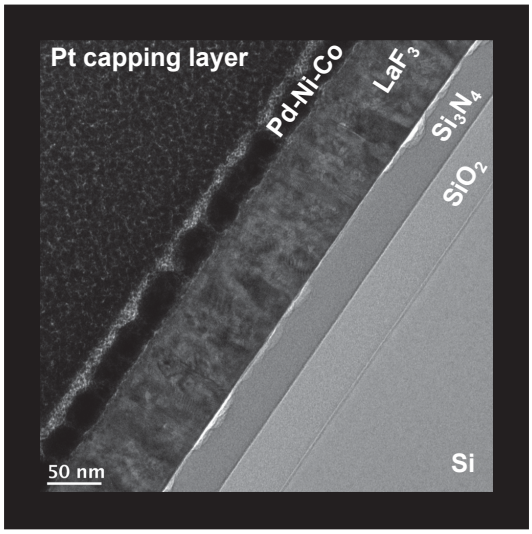

Figure 2.3: TEM image of the sensor device with Pt capping layer necessary for FIB preparation. The Pd-Ni-Co layer is on top of a $LaF_3/Si_3N_4/SiO_2/Si$ multilayer substrate developed for hydrogen sensing purposes.

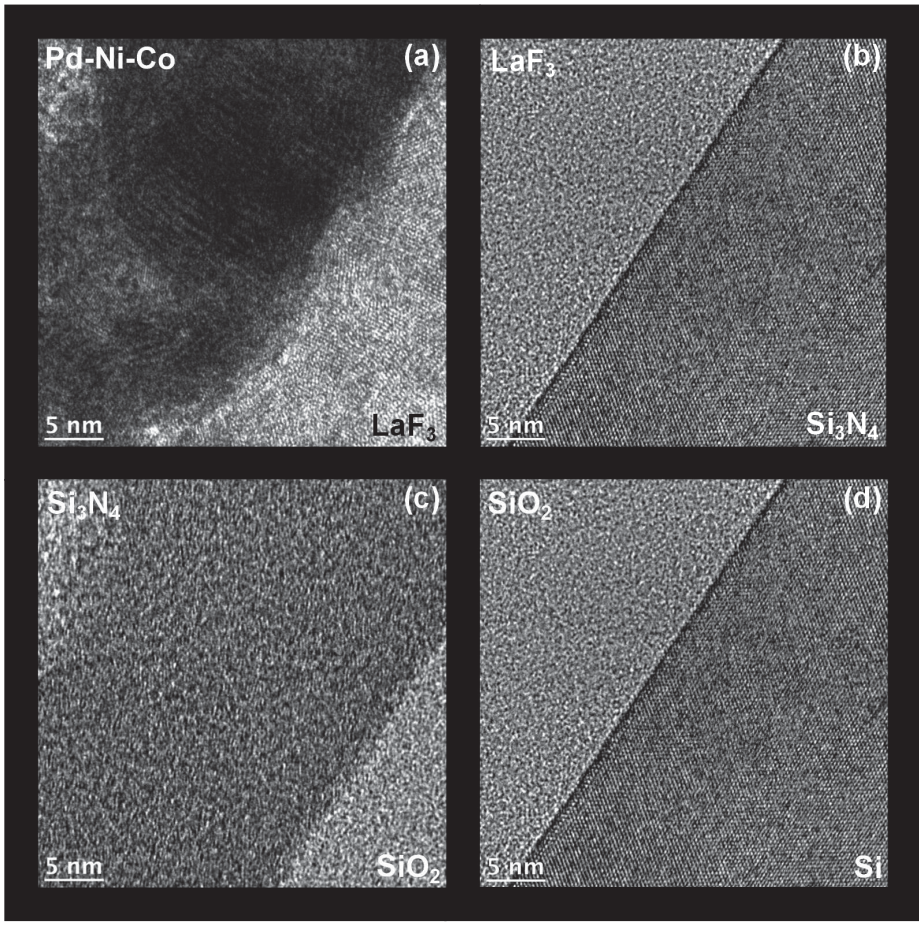

Figure 2.4: High resolution TEM images of the interfaces (a-d) within the multilayer hydrogen sensor configuration Pd-Ni-Co/$LaF_3/Si_3N_4/SiO_2$/Si.

Figure 2.3 shows the Pd-Ni-Co layer on top of the multilayer substrate. The interfaces of the layer stack are shown with higher resolution in Figure 2.4 (a-d). A Pt capping layer was deposited to protect the sample surface during FIB preparation. The Pd alloy layer thickness is in between 28 nm to 35 nm and the size of the crystallites ranges from 10 nm to more than 20 nm. The top of the alloy layer and also its interface to LaF_3 is rippled. The LaF_3 layer thickness is about 90 nm and polycrystalline with crystallite sizes from 10 nm to 30 nm. The LaF_3/Si_3N_4 interface is rather flat. The Si_3N_4 layer is amorphous with a thickness of about 44 nm. Its interface to the SiO_2 layer is flat without defects. The SiO_2 layer has a thickness of 50 nm, is amorphous, has no defects and the interface to Si is flat.

Samples deposited with setup 1 were used for the ED-EPMA/STRATAGEM study presented in Chapter 7 and for the high-throughput surface segregation study by AES in Section 8.2.

2.2 Deposition setup 2: three magnetron sputter sources

A second sputter deposition setup was commissioned during this project. The UHV-sputter deposition setup 2 is equipped with three independent magnetron sputter sources and was designed by Bestec GmbH, Berlin, Germany. The deposition of pure metal films, binary films and ternary films is possible with that setup. The commissioning of setup 2 started with the deposition of pure metal films from each sputter source to optimize the sputter spot size and their overlap on the substrate for

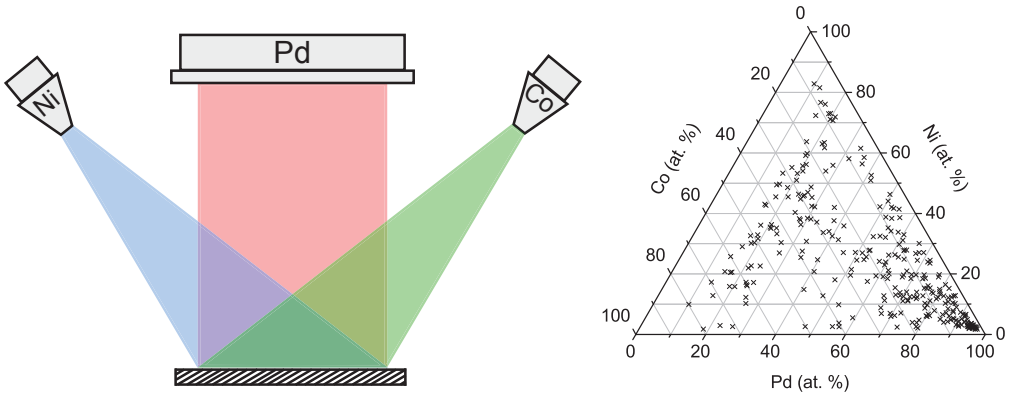

(a) (b)

Figure 2.5: Deposition setup 2: (a) illustration of the UHV-sputter setup by Bestec, (b) ternary plot of the deposited alloy compositions based on Auger electron spectroscopy.

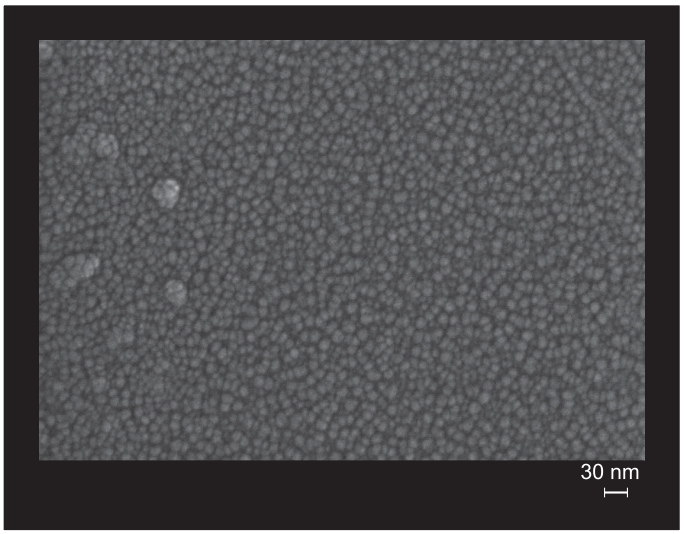

Figure 2.6: Surface SEM image of a Pd-Ni-Co alloy thin film from deposition setup 2.

the deposition of ternary alloys. Deposition setup 2 is shown schematically in Figure 2.5 (a). The Pd-Ni-Co alloy compositions deposited in this project are shown in the ternary plot in Figure 2.5 (b). The deposition of ternary alloys over the whole composition range is possible with deposition setup 2. The sputter process was optimized on a sample size of 2.5 x 3.0 cm^2 with a maximized composition range.

Polycrystalline Pd-Ni-Co thin film alloy libraries have been deposited on single crystalline silicon (100) wafers under UHV conditions at room temperature. The native oxide layer of the substrate has been removed by a HF treatment before deposition. The sputter system has three magnetron sputter sources, one for each metal: a 6" Pd source and two 2" sources for Ni and Co, respectively. The 6" source manipulator allows a manual height adjustment of 100 mm and the 2" sources a manual height adjustment of 150 mm and a tilt up to 30°. The sources can be used simultaneously and during deposition the substrate can be rotated and heated. The surface morphology of the ternary alloys can be seen in Figure 2.6. The quality of the films in terms of their surface morphology and roughness is similar to the films deposited with setup 1 but the grain size is somewhat smaller than 30 nm.

Samples deposited with deposition setup 2 were used for the high-throughput screening study on the surface and bulk composition by AES and EDX in Section 8.1 and for the compositional and chemical depth profiling study in Chapter 9.

3 Electron excited Auger electron spectroscopy

Auger Electron Spectroscopy (AES) is an ultra-high vacuum (UHV) based analytical technique used to determine the elemental composition in the outermost surface region of a solid material qualitatively and quantitatively [20–24].

In an Auger electron spectrum the number of detected electrons is plotted as a function of their kinetic energy. All elements, except hydrogen and helium, can be identified. The concentration of an element is related to the Auger peak intensity. The interaction of an incident electron beam with a solid sample is illustrated in Figure 3.1, which shows the regions where characteristic Auger electrons, secondary electrons, backscattered electrons, and X-ray photons emerge. The size and shape

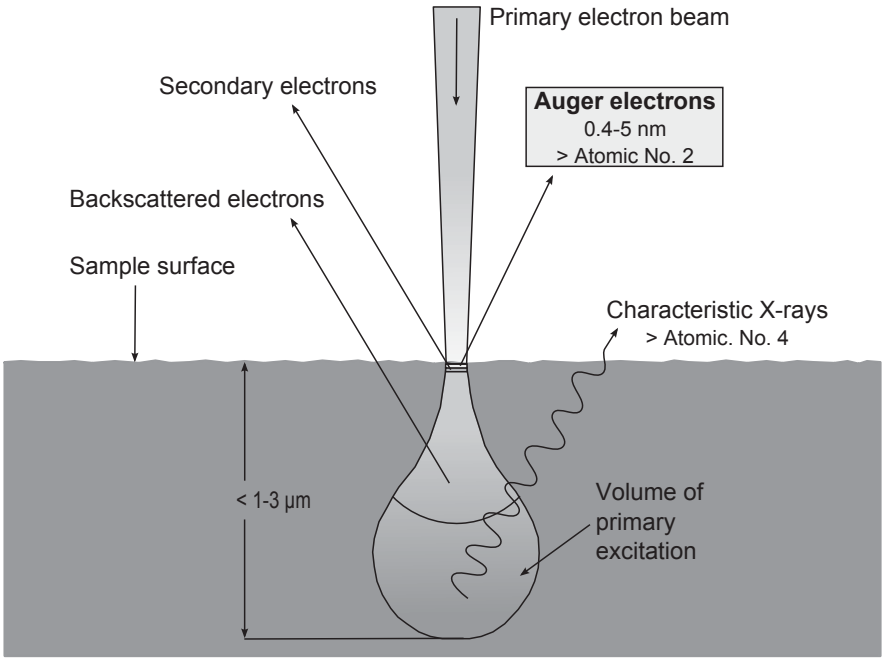

Figure 3.1: The interaction between an incident electron beam and a solid sample: Auger electrons, secondary electrons, backscattered electrons and X-ray fluorescence.

of this interaction volume is dependent on the primary beam energy and the sample material. The teardrop (or pear) shape is typical for high primary electron energies incident on low atomic number materials. As the atomic number increases or the electron energy decreases, the interaction volume is reduced and appears more like a sphere subtended by the surface. Electrons emitted in the solid must be transported to the surface in order to escape the solid and to be analyzed. Such electrons may undergo scattering events by interaction with the electrons in the solid. These interactions depend on the energy of the transported electron and on the matrix electron density. The surface sensitivity of AES arises from the relatively short inelastic mean free path (IMFP) of Auger electrons.

3.1 The Auger process

The description of the Auger process goes back to the 1920s, when Pierre Auger explained the radiationless relaxation of ionized atoms observed in cloud chambers [25–28]. The process was independently discovered by Lise Meitner around the same time [29]. The Auger electron emission process is imagined as a three-stage process. The emission is initiated, e.g. by electron impact which leads to the creation of an ion with an inner shell vacancy. In this process an electron from a higher lying energy level fills the inner shell vacancy. This simultaneous relaxation results in a final state with two vacancies. Auger electron emission is one of two relaxation mechanisms possible in an ionized atom. The other is X-ray fluorescence, in which a photon is emitted. The KL_2L_3 Auger transition is illustrated in the energy level diagrams in Figure 3.2. All energies are referenced to the Fermi level, E_f, equal to zero binding energy. In these diagrams the initial ionization occurs in the K-level, Figure 3.2 (a). The incident particle is any particle that ionizes the K-level, e.g. electrons, X-ray photons, ions or positrons. In AES instruments typically electron beams are used which can be focused to very small diameters. Following the core level ionization, an electron from the L_2-level fills the vacancy in the K-level, Figure 3.2 (b). The relaxation releases energy equal to the difference in binding energy between the K-level and the L_2-level. The energy is sufficient enough to excite an electron out of the L_3-level and leaving the atom in a doubly ionized state, Figure 3.2 (c). The Auger electron emission competes with the X-ray fluorescence process, illustrated in Figure 3.2 (d). A simple Auger transition takes place on the femtosecond timescale.

The sum of the total Auger electron yield and the fluorescence yield is unity, since an excited ion can relax by either Auger electron emission or X-ray emission. The

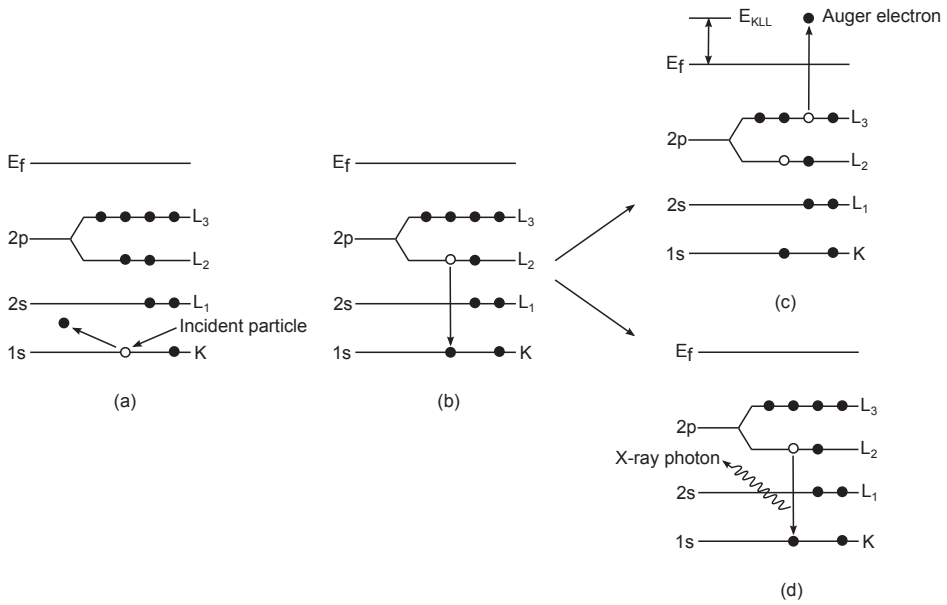

Figure 3.2: Illustration of the KL_2L_3 Auger process: (a) Creation of an inner shell vacancy, ionization of the K-level, (b) relaxation of an electron from a higher lying energy level, L_2, (c) emission of an Auger electron from the L_3-level, (d) emission of an X-ray photon.

Auger electron emission is the more probable decay mechanism for low energy transitions, e.g. for low atomic number elements with initial vacancies in the K shell and for all elements with initial vacancies in the L or M shells. Auger electron emission occurs also in X-ray photoelectron spectroscopy as a result of the photoelectric effect (Chapter 5). Auger transitions are typically labeled by the energy levels of the electrons involved, using the X-ray spectroscopy notation given in Table 3.1. The first label corresponds to the energy level of the initial core hole. The second and third labels refer to the initial energy levels of the two electrons involved in the Auger transition. Thus the Auger transition shown in Figure 3.2 is named KL_2L_3. Sometimes the energy levels are very close and not resolvable in the measurement, e.g. the Pd $M_5N_{4,5}N_{4,5}$ transition, where the energy levels are separated by comma. The kinetic energy of an Auger electron depends on the binding energies of the levels involved and not on the energy of the incident beam. But the electron beam energy has to be at least sufficient enough for the ionization of the atom. For the KL_2L_3 transition the Auger kinetic energy, E_{kin}, is given by the difference in binding energies, E_b, of energy levels K, L_2 and L_3:

$$E_{kin}(KL_2L_3) \approx E_b(K) - E_b(L_2) - E_b(L_3) \tag{3.1}$$

X-ray Spectroscopy	Optical Spectroscopy
N_7	$4f_{7/2}$
N_6	$4f_{5/2}$
N_5	$4d_{5/2}$
N_4	$4d_{3/2}$
N_3	$4p_{3/2}$
N_2	$4p_{1/2}$
N_1	4s
M_5	$3d_{5/2}$
M_4	$3d_{3/2}$
M_3	$3p_{3/2}$
M_2	$3p_{1/2}$
M_1	3s
L_3	$2p_{3/2}$
L_2	$2p_{1/2}$
L_1	2s
K	1s

Table 3.1: The X-ray notation, used for the Auger electrons and optical spectroscopy notation, used for photoelectrons, for the first four electron shells (K, L, M, N).

In this simple form contributions from the interaction energy between the holes in the L_2 and L_3 levels, as well as intra-atomic and extra-atomic relaxation are neglected. A general empirical expression for the calculation of an Auger transition has been suggested by Chung and Jenkins [30]:

$$E_{ABC}(Z) = E_A(Z) - \frac{1}{2}[E_B(Z) + E_B(Z+1)] - \frac{1}{2}[E_C(Z) + E_C(Z+1)] \quad (3.2)$$

where E_{ABC} is the kinetic energy of an arbitrary Auger transition ABC of an element, Z. An electron is ejected from the A-level by the incident beam. The terms $\frac{1}{2}[E_B(Z) + E_B(Z+1)]$ and $\frac{1}{2}[E_C(Z) + E_C(Z+1)]$ are the binding energies of the B-level and C-level in atoms having atomic numbers of Z and Z+1. Based on Equation 3.2 Coghlan and Clausing published comprehensive tables of calculated Auger energies using binding energies from Siegbahn et al. [31]. While it is difficult to find exact agreement between experimental Auger energies and calculated energies over the periodic table, there is a good general agreement.

3.2 Instrumentation

Auger analysis is performed with a PHI 700 Scanning Auger Nanoprobe by Physical Electronics, a division of ULVAC-PHI. It is an stand-alone AES only system with a cylindrical mirror analyzer (CMA), schematically shown in Figure 3.3. The system consists basically of two UHV - chambers: In the upper chamber a hot field emission electron source creates the electron beam, a Schottky-type field emitter, a ZrO_2 covered tungsten tip with an excellent spatial resolution. Voltages from 1 keV - 25 keV can be applied with beam currents from 1 nA - 20 nA which gives beam diameters in the nanometer range with a high current density. In this thesis Auger spectra are typically recorded with a 5 keV beam voltage and 20 nA beam current. Under these conditions the beam diameter is in the range of 30 nm. The upper chamber has a base pressure of $\approx 10^{-11}$ mbar and the emitter is constantly operated at $\approx$ 1800 K. The electron beam is focused by an electron optical column onto the sample. The specimen alignment is done by the determination of the focal point of the analyzer with the z-coordinate of the sample according to the peak position of the elastic peak at 1 keV. The Auger electrons are analyzed by a CMA with a high transmission efficiency. The analyzer's angle of acceptance, defined by the entrance slit, is 42° ± 6° for the Physical Electronics CMA and integrated around the full 360° azimuth, Figure 3.4. The energy resolution is a function of analyzer aberrations and the dimensions of the exit slit. The CMA is a band pass filter that allows passage of electrons within a band of energy, ΔE, at a pass energy, E, resulting in an energy resolution of $\Delta E/E$, which is constant for a fixed analyzer geometry. The energy resolution for the PHI 700 system is 0.5%. The electrons are

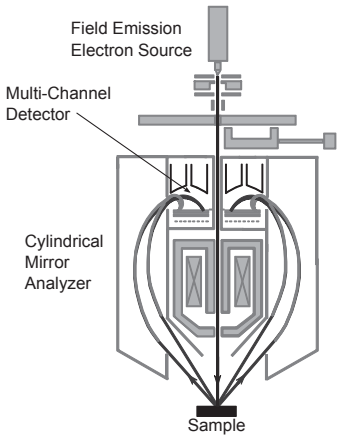

Figure 3.3: Schematic drawing of the PHI 700 Scanning Auger Nanoprobe adapted from Reference [20].

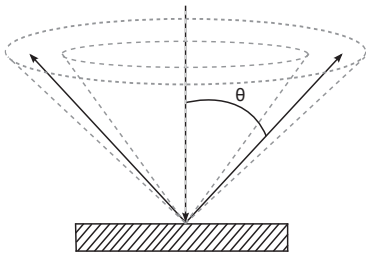

Figure 3.4: Geometry of the AES analysis configuration. The angle θ is the angle of emission with respect to the surface normal. The internal cone at 36° and external cone 48° of the analyzer are illustrated by the dashed lines.

detected with a multichannel plate (MCP). A secondary electron detector (SED) allows also the acquisition of SEM images. Topographical and physical information of the surface can be obtained and Auger analysis performed on specially identified regions of interest. Typically the main chamber has a base pressure of $\approx 10^{-10}$ mbar and is additionally equipped with an Ar^+-sputter gun for surface cleaning, charge neutralization (for insulating samples) or Auger sputter depth profiling. A load lock is attached to the main chamber, where samples are transferred into UHV within 30 min. The sample stage is motorized and therefore moveable in all directions including sample rotation and tilt. The whole Auger system can be operated fully automatic which was successfully utilized for high-throughput screening of samples in this thesis.

3.3 Surface sensitivity

Auger electrons are created both, near the surface and deep within the bulk, but only those electrons that originate from a volume within a few nanometers of the surface escape without energy loss. The analyzed depth is defined by the inelastic mean free path (IMFP, λ), which is the average of distances measured along the trajectories, that electrons with a given energy travel between inelastic collisions in a substance [32, 33]. The inelastic mean free paths of Pd, Ni and Co as a function of electron kinetic energy are shown in Figure 3.5. The surface sensitivity in AES is described by the mean escape depth (MED) in nanometers which is defined according to ISO18115 as average depth normal to the surface from which the specified electrons escape [33]:

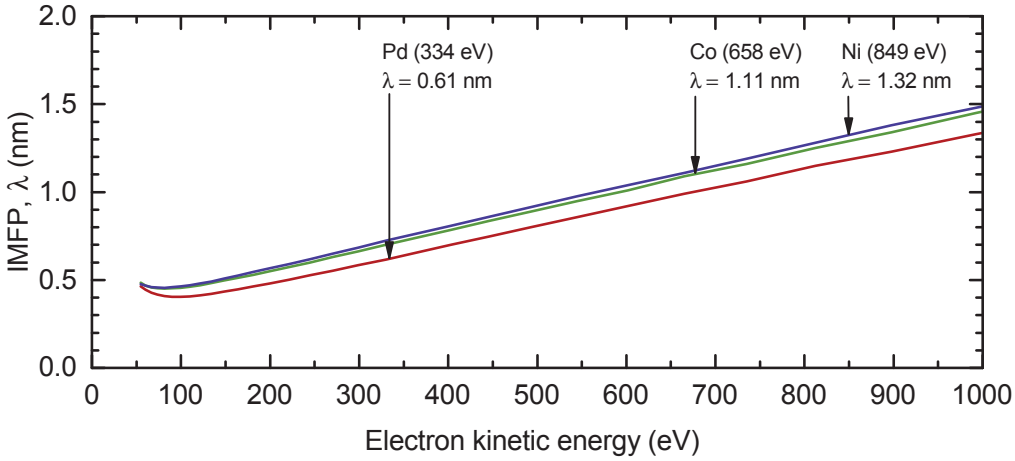

Figure 3.5: IMFPs of Pd, Ni, Co shown in the range from 50 eV to 1000 eV taken from Tanuma *et al.* [36]. The individual IMFPs of the pure elements according to the kinetic energy of the analyzed Auger electrons are given.

$$MED = \int_0^\infty z\psi(z,\theta)\mathrm{d}z \Big/ \int_0^\infty \psi(z,\theta)\mathrm{d}z \tag{3.3}$$

where $\psi(z,\theta)$ is the emission depth distribution function for depth, z, from the surface into the material and for the angle of emission, θ, with respect to the surface normal [34, 35]. Neglecting elastic scattering, the MED is simply given by the IMFP, λ, multiplied by the cosine of the emission angle, θ. The surface sensitivity strongly increases with the emission angle.

$$\lambda_{MED} = \lambda\cos(\theta) \tag{3.4}$$

Another term for the surface sensitivity is the number of "monolayers". The monolayer thickness, a, (in a cubic system) is calculated by [24, p. 89]:

$$a = \left(\frac{M}{\rho N_{Avo}}\right)^{1/3} \tag{3.5}$$

where a is in meter when M is the molecular mass in kg/mol, ρ the density in kg/m^3 and N_{Avo} Avogadro's number, 6.022x10^{23} mol^{-1}. For palladium the monolayer (ML) thickness is about 0.25 nm while the MED is about 0.45 nm. Hence, only the first two monolayers of palladium are analyzed with AES using the described measurement setup.

3.4 Data interpretation

Auger electron peaks are relatively small and superimposed on the continuous background of secondary and backscattered electrons [37]. An example for an Auger electron spectrum is given in Figure 3.6, a measured survey spectrum of Pd. The spectra are measured as a function of the kinetic energy of the electrons leaving the sample. In the PHI 700 system the spectra are acquired in the fixed retarding ratio (FRR) mode with an relative energy resolution of $\Delta E/E = 0.5\%$, hence the quotient of the absolute energy, ΔE, and the kinetic energy, E, of the emitted electrons is constant. This results in a continuous, linear change of the absolute energy resolution ΔE and numbers of electrons contributing to the spectrum with kinetic energy. The y-axis of direct spectra in FRR mode is labeled with $E \cdot N(E)$. The Auger peak position is determined from the peak maximum, here the Pd $M_5N_{4,5}N_{4,5}$ transition at 328 eV. In the corresponding derivative spectrum, shown in Figure 3.7, the background is suppressed and the Auger features are enhanced. All direct spectra in this thesis were processed with a 9-point smooth Savitzky-Golay convolution algorithm and 5-point derivative, (S9D5), a common procedure in AES. The y-axis is labeled with $d[E \cdot N(E)]/dE$. The Auger peak position is taken from the minimum, which is used for peak identification. Compared to the position of the Auger peak in the direct spectrum, the energy is shifted to by a few eV to higher kinetic energies. Auger

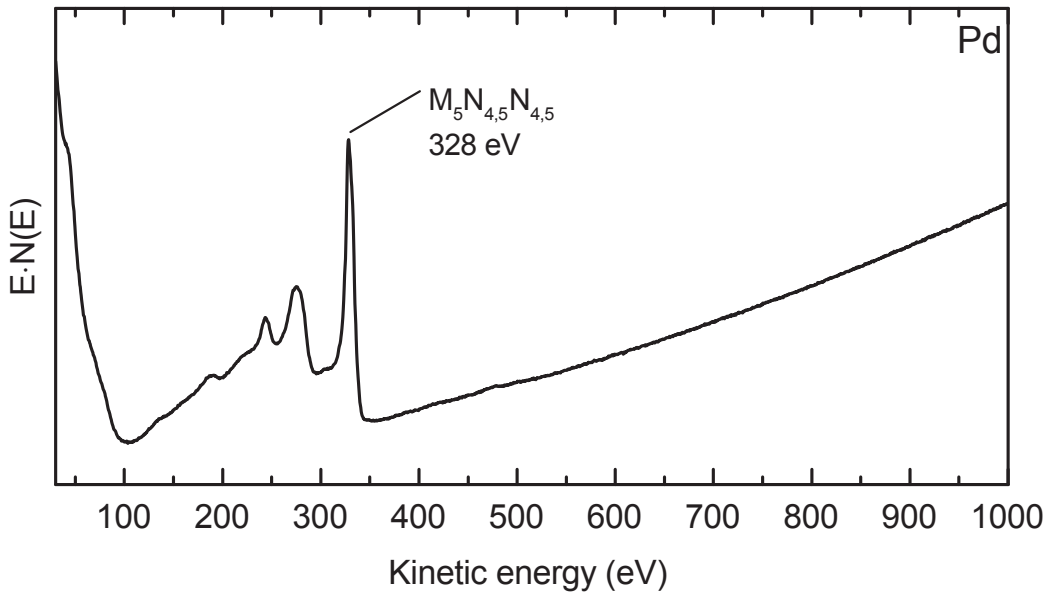

Figure 3.6: A survey Auger spectrum of pure Pd taken from a Ar^+-sputtered Pd foil, obtained in the range of 30 - 1000 eV with 0.5 eV step interval, 5 keV electron beam voltage and 20 nA current.

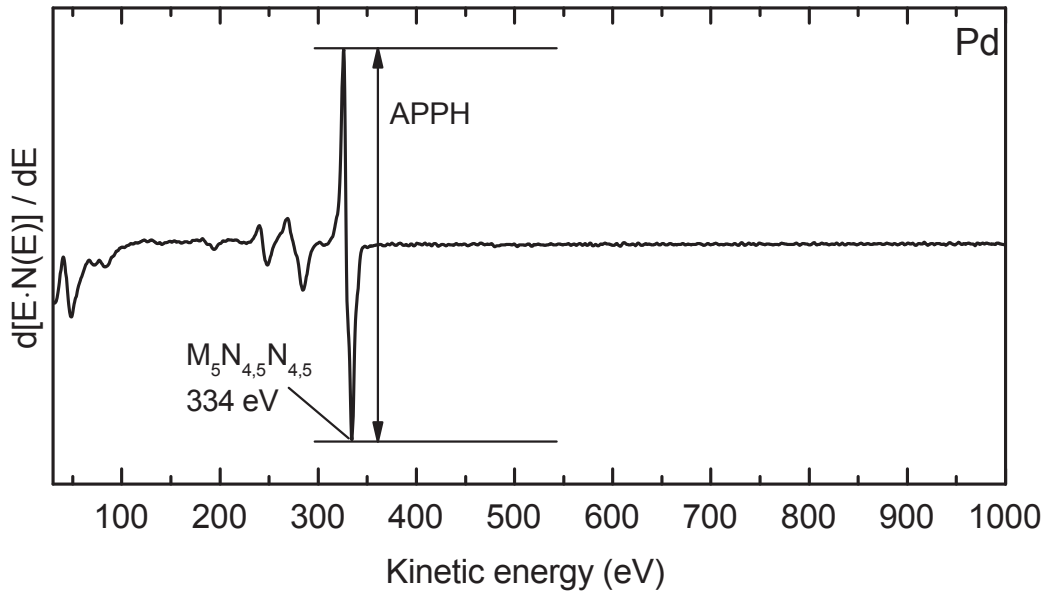

Figure 3.7: Derivative Auger spectrum of Pd processed with a 9-point smooth and a 5-point differentiation. The Auger peak intensity measurement is indicated by using the Auger peak-to-peak height (APPH).

electron spectra databases or reference spectra from pure elements or compounds, obtained on the same instrument, help to identify the constituents of a sample [20]. There are limitations of the qualitative analysis due to peak overlaps. The intensity of an Auger peak is measured from Auger peak-to-peak heights (APPH), which are used for quantitative analysis (Section 3.5). The line shape and peak position give information about the chemical state of an element. Energy shifts occur whenever there is a transfer of charge from one atom to another. In metallic compounds, such as transition metal alloys, there are almost no peak shifts detectable. Prominent examples for peak shape changes and shifts with the chemical environment (binding state) in Auger spectra are the LMM (LVV) transitions of Si, SiO_2, Si_3N_4, SiC and the KLL (KVV) transition of carbon for graphitic or carbidic compounds.

Surface contaminants of O, C or N can influence peak shapes and reduce peak intensities. Exposing samples to air leads to the adsorption of contaminants or oxidation of the sample. They can be removed by Ar^+-sputtering, but this can lead to changes of the composition and chemistry also. For the investigation of catalyst materials it is not suggested to apply Ar^+-sputtering for surface cleaning because any changes of the surface composition and chemical states should be avoided. The electron beam can induce a change of the surface composition by heating the sample with exposure time. Elements can diffuse from the bulk to the surface, diffuse across the surface or desorb from the surface. Compounds containing oxygen and carbon

can be decomposed, which leads to the formation of surface oxides or carbides. Therefore electron beam damaging is minimized by defocusing the electron beam or rastering over the sample. In this thesis spectra are usually measured with 90% defocused beam.

3.5 Quantitative analysis

One of the major applications of AES is the determination of the surface composition of solid materials. The composition of alloys especially for catalytic applications is an important issue. AES is a surface sensitive method, which addresses the first few monolayers of a sample. Several assumptions and approximation are made for the standardless quantitative analysis. Overall it is assumed that the sample is homogeneous within the analyzed sample volume and the electron beam itself does not alter the surface. The quantitative results are an approximation of the true composition, which is usually unknown. After qualitative analysis of the Auger spectra quantitative analysis can be performed in different qualities depending on the taken effort. A major aspect in quantitative AES is the matrix correction. The scientific discourse about matrix effects in quantitative AES started back in the 1970s [38–41]. A number of papers were published about different approaches of quantitative analysis and the use of relative sensitivity factors. In the literature quantitative analysis is extensively discussed on *binary* alloy systems.

This thesis deals with the quantitative analysis of a *ternary* Pd-Ni-Co alloy system over a wide range of alloy compositions. The more elements in the sample, the higher the chance of peak overlaps, due to the larger number of Auger transitions, e.g. the LMM Auger series of Ni and Co are overlapping in the ternary Pd-Ni-Co alloy system. Well separated Auger lines should be chosen to make sure, that no other element contributes to the measured Auger intensity. Low concentrations of elements close to the detection limit complicate the peak identification and the intensities have a higher deviation due to increased noise contributions. Different ways of quantitative analysis of a Pd-Ni-Co thin film alloy are presented in Section 6.2.

3.5.1 Auger peak intensity

A simple expression for the measured Auger intensity is given by Jablonski [32]. Equation 3.6 shows that the measured Auger intensity of an element, I_i, is directly related to the concentration of an element:

$$I_i = \frac{\Delta\Omega}{4\pi} T D I_p \sigma_i(E_p) P_i R_i \lambda \cos(\theta) N X_i \tag{3.6}$$

where:

I_i	-	Auger intensity for an Auger transition of element i
$\Delta\Omega$	-	analyzer solid angle of acceptance
T	-	analyzer transmission function
D	-	detector efficiency
I_p	-	primary electron beam current
$\sigma_i(E_p)$	-	electron-induced ionization cross section for the considered level at the primary energy E_p
P_i	-	probability of Auger transition after ionization
R_i	-	backscattering correction factor (BCF)
λ	-	inelastic mean free path (IMFP)
θ	-	angle of emission (see Figure 3.4)
N	-	atomic density (the number of all atoms per unit volume)
X_i	-	atomic fraction of the analyzed element.

Equation 3.6 presents all parameters which influence the measured Auger intensity. The parameters λ, R_i and N are material dependent factors, also known as matrix factors. The others depend on analyzer design and on instrumental settings. After peak identification the intensity of a certain Auger transition is taken from the APPH after differentiation of the spectrum, which was described earlier in Section 3.4.

3.5.2 Matrix effects

The accuracy of the quantitative analysis can be improved if the material dependent parameters atomic density, N, backscattering correction factor, R, and the IMFP, λ, in Equation 3.6 are taken into account. Further corrections for elastic scattering, peak shapes [42] or preferential sputtering [43] can be applied. Peak shape changes should be corrected using integrated spectra rather than differentiated spectra, but

the Auger peaks appear often as a bulge on the secondary electron cascade. Across an alloy series the peak shape is often constant. The matrix correction for a multicomponent alloy system can be realized by using average matrix relative sensitivity factors [22] or an iterative calculation procedure for the matrix correction factors [44]. The matrix correction leads to a higher accuracy of the quantitative analysis.

In electron-excited AES the backscattering correction factor (BCF) has been recognized as an important matrix correction term [45]. The electrons of the exciting electron beam penetrate deep into the sample up to a depth of several microns. During their trajectory, these electrons lose a certain amount of energy, change their direction and are also backscattered. Some of the backscattered electrons can in turn produce themselves Auger electrons if they have sufficient energy. This way backscattered electrons contribute to the total Auger current. In some papers and books the term "backscattering factor" is the same as the BCF, while in other papers and books the "backscattering factor" is identified as the backscattering fraction. The term "backscattering factor" is defined after ISO:18115-1 with the note, that different usages exist: "a factor defining the fractional increase in the Auger electron current due to additional ionizations in the sample caused by backscattered electrons above that arising directly from the primary electrons" [33]. The term "backscattering factor" was used by Shimizu, whose equations were usually used to calculate BCFs [46]. The BCF, denoted R, in Equation 3.7 is equal to unity plus the backscattering fraction, denoted r:

$$R = 1 + r \tag{3.7}$$

The definition of these two terms is considered by the ISO Technical Committee 201 on Surface Chemical Analysis, while the use of the term "backscattering factor" is objected. The NIST Backscattering-Correction-Factor Database for Auger Electron Spectroscopy offers the possibility to calculate BCFs from Monte Carlo simulations based on a simplified or an advanced model [47]. BCFs from the simplified model are obtained from an integration of the energy and angular distribution of backscattered electrons leaving the solid, the cross section for inner-shell ionization, and the secant of the backscattered-electron emission angle. BCFs from the advanced model are obtained from an integration over depth of the product of the excitation depth distribution function (EXDDF) and the integral emission depth distribution function (EMDDF). The EXDDF describes the depth distribution of inner-shell ionizations that lead to subsequent emission of the relevant Auger electrons for a specified primary energy and angle of incidence. The EMDDF describes the depth distribution of emitted Auger electrons for a specified analyzer-acceptance

Element	Pd	Ni	Co
Auger transition	$M_5N_{4,5}N_{4,5}$	$L_3M_{4,5}M_{4,5}$	$L_3M_{2,3}M_{2,3}$
Auger kinetic energy	334 eV	849 eV	658 eV
pure Pd	2.062		
pure Ni		1.637	
pure Co			1.720
$Pd_{90}Ni_8Co_2$	1.918	1.708	1.672
$Pd_{80}Ni_{10}Co_{10}$	1.932	1.713	1.676
$Pd_{60}Ni_{20}Co_{20}$	1.925	1.715	1.691
$Pd_{40}Ni_{30}Co_{30}$	1.934	1.727	1.684
$Pd_{10}Ni_{80}Co_{10}$	1.945	1.741	1.705
$Pd_{10}Ni_{10}Co_{80}$	1.956	1.751	1.712
PdNiCo	1.935	1.735	1.689

Table 3.3: Backscattering correction factors, R, calculated for the pure elements Pd, Ni, Co and for different Pd-Ni-Co alloy compositions with the advanced model and the geometry according to the PHI 700 setup. For the Monte Carlo simulations Bote *et al.* cross sections were applied and 10.000.000 trajectories for the IEMDDF and 10.000 trajectories EXDDF were used [47, 48].

angle. Monte Carlo simulations are performed over a specified number of trajectories to obtain EXDDF and EMDDF for the advanced model. These trajectories are calculated with differential elastic-scattering cross sections from the NIST Electron Elastic-Scattering Cross-Section Database [49], electron stopping powers from a predictive formula [50], and inner-shell ionization cross-sections from Casnati *et al.* [51], Gryzinski [52], or Bote *et al.* [48]. The advanced model shows a weak dependence of the BCF on the analyzer acceptance angle, which is a major advantage over the simplified model of electron transport. Values from the Shimizu formulae, based on the simplified model, can differ from the BCFs from the advanced model, because different algorithms and new data for the differential elastic-scattering cross sections are used. The BCFs from the advanced model are more accurate and used in the thesis. Table 3.3 shows the values of R calculated for the pure elements, Pd, Ni, Co and for several ternary alloys, which were calculated with the advanced model.

3.5.3 Relative Sensitivity Factors

The atomic concentration, X_i, (at.%) of an element in a multi-component system with unknown composition can be calculated with the general Equation 3.8, based on the intensity ratio of the measured intensity of the element in the specimen, I_i, to the intensity of the pure element, I_i^0:

$$X_i = \frac{\frac{I_i}{I_i^0}}{\sum_{j=i}^{n} \frac{I_j}{I_j^0}} \times 100\% \tag{3.8}$$

This approach neglects matrix effects and is only valid if the specimen and pure elements are measured under exactly the same experimental and instrumental conditions. Further a homogeneous elemental distribution within the analyzed volume is assumed. The quantitative results are a rather rough estimation of the sample composition. It is common to use relative sensitivity factors, S_i, instead of the intensities of of the pure elements in Equation 3.8:

$$X_i = \frac{\frac{I_i}{S_i}}{\sum_{j=i}^{n} \frac{I_j}{S_j}} \times 100\% \tag{3.9}$$

There are different kinds of RSFs and they depend on excitation energy of the electron beam. A detailed overview about RSFs is given in ISO 18118:2004 [53]. There are two types of elemental relative sensitivity factors. For general purposes the intensities of the pure elements are normalized to the intensity of a key element, known as pure element relative sensitivity factors, S_i^{Ep}. In AES the intensities of Cu $L_3M_{4,5}M_{4,5}$ or Ag $M_5N_{4,5}N_{4,5}$ transitions are chosen as a reference intensities, I_{key}:

$$S_i^{E_p} = \frac{I_i^0}{I_{key}} \tag{3.10}$$

Pure element relative sensitivity factors are given in the AES Handbook by Childs *et al.* [20] and by manufacturers [54]. The accuracy of the quantitative results can be improved by taking the measured intensity from a reference material or standard material with known atomic concentrations of the elements and a composition in the same range as the unknown [55]. The intensities from the reference material I_i^{ref} is normalized to the intensity of the key element, I_{key}, and the atomic concentration of the element in the reference material, X_i^{ref}. This kind of RSF is nominated S^{E_c} and is calculated by Equation 3.11. But reference samples are usually not available and it takes a lot of effort to prepare a well characterized reference sample for a new system.

$$S_i^{E_c} = \frac{I_i^{ref}}{X_i^{ref} I_{key}} \tag{3.11}$$

The quantitative results based on S_i^{Ec} are supposed to be more reliable than results based on S_i^{Ep}, because in S_i^{Ec} the matrix is comparable to the matrix of the specimen. A correction for the atomic density can be introduced into the equations for the elemental relative sensitivity factors 3.10 and 3.11 which results in atomic relative sensitivity factors, S_i^{Av}:

$$S_i^{At} = \left(\frac{N_{key}}{N_i} \right) S_i^E \tag{3.12}$$

The atomic density of the key element, N_{key}, is divided by the atomic density of the element, N_i. It is only a partial correction of the matrix effects. An almost full correction of the matrix effects is achieved with average matrix relative sensitivity factors (AMRSFs), S_i^{Av}, Equation 3.13. The definition of an average matrix was proposed by Seah *et al.* [56].

$$S_i^{Av} = \left(\frac{N_{Av} Q_{Av} R_{Av} \lambda_{Av}}{N_i Q_i R_i \lambda_i} \right) S_i^E \tag{3.13}$$

The subscript Av indicates the values of the hypothetical average matrix namely the atomic density, N_{Av}, the parameter for elastic scattering, Q_{Av}, the BCF, R_{Av}, and the IMFP, λ_{Av}. All equations for the calculation of the average matrix are given in [22, pp. 361].

3.5.4 Matrix correction

The matrix correction for a multi-component system with more than two components is adopted from Sekine *et al.* [44]. The three most important matrix effects are taken into account for the full matrix correction procedure: The correction for the atomic density, the correction for the inelastic mean free path and the correction for electron backscattering. Matrix correction factors have to be calculated individually for each element in the sample and for the individual alloy composition. Usually the real composition is unknown. Hence, the matrix correction factor has to be calculated iteratively. The ratio of the measured Auger intensity of an element, I_i, to the intensity of pure element I_i^0 in Equation 3.14 is defined as k-value, which are later also used in the same manner in the ED-EPMA/STRATAGEM data reduction routine in Chapter 4:

$$k_i = \frac{I_i}{I_i^0} \tag{3.14}$$

The intensity ratios in Equation 3.8 are replaced by the k-values:

$$X_i = \frac{k_i}{\sum_{j=i}^{n} k_j} \tag{3.15}$$

The matrix correction factor,F_i, is introduced in Equation 3.15:

$$X_i = \frac{F_i k_i}{\sum_{j=i}^{n} F_j k_j} \tag{3.16}$$

The matrix correction factor includes a correction term for the atomic density, N_i^0/N, a correction factor for the electron backscattering, R_i^0/R_i, and for the inelastic mean free path λ_i^0/λ_i:

$$F_i(X_i, X_j, ..., X_n) = \frac{N_i^0}{N(X_i, X_j, ..., X_n)} \frac{R_i^0}{R_i(X_i, X_j, ..., X_n)} \frac{\lambda_i^0}{\lambda_i(X_i, X_j, ..., X_n)} \tag{3.17}$$

These three factors are the more important ones among the other factors described before. All necessary values for pure elements and alloys can be calculated from databases [47, 57]. The atomic densities of the pure materials N_i^0 are available from the literature. The atomic density of an alloy N is given by a summation of the products of atomic concentration X_i and atomic density in the pure state N_i^0 for each element:

$$N = \sum_{j=i}^{n} X_i N_i^0 \tag{3.18}$$

A correction for elastic scattering, Q, which is considered in Equation 3.13 for the average matrix sensitivity factors, is neglected here [58]. The matrix correction factor cannot be calculated directly for an unknown composition because the three terms in Equation 3.17 depend on the composition and so does F_i. This dilemma can only be solved iteratively. A first approximation of the sample composition is estimated by Equation 3.15 to calculate a matrix correction factor F_i with Equation 3.17. A new composition can be calculated now with Equation 3.16. This procedure is repeated until the F_i reaches a constant value. The latest F_i provides a more correct composition of the alloy. The full matrix correction was applied to a Pd-Ni-Co alloy in Section 6.2.1 and compared to quantitative results based on RSFs.

4 Energy-dispersive X-ray spectroscopy

The method combination of energy-dispersive X-ray spectroscopy (EDX) at a scanning electron microscope (SEM) is called energy-dispersive - electron probe microanalysis (ED-EPMA) [59]. Compared to AES it is a bulk sensitive method suitable for the identification and quantification of elements in the sample. The method is non-destructive, precise and quick.

In this thesis the method was used to analyze the bulk composition of ternary Pd-Ni-Co thin film alloys on Si wafers by applying the commercial software package STRATAGEM, SAMx (France). The data reduction procedure is presented in detail in Chapter 7.

Further the spectra acquisition and data reduction routines were optimized for high-throughput screening of thin film alloy libraries. In combination with AES the surface and bulk composition was studied to identify surface segregation phenomena and reported in Chapter 8.

4.1 Characteristic X-Rays

In a SEM a high energy electron beam of some keV hits the sample and generates X-rays that can be detected by an X-ray spectrometer. The electron beam - matter interaction is shown schematically in Figure 3.1. The emission of an X-ray photon is the competing process to the Auger electron emission and is called X-ray fluorescence, which is more favorable for higher excitation energies. Electrons kick an electron out of an inner shell, e.g. K-shell, and ionize the atom, shown in Figure 3.2 (a). This state is energetically unstable. An electron from an outer shell fills the vacancy, see Figure 3.2 (b). The transition provides energy for the atom which either leads to the emission of a X-ray photon or the emission of an Auger electron, see Figures 3.2 (c, d). Emitted X-ray photons can be detected as characteristic X-rays for elements $Z \geq 4$.

The intensity of the emitted X-rays depends on the electron beam energy (keV) and the electron beam current (nA). The process of X-ray emission by incoming electrons is also known as the inverse photoelectric effect. X-rays can also be generated by X-ray photon excitation. Their detection is called X-ray Fluorescence (XRF) analysis. The probability of the interaction of the electron beam with the atoms is defined by the cross section. For electrons the cross section stays constant with increasing energy after reaching the maximum. In contrast, the cross sections of X-rays drop exponentially. In the case of electron excitation the probability is highest to interact with the valence electrons, while for X-ray excitation the interaction with core level electrons, especially with electrons from the K-shell, is more likely. The maximum of the electron cross section is by about the triple of the corresponding binding energy. The ratio of the primary energy to the binding energy is called overvoltage ratio, which should be larger than two to get sufficient ionization.

The probability that an ionized atom emits X-rays is called fluorescence yield (FY). It depends on the atomic number and the electron shell. The Auger electron emission is more likely for light elements than the emission of a photon. For this reason light elements are difficult to detect by EDX at SEM.

The terminology of X-ray lines is based on the Siegbahn nomenclature shown in Table 4.1. X-ray lines, which arise from the filling of a K-shell vacancy, are called K-lines, and from L-shells are called L-lines, respectively. A Greek letter indicates the shell from which shell an electron dropped down to fill the vacancy. The IUPAC X-ray nomenclature is consistent with the notation used in electron spectroscopy and is closely related to that of AES. If the X-ray lines within a series are very close together, only the electron shell with the Greek letter is mentioned, e.g. Si Kα.

Siegbahn	IUPAC	Siegbahn	IUPAC	Siegbahn	IUPAC
Kα_1	K-L_3	Lα_1	L_3-M_5	Mα_1	M_5-N_7
Kα_2	K-L_2	Lα_2	L_3-M_4	Mα_2	M_5-N_6
Kβ_1	K-M_3	Lβ_1	L_2-M_4	Mβ	M_4-N_6
		Lβ_2	L_3-N_5	Mγ	M_3-N_5
		Lγ_1	L_2-N_4		

Table 4.1: Siegbahn and IUPAC notation for selected X-ray lines of the K-, L- and M-series [60].

4.2 Instrumentation: EDX at SEM

The electron beam of a SEM Carl Zeiss SUPRA 40 with a temperature stabilized Schottky-field emitter is used for electron excitation up to 30 keV. The field emission electron source provides a short term stable and high electron beam current up to 20 nA. The beam current was measured by means of a Faraday cup and a calibrated picoammeter. The SEM allows the investigation of the sample surface morphology down to a few nanometers (see Chapter 2, Figure 2.2).

A state of the art Silicon Drift Detector (SDD) with Peltier cooling system ($T \approx -20°C$) is attached to the SEM setup. The EDX spectra were acquired using a Bruker XFlash 5010 SDD-EDS X-ray spectrometer with an energy resolution of 123 eV (FWHM) at the energy of the Mn Kα line and a take-off angle of 35°. The experimental geometry is shown schematically in Figure 4.1. The emitted X-rays from the sample are converted into electric charge within the detector crystal due to the photoelectric effect. For the experiments usually a pulse processor with a rate of 60 kcps is used. During spectra acquisition pulses are not taken into account if the time between them is to short. There is a certain dead time where incident photons are not counted, which is increasing with high count rates. The correction for the dead time is achieved by measuring the spectra with a certain live time, where only the active measuring time is considered.

A performance check of both, energy-dispersive spectrometer and SEM, is carried out every three month as part of the accreditation of the BAM 6.8 laboratory.

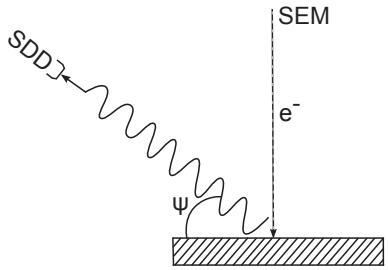

Figure 4.1: Schematic depiction of the geometry of the EDX analysis configuration. The position of the detector relative to the electron beam and the sample is described by the take-off angle $\psi = 35°$ measured relative to the surface plane.

4.3 Bulk sensitivity

The primary electrons of the electron beam loose successively their energy during interaction with the atoms in the sample. This characteristic of solids is called stopping power. The process can be demonstrated by Monte Carlo simulations. Therefore, Figure 4.2 shows the interaction of the electron beam with Si at 15 keV excitation energy for 200 electron trajectories. The penetration depth of the electrons depends on the energy of the primary electrons (blue). Some electrons leave the sample as backscattered electrons (red) after elastic collisions with the atoms of the sample. Every bend corresponds to a collision of an electron with an atom. X-rays are emitted from the entire excitation volume which depends on the excitation energy of the electron beam and density of the material. The dimension of the interaction volume defines the analyzed sample volume and is in the μm-range.

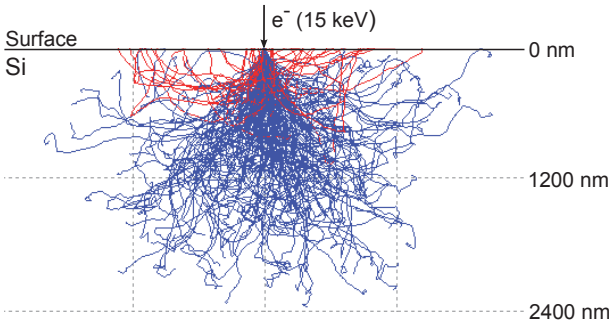

Figure 4.2: Interaction volume of a focused electron beam of 15 keV in pure Si. A Monte Carlo simulation (Casino software package Version 2.42) of 200 electron trajectories shows the primary electrons in blue and backscattered electrons in red [61]. The scale indicates the penetration depth of the electrons into the sample and the volume of X-ray emission.

4.4 Data interpretation

An EDX spectrum of pure Si taken with a electron beam voltage of 15 keV is shown in Figure 4.3 with logarithmic intensity scale. The most intense characteristic X-ray line of Si is the Kα line at a photon energy of 1.74 keV. Further the C Kα line at 0.28 keV is clearly present in the spectrum due to adventitious carbon on the surface. X-ray lines in energy-dispersive X-ray spectra appear as wide Gaussian peaks on a continuous background spectrum, that arises from the deceleration of the electrons in the electric field of the atoms. The so called bremsstrahlung spectrum covers the

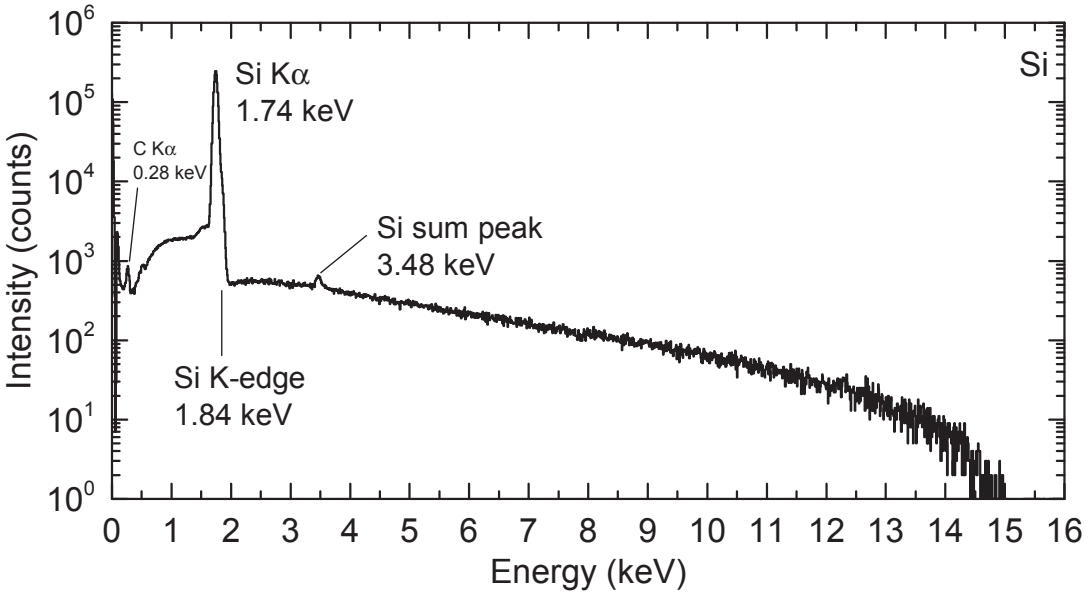

Figure 4.3: An EDX spectrum of an air exposed Si-wafer taken with an electron beam energy of 15 keV.

full length of the spectrum, here 15 keV according to the Duane-Hunt limit. Further, bremsstrahlung worsens the limit of detection of an element in the sample, because very weak lines cannot be detected above the background. A part of the emitted X-rays can be self absorbed in the sample ionizing other atoms. If the energy of the emitted photons is sufficient enough to excite a photoelectron, the probability for absorption is highest. So called absorption edges appear as sharp steps slightly above the X-ray lines of the electron shells. In Figure 4.3 the Si K-edge at 1.84 keV corresponds to the binding energy of the Si 1s core level. In an EDX spectrum peaks can appear that are not related to the sample itself. For instances in Figure 4.3 the Si Kα sum peak (pile-up peak) at 3.48 keV has exactly twice the energy of the Si Kα line. Sum peaks appear if the time between two photons is too short to be registered by the spectrometer as two separate pulses. Both events are detected as one pulse and so assigned to a channel at higher energy. At 1.74 keV lower energy of an X-ray line escape peaks can appear due to emitted Si Kα photons from the detector crystal. These photons can escape through the front contact of the detector and are not taken into account for actual X-ray line. Another peak in EDX spectra is the zero peak at 0 eV. It is a reference peak of the spectrometer from which the performance of the spectrometer can be checked directly. At high excitation energies X-rays lines can be emitted from other materials within the analysis chamber due to backscattered electrons from the sample, e.g. Al Kα or Fe Kα.

For quantitative analysis net intensities of the X-ray lines are determined after background subtraction. Therefore the bremsstrahlung background spectrum is simulated based on selected supporting regions in the EDX spectrum, where no X-ray lines are present. Furthermore absorption edges have to be taken into account. Overlapping peaks can be separated in many cases by peak deconvolution for elemental and quantitative analysis.

4.5 Quantitative analysis of a thin film on a substrate

The elemental composition of a sample homogeneous at the scale of the excitation volume can be determined by EDX. The composition of a thin film on a substrate can be analyzed, too but requires a model for quantification that addresses the inhomogeneous elemental distribution within the analyzed film - substrate system. Therefore the STRATAGEM software was applied for quantitative EDX data evaluation of thin films on thick substrates. In addition information about the film thickness is gained. Surprisingly EDX in combination with the STRATAGEM software was applied in only a few cases in the past though the required equipment, i.e. a scanning electron microscope (SEM) with an X-ray spectrometer attachment is available in many laboratories. Until now the method was only applied a few times to thin films [62, 63]. The quantitative analysis using STRATAGEM for a Pd-Ni-Co thin film alloy on Si substrate is presented in Chapter 7. It was one of the main analytical tasks of this thesis to extend the procedure from binary to ternary thin films and to develop a high-throughput screening strategy for alloy libraries.

5 Soft and hard X-ray photoelectron spectroscopy

X-ray photoelectron spectroscopy (XPS), also known as electron spectroscopy for chemical analysis (ESCA), is an established UHV based analytical method in surface and material science [21–23]. The principle of photoelectron spectroscopy (PES) is based on the photoelectric effect and on the analysis of photoelectrons emitted from a sample excited by X-rays.

The regime of excitation energies lower than 2 keV is referred to soft X-ray photoelectron spectroscopy (XPS) and excitation energies from 2 keV up to 12 keV to hard X-ray photoelectron spectroscopy (HAXPES) by definition [64, 65]. While XPS is a surface sensitive method, HAXPES is more bulk sensitive. From PES data the elemental composition can be determined qualitatively and quantitatively, except for H and He. PES is a very powerful method to investigate the chemical states of a sample. In contrast, the capabilities of AES are constricted to identify chemical states and EDX can only be used for of elemental analysis and quantification.

In Chapter 9 quantitative data from XPS and HAXPES combined with the data of AES and EDX are presented as non-destructive compositional depth profile. Furthermore the chemistry of the Pd-Ni-Co thin film alloy system derived from the PES data is presented as a non-destructive chemical depth profile.

5.1 The photoelectric effect

The photoelectric effect was discovered by Hertz in 1887 and the theoretical description followed by Einstein in 1905 [66, 67]. The emission of an electron out of an electron shell due to photon excitation is called photoelectric effect. If the incident particle in Figure 3.2 (a) is a photon with sufficient energy a photoelectron can be emitted. Here, it is a photoelectron from the K-shell, the 1s core level. The following process cascade in Figure 3.2 (b-d) is the same as for electron beam excitation. An electron from a higher shell fills the inner shell vacancy. The relaxation process either leads to the emission of an Auger electron or to the emission of a photon.

Once the photoelectrons (and Auger electrons) are emitted from the solid into the vacuum they can be analyzed according to their energies. The kinetic energy of a photoelectron, E_{kin}, is given by:

$$E_{kin} = E_{h\nu} - E_{bin} - \phi \tag{5.1}$$

where E_{bin} is the binding energy of the photo electron, $E_{h\nu}$ the photon energy and ϕ the work function, which is the required energy that an electron needs to escape from the solid. Photoelectrons can be excited only by photons, which have enough energy to overcome the work function of the individual material. The binding energy is characteristic for each core level of an element. It gives information about the atomic species and their binding states (chemical environment). In contrast Auger electrons have constant kinetic energies, because they are emitted in a secondary process, which is independent of the excitation energy, but which has to be at least sufficient enough for the photoemission of an electron. After creation of a photoelectron inside the solid, it has to travel to the sample surface, where it is emitted into the UHV. A measure for the travel distance of an electron in a solid is described by the inelastic mean free path, λ, introduced in Section 3.3. The photoionization cross section decreases by more than two orders of magnitude between 1 keV and 10 keV. Therefore a high photon flux is required for HAXPES, which can be provided by a synchrotron radiation facility. In contrast to XPS the theoretical description of the photo ionization cross section and the inelastic mean free for the hard X-ray regime is still lacking [36, 68–71]. Extensions of the theoretical approaches from the soft X-ray range into the hard X-ray range are provided by SESSA [57].

5.2 Instrumentation

The foundation of modern photoelectron spectroscopy was done in the 1950s by Kai Siegbahn at Uppsala University, who received the Nobel Prize in 1981 for his pioneering work. Actually ESCA was HAXPES from the beginning since Nordling *et al.* used Mo Kα radiation of $\approx$ 17.4 keV to study the Cu 1s core level by about 8985 eV [72]. Their findings were recently celebrated during the "50 years anniversary of the chemical shift" session at the HAXPES 2013 workshop held in Uppsala, Sweden [73]. Nowadays hard X-ray lab sources, such as Zr Lα ($\approx$ 2042 eV), Ag Lα ($\approx$ 2984 eV), Cr Kα ($\approx$ 5411 eV) or Cu Kα ($\approx$ 8041 eV) X-ray anodes are available and further development is in progress [74]. In this thesis the soft X-ray measurements were carried out in the BAM 6.8 laboratory at the Kratos XPS system

using monochromatic Al Kα (1486.7 eV) radiation. The hard X-ray photoelectron spectroscopy (HAXPES) experiments were performed during beam times at the synchrotron radiation source BESSY II at Helmholtz-Zentrum Berlin, Germany. In the following both measurement systems are presented in detail.

5.2.1 XPS at BAM 6.8

Laboratory XPS measurements at BAM 6.8 were carried out with an AXIS Ultra DLD electron spectrometer manufactured by Kratos Analytical, UK. Here, monochromatic Al Kα (1486.7 eV) radiation is used for excitation. The dual anode of the X-ray source provides Mg Kα (1253.6 eV) radiation, also. Sometimes it can be useful to switch the excitation energy in case Auger electron series are overlapping with photoelectron peaks. The system is equipped with a hemispherical electron analyzer and a delay line detector (DLD) detector. Survey spectra were acquired with a pass energy of 80 eV and the core levels of interest with 20 eV. The standard experimental XPS geometry is shown in Figure 5.1 (a), where the source-to-analyzer angle α is fixed at 60° and the angle of emission, $\theta = 0°$, which is the angle between the surface normal of the sample and the axis of the electron analyzer [22]. The surface sensitivity of XPS can be increased by increasing θ, which is described in Section 5.3. In this thesis spectra were also acquired at $\theta = 60°$ as shown in Figure 5.1 (b). The binding energy scale of the instrument was calibrated following a Kratos analytical procedure which uses ISO 15472 binding energy data [75].

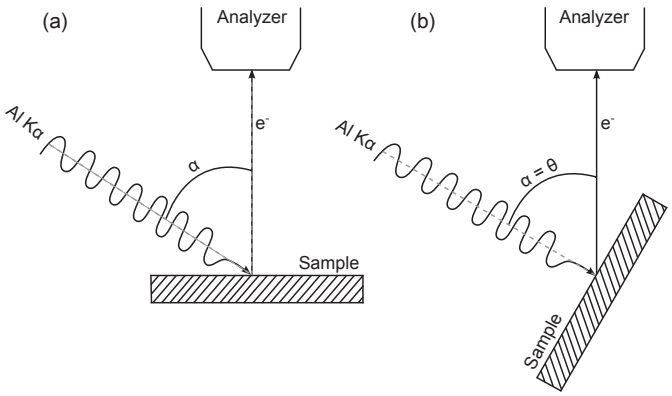

Figure 5.1: The experimental configurations of the XPS setup used in this thesis: (a) the source-to-analyzer angle, α, is fixed to 60° and the angle of emission, θ, is 0°. (b) geometry with increased surface sensitivity, where $\alpha = \theta = 60°$.

5.2.2 HAXPES at HZB/BESSY II

In this thesis synchrotron radiation experiments were carried out at Helmholtz-Zentrum Berlin, BESSY II, Berlin, Germany. In a synchrotron electron packages are accelerated radially almost up to the speed of light by strong magnetic fields under UHV conditions. If these relativistic electrons pass bending magnets (dipoles), undulators or wigglers, synchrotron radiation is emitted tangential to the direction of motion of the electrons. BESSY II is an electron storage ring with an energy of 1.7 GeV, providing synchrotron radiation from the terahertz to the hard X-ray regime, with an emphasis on the soft X-ray range. PES in the soft and hard X-ray range are only two out of many spectroscopic methods performed with synchrotron radiation, which has two major advantages compared to conventional laboratory XPS; its very high brilliance and the tunable photon energy. The application of soft X-rays lower than 2 keV for photoelectron spectroscopy at a synchrotron is well established. The HIKE (high kinetic energy) facility at BESSY II became available for users in 2009. At BESSY II HAXPES is performed at the KMC-1 beamline [76]. A bending magnet (dipole) provides photon energies from 2 keV - 12 keV. The photon energies are selected using a double crystal monochromator. The available photon energies with the corresponding energy resolution are shown in Figure 5.2. In this thesis the Si (111) crystal pair was used for the experiments. The photon energy was varied from 2.5 eV to 6.0 keV in several steps to increase the information depth. The intensity of the X-ray photon beam is monitored via a N_2 ionization

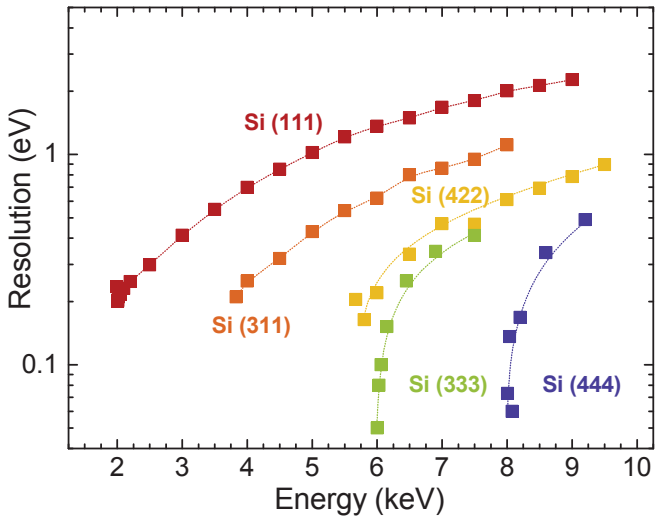

Figure 5.2: The resolution of the KMC-1 double crystal monochromator with Si-crystals with (111), (311) and (422) orientations. Si (333) and Si (444) correspond to higher-order reflection of the Si (111) orientation.

chamber. The aligned photon beam is focused in the analysis chamber of the HIKE end station on the sample via an X-ray glass capillary [77]. The experiments were performed close to grazing incidence geometry with an angle of emission, $\theta \approx 3°$, shown in Figure 5.3.

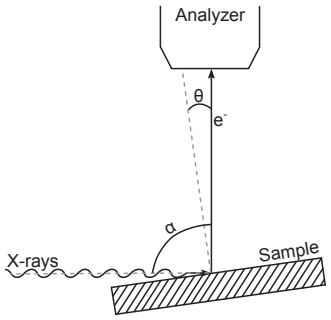

Figure 5.3: Experimental geometry of the HIKE setup, where the source-to-analyzer angle α is fixed to 90° and the angle of emission θ is $\approx 3°$.

The emitted photo electrons are analyzed with a Scienta R4000 hemispherical analyzer optimized for high electron kinetic energies from 150 eV to 10000 eV. HAXPES spectra were recorded with six different excitation energies (2.5 keV, 3.0 keV, 3.5 keV, 4.0 keV, 5.0 keV, 6.0 keV). The pass energy was kept constant at 200 eV and the 0.5 mm slit was used. The transmission function of the analyzer for these conditions, given by the manufacturer, is plotted in Figure 5.4 [78]. In all PES data the binding energy scale was corrected for charging effects by setting the C 1s core level to $E_{bin} = 285$ eV originating from adventitious-hydrocarbon [79, 80]. In case of HAXPES recoil effects, influencing the C 1s peak position at high photon energies, were neglected [81].

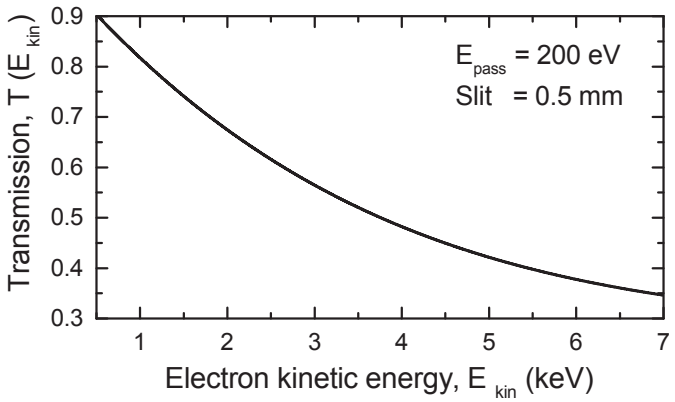

Figure 5.4: Transmission function of the SCIENTA R4000 analyzer for the conditions of the experiments in this thesis.

5.3 Surface and bulk sensitivity

Surface and bulk sensitivity is related to the IMFP depending on the kinetic energy of the emitted photoelectron and the material. The IMFP as a measure for the information depth in electron spectroscopy was already introduced in Chapter 3. Figure 5.5 shows the IMFP of pure Pd, Ni and Co in the soft and hard X-ray range as a function of electron kinetic energy.

The IMFP is increasing significantly with the electron kinetic energy determined by the photon excitation energy. At low photon energies PES is more surface sensitive and becomes more and more bulk sensitive with higher photon energies. At a tunable X-ray source, such as a synchrotron radiation source like BESSY II, the photon energy can be increased continuously and so the information depth can be varied. The increased bulk sensitivity of HAXPES is its major feature. The information depth of PES is defined in the ISO vocabulary [33]. It is defined as the layer thickness from which 95% of the detected signal originates. The ID, $z_{95\%}$ is calculated with Equation 5.2:

$$z_{95\%} = 3\lambda\cos(\theta) \tag{5.2}$$

XPS data were acquired with an emission angle, θ, of 60° and 0°, schematically shown in Figure 5.1 and 3° for HAXPES, shown in Figure 5.3. In case of HAXPES $\cos(\theta)$ is ≈ 1 and the ID becomes $\approx 3\lambda$. IMFPs for the soft and hard X-ray range were calculated using SESSA [57].

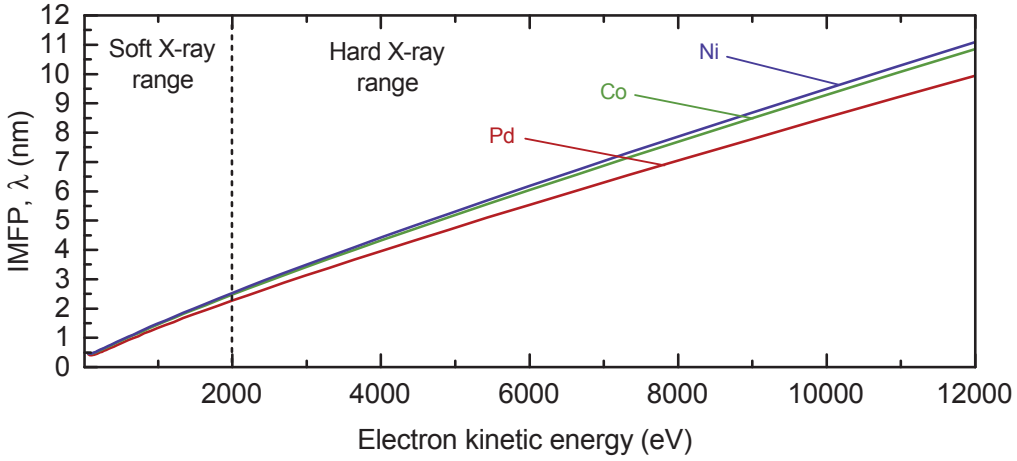

Figure 5.5: IMFP as a function of the electron kinetic energy for Pd, Ni, Co shown in the range from 50 eV to 12000 eV [36].

For example, the XPS information depth related to the Pd $3d_{5/2}$ core level with a binding energy of 335 eV, is about 2.3 nm ($\approx$ 9 ML) at $\theta = 60°$ and about 4.5 nm ($\approx$ 18 ML) for $\theta = 0°$. The ID range addressed by HAXPES increases from 7.5 nm ($\approx$ 30 ML) at a photon energy of 2500 eV to 16.5 nm ($\approx$ 66 ML) at 6000 eV for the given measurement geometry. A monolayer (ML) of Pd is about 0.25 nm and was calculated in Section 3.3. IDs calculated for the Pd-Ni-Co alloy system are slightly higher, because of the lower density of the alloy system the IMFPs are increased compared to pure Pd. Values can be found in Chapter 9.

5.4 Data interpretation

A measured photoelectron survey spectrum of pure Pd excited by monochromatic Al Kα (1486.6 eV) irradiation is shown in Figure 5.6, where the characteristic photoelectron (3s, 3p, 3d, 4s, 4p, 4d) and Auger electron peaks (MNN series) are labeled.

Survey spectra give an overview of the elements present in the sample according to the shell structure (core levels) of the atomic electrons. It is common to plot the number of detected electrons against the binding energy (bottom X-axis), while the electrons are actually analyzed according their kinetic energy (top X-axis). Photoelectrons have characteristic binding energies (with respect to the *chemical shift*),

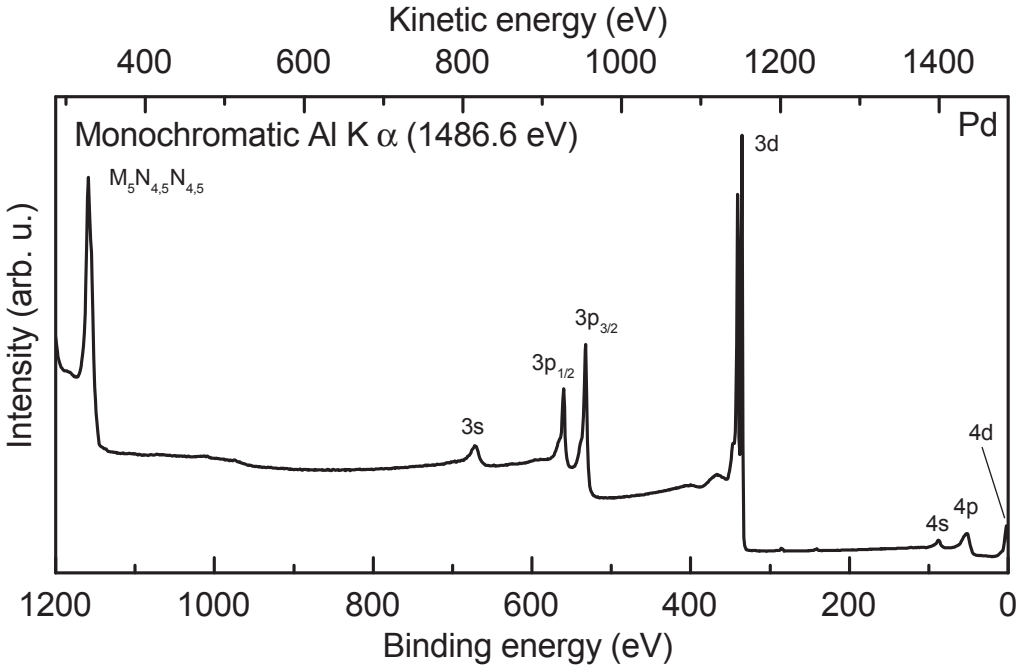

Figure 5.6: A measured X-ray photoelectron survey spectrum of Pd recorded with monochromatic Al Kα (1486.6 eV) radiation.

while Auger electrons have characteristic kinetic energies. The peaks appear above a step-like background arising to higher binding energies (lower kinetic energies, respectively) from inelastic scattering of electrons.

The notation of the core levels is nl_j (see Table 3.1) where n is the principal qunatum number, l is the orbital angular momentum quantum number and j is the total angular momentum quantum number, which is the sum $(l + s)$ where s is the spin angular momentum quantum number $(\pm 1/2)$. Thus, s levels $(l = 0)$ are singlets and p-, d- and f-levels, where $(l > 0)$, are doublets. The splitting in two possible states with different energies is known as the spin-orbit $(j-j)$ coupling. The relative intensities of two levels are given by the ratio of their degeneracies $(2j + 1)$. The difference in binding energy between the doublet components ΔE_B is a characteristic measure in photoelectron spectra. The 4d levels of Pd close to 0 eV binding energy are referred to the valence band, which is a source of information on both electronic and chemical structure. In metals the valence band and the conduction band overlap and the highest occupied state is termed the Fermi level, E_F. The valence band can be studied in detail using ultraviolet photoelectron spectroscopy (UPS). The nature of Auger electrons was discussed in Chapter 3, except here they are caused by the refilling of core holes after X-ray photoemission (XAES).

As the region of interest for the PES data analysis the Pd 3d core level is shown in Figure 5.7, acquired with a pass energy 20 eV to have sufficient resolution. The background determination (grey) is performed after Shirley [82]. The peak positions of $Pd_{5/2}$ at E_{bin} = 335.0 eV and $Pd_{3/2}$ at E_{bin} = 340.3 eV are in agreement with the

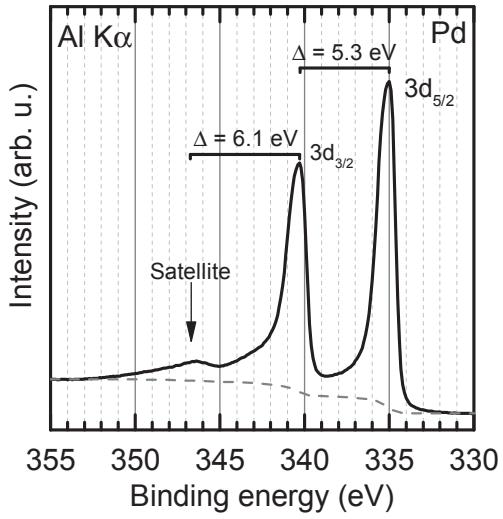

Figure 5.7: The Pd 3d core level spectrum recorded with monochromatic Al Kα radiation of 1486.6 eV.

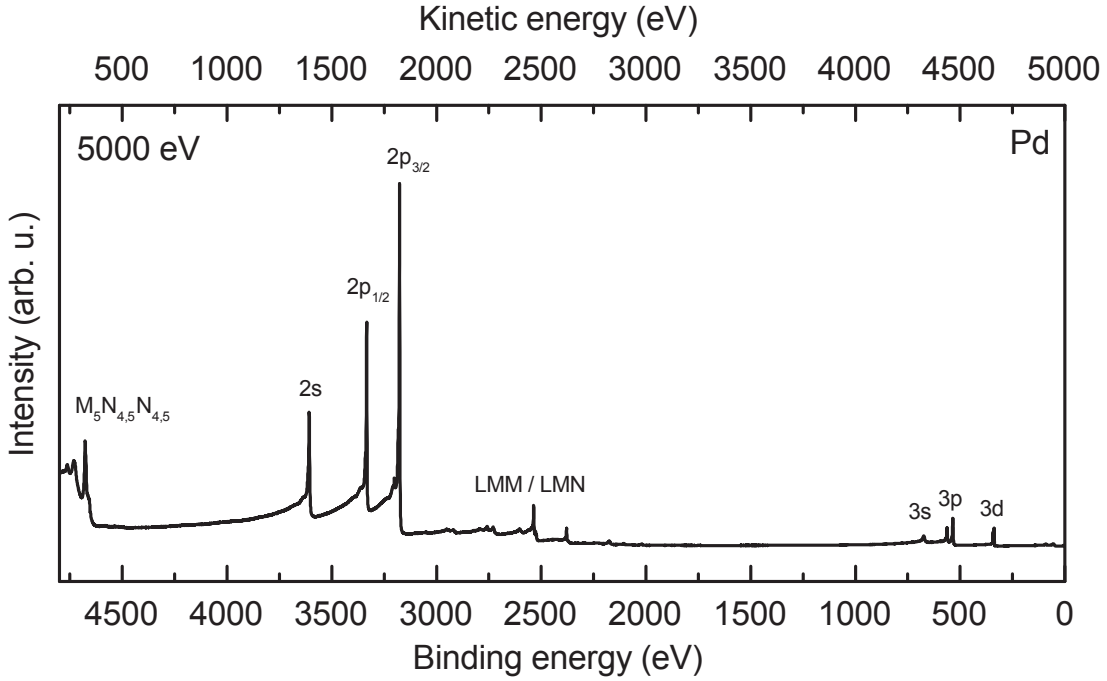

Figure 5.8: A measured Pd survey spectrum taken at the KMC-1 beamline with a photon excitation energy of 5000 eV selected with the Si (111) double crystal monochromator.

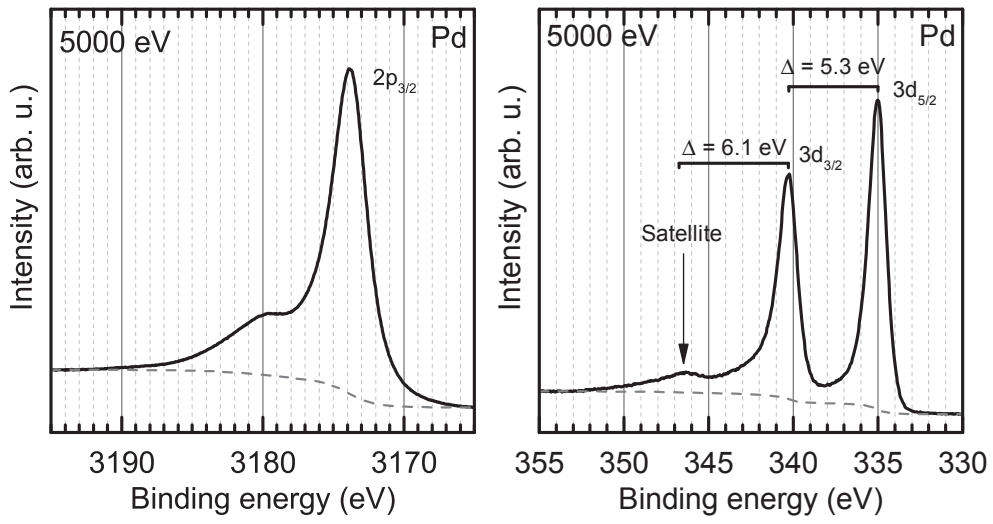

(a) (b)

Figure 5.9: Detailed spectra of the Pd $3p_{3/2}$ (a) and Pd 3d (b) core levels taken with an excitation energy of 5000 eV.

literature [83]. There is a core-level satellite by about 6 eV higher binding energy than the Pd $3d_{3/2}$ line, due to a 4d-electron shake-up process [84]. The Pd $3d_{5/2}$ satellite line overlaps with the tail of the Pd $3d_{3/2}$ peak. The shake-up satellite

arises from the interaction of the emitted photoelectron with the valence band and belongs to secondary structures observed in photoemission spectra. More detailed information about these characteristics in photoelectron spectra are given elsewhere [22, 85].

A measured photoelectron survey spectrum of pure Pd taken with an excitation energy of 5000 eV at the KMC-1 beamline is shown in Figure 5.8. The characteristic peaks of Pd below 1000 eV binding energy are present and additionally deeper core levels as 2s and 2p of Pd and more Auger series (LMM/LMN), which cannot be excited by Al Kα radiation. The Pd $2p_{3/2}$ and the Pd 3d core levels are shown in Figure 5.9 (a, b). The access to deeper core levels is a major feature of HAXPES, e.g. the Ni 1s core level at 8.7 keV was studied in detail [86]. The cross section of the photoelectron peaks of the higher core levels, e.g. Pd 3d at E_{bin} = 335 eV, is getting very low at high excitation energy, which increases the spectra acquisition time, especially by acquiring the valence band. On the other hand the cross section of the deeper core levels, e.g. Pd $2p_{3/2}$ at E_{bin} = 3174 eV, gets very high. One has to keep in mind that the information depth becomes smaller when a deeper core level is investigated, because the kinetic energies of the photoelectrons get lower with higher binding energies.

The shift of the binding energy of a core level related to the chemical environment (binding state) of an atom is called the *chemical shift*. Notably core level binding energy shifts give information about the electronic structure of materials, e.g. the oxidation states of elements. The shape of photoelectron peaks is determined by the life time of the ionized state of the atom which leads to Lorentzian lineshape. Another source of line broadening arises in the PES experiment from the light source and the spectrometer, which limits the energy resolution. The experimental broadening is described by a Gaussian lineshape. Both together give a Voigt profile [87]. Peak asymmetry on the high binding energy side of the main line occurs in transition metals, where photoelectrons can interact with conduction electrons and thus loosing some energy. A Doniach-Sunjic line profile is the appropriate peak shape model here [88]. In this thesis PES data were processed with Unifit 2013 (Unifit Scientific Software GmbH, Leipzig, Germany) by Hesse.

5.5 Quantitative analysis

For the quantitative analysis the contributions to the intensity of a photoelectron peak, I_i, should be considered first which is described approximately by the following Equation 5.3:

$$I_i = T(E_{kin}) \cdot D \cdot A \cdot F \cdot \Delta\Omega \cdot (\mathrm{d}\sigma_i/\mathrm{d}\Omega) \cdot \int N(z) \cdot X_i(z) \cdot \exp\left[-\frac{z}{\lambda(E_{kin}) \cdot \cos(\theta)}\right] \mathrm{d}z \quad (5.3)$$

$T(E_{kin})$	-	analyzer transmission function as a function of kinetic energy
D	-	detector efficiency
A	-	analyzed area
F	-	photon flux of the incident X-rays
$\Delta\Omega$	-	analyzer solid angle of acceptance
σ_i	-	photoionization cross section
N	-	atomic density (the number of all atoms per unit volume)
X_i	-	atomic fraction of the analyzed element
z	-	sample depth from the surface
$\lambda(E_{kin})$	-	inelastic mean free path (IMFP)
θ	-	angle of emission.

Equation 5.3 reflects the relationship between measured signal intensity and the atomic fraction. The higher the content of an element in the sample the higher is the photoelectron intensity. The parameter T, D, A, F and $\Delta\Omega$ are determined by the experimental setup. The photoionization cross section depends on the core level and changes strongly with photon energy. The IMFP, λ, depends on the electron kinetic energy and as well as the atomic density, N, on the sample composition.

The quantitative approach assumes that the sample surface is atomically flat and clean and that the distribution of the elements within the analyzed depth is homogeneous, which can be considered as idealized experimental conditions, but usually the depth profile of the elemental distribution in a sample is unknown or of interest in case of studying surfaces segregation.

For the quantitative analysis of the Pd-Ni-Co alloy the Pd 3d, Ni $2p_{3/2}$ and Co $2p_{3/2}$ core levels were chosen. The net peak intensities were obtained from survey spectra after Shirley-background subtraction. The measured intensities have to be normalized before quantitative interpretation according Equation 5.4. Therefore they are divided by the product of the photoionization cross section of the core

level, σ_i, and the IMFP, λ. Both depend on the photoelectron kinetic energy, E_{kin}. The Kratos spectrometer transmission function was given by the manufacturer and the established Scofield' photoionization cross sections for Al Kα were used [89].

$$I_i' = \frac{I_i}{T(E_{kin}) \cdot \lambda(E_{kin}) \cdot \sigma_i} \tag{5.4}$$

The atomic concentration of each element in a sample, X_i, can be calculated based on the normalized intensities I_i' with Equation 5.5:

$$X_i = \frac{I_i'}{\sum_{j=i}^{n} I_j'} \times 100\% \tag{5.5}$$

The quantification of PES data acquired at a synchrotron radiation source is more complicated. Several parameters in Equation 5.3 depend on the photon energy, the kinetic energy of the photoelectrons, respectively.

As a simple experimental approach the measured peak intensities from the alloy were related to measured peak intensities from pure elements, I_i^0, which is similar to the k-value approach in AES and EDX as a first approximation for the composition. The measured intensities from pure elements can be considered as experimental pure element relative sensitivity factors (PERSFs). The atomic concentrations of Pd, Ni and Co were calculated after:

$$X_i = \frac{\frac{I_i}{I_i^0}}{\sum_{j=i}^{n} \frac{I_j}{I_j^0}} \times 100\% \tag{5.6}$$

The HAXPES data were treated in the same manner as the XPS data. The net peak intensities I_i of the Pd 3d, Ni $2p_{3/2}$ and Co $2p_{3/2}$ core levels were derived from survey spectra measured after Shirley-type background subtraction. The peak intensities were normalized to the ionization current of the photon beam. During peak acquisition the experimental conditions were considered to be stable. The intensities were taken from sputter deposited pure Pd, Ni and Co thin films after Ar^+-sputter cleaning.

6 Characterization and quantification by AES

In this chapter the results of the characterization and quantification of ternary Pd-Ni-Co alloys by electron excited Auger electron spectroscopy are presented. AES was the main analytical method of this project and was used for process control, development and optimization of the ternary alloy thin film libraries deposition. Further high-throughput screening experiments have been performed which are presented in Chapter 8.

6.1 Characterization of Pd-Ni-Co alloys by AES

The ternary alloy system of Pd, Ni and Co was extensively studied by AES in this thesis. In Figure 6.1 the undifferentiated Auger electron spectra of pure Pd (a), the $\mathbf{Pd_{69}Ni_{18}Co_{13}}$ alloy (b), pure Co (c) and pure Ni (d) are shown. Here, contaminants from oxygen (O KLL) and carbon (C KLL) were removed by Ar^+-sputtering (3 kV, 2 μA, 6 s) before spectra acquisition to achieve better peak intensities. In case of the Pd-Ni-Co alloy and pure Co not all traces could be removed entirely. The spectra represent the elemental composition of the first monolayers. 3d transition metals have characteristic Auger series like a fingerprint. In the first row transition metals, e.g. Ni and Co, the LMM and in the second row, e.g. Pd, the MNN transitions are characteristic. The LMM and MNN Auger series appear also in the Pd-Ni-Co alloys. The main peak in the Pd spectrum (a) at around 330 eV is a closely spaced peak. The peak is usually nominated $M_{4,5}N_{4,5}N_{4,5}$ to point out that there are two core levels involved. In a Pd rich alloy, e.g. $\mathbf{Pd_{69}Ni_{18}Co_{13}}$ (b) the LMM transitions of Ni (c) and Co (d) appear on the huge secondary electron background. Especially the intensity of the $L_3M_{2,3}M_{2,3}$ of Co, used to quantify the Co content in the alloys, is very low and limits the detection of low Co concentrations.

In Figure 6.2 the corresponding derivative spectra to Figure 6.1 are shown. The peaks appear as amplitudes and the peak positions are determined at the minimum. In the alloy the MMM transitions cannot be detected. These transitions are very

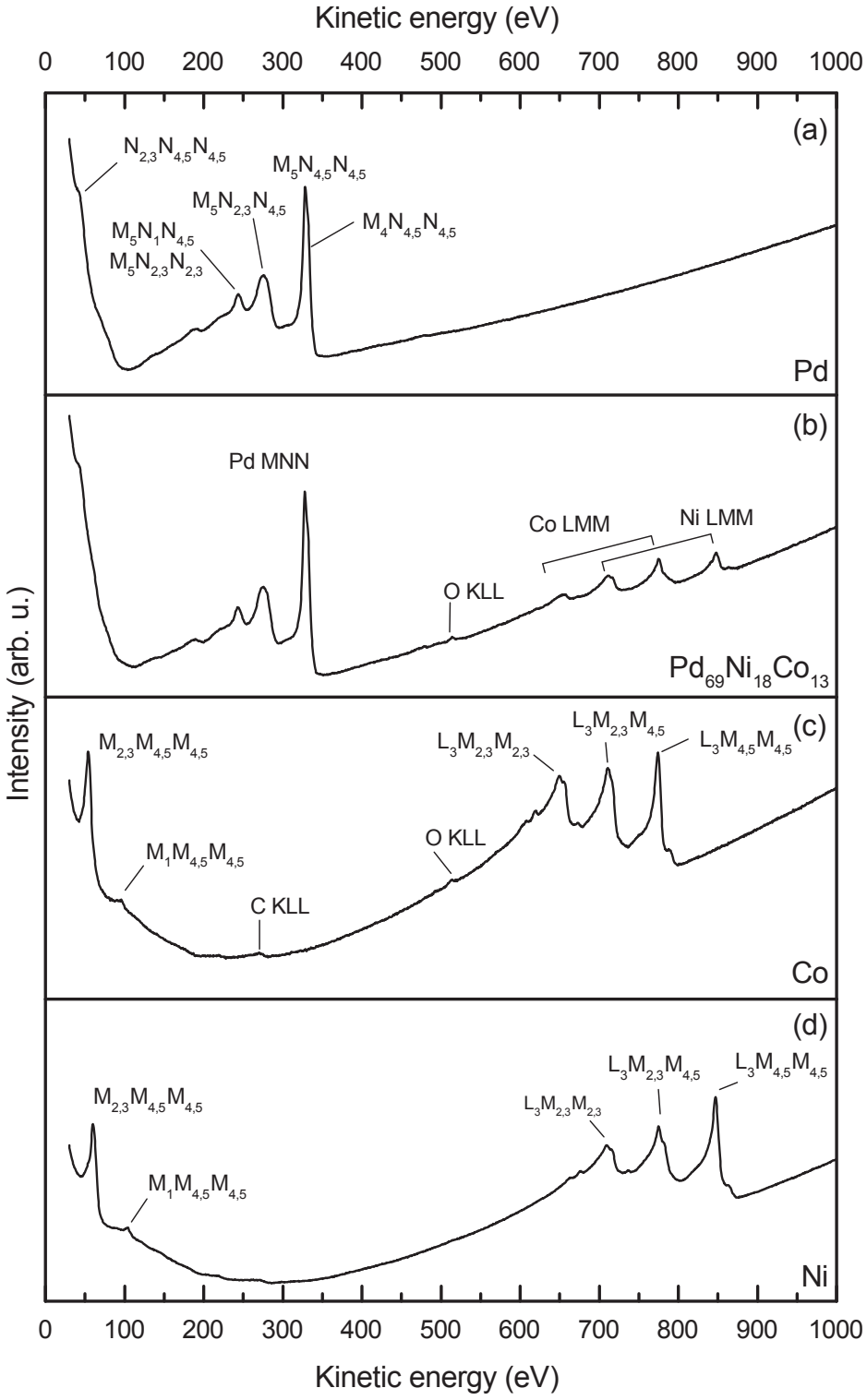

Figure 6.1: Auger survey spectra of pure Pd (a), Pd-Ni-Co thin film alloy (b), pure Co (c), and pure Ni (d) acquired with a 5 keV electron beam and 20 nA beam current after surface cleaning by Ar^+-sputtering.

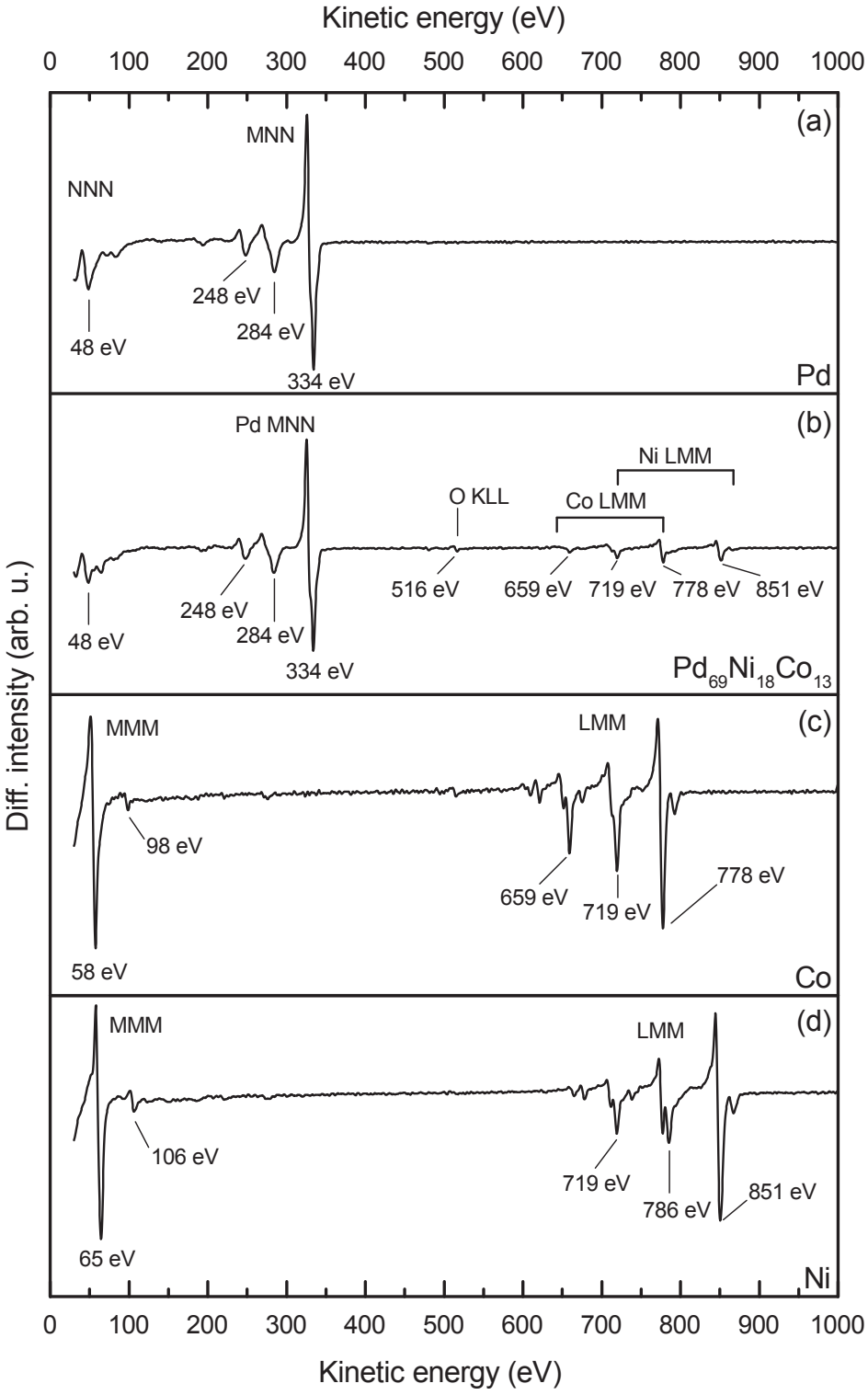

Figure 6.2: Derivative Auger survey spectra (S9D5) of pure Pd (a), Pd-Ni-Co thin film alloy (b), pure Co (c) and pure Ni (d) acquired with a 5 keV electron beam and 20 nA beam current after surface cleaning by Ar^+-sputtering.

surface sensitive because of the very short IMFP of the electrons. They arise directly from the surface. The MMM transitions of Ni and Co appear almost at the same kinetic energy. The palladium MNN Auger lines do not interfere with the LMM Auger transitions of Ni and Co. The peak shapes of the Auger lines of the alloy are comparable to the peak shapes of the pure elements. Peak shifts due to alloying were not observed.

Usually the alloy samples were investigated as received. They were carried under an inert gas atmosphere during transport but air exposure could not be avoided directly after alloy deposition and mounting them for analysis. The analysis of the samples was performed without any further treatment to keep the alloy surface intact. Figure 6.3 (a) shows the influence of carbonaceous contaminants due to air exposure on the Pd MNN transitions. The C KLL transition appears at lower kinetic energies next to the Pd $M_{4,5}N_{4,5}N_{4,5}$ transition. These contaminants are also found on pure Pd after air exposure. Both samples were sputter cleaned to check if the peak shape is influenced either by oxidation and contamination or sputtering. An alloy composition of $\mathbf{Pd_{40}Ni_{32}Co_{28}}$ was chosen for this comparison. The composition changed to $\mathbf{Pd_{53}Ni_{30}Co_{17}}$, which demonstrates the consequences of sputtering for the alloy composition. Here, the compositions were calculated using the PHI ERSFS in Table 6.1. The peak shape and position of the Pd $M_{4,5}N_{4,5}N_{4,5}$ transition did not change. The detailed spectra of the LMM transitions of Co and Ni are shown in Figure 6.3 (b). The most intense $L_3M_{4,5}M_{4,5}$ transition of Ni at 848 eV and Co at 774 eV and Co $L_3M_{2,3}M_{2,3}$ transition at 655 eV are indicated. The peak shape of both elements is not influenced by contaminants, oxidation, alloying or sputtering, except the background contribution of the secondary electrons changes. The carbonaceous layer on top of the sample leads to attenuation of the Auger electrons. It is assumed that the measured peak intensities of a sample are all affected in the same manner. Oxygen, caused by adsorbed water and oxidation, is also present on the sample surface after air exposure. In Figure 6.4 the corresponding derivative spectra to Figure 6.3 are shown. In (a) the C KLL is very dominant at 270 eV within the Pd MNN transitions of the air exposed alloy. The adsorption of carbon species on the alloy is stronger compared to pure Pd according to the intensity of the C KLL transition in the spectra. After sputter cleaning the spectra look nearly identical. In (b) the Ni and Co LMM transitions are shown after differentiation. The alloy spectra are noisier, due to the lower concentrations of Ni and Co.

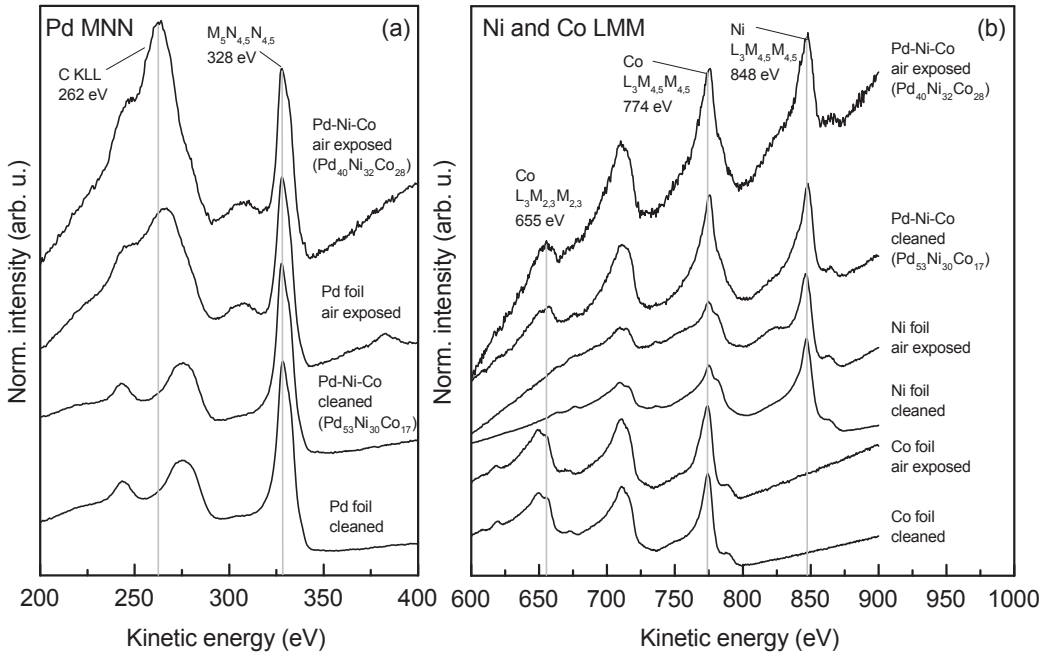

Figure 6.3: The Pd MNN region (a) and the Co and Ni LMM regions (b) of an Pd-Ni-Co alloy before and after cleaning by Ar^+-sputtering are compared to reference spectra of pure elements.

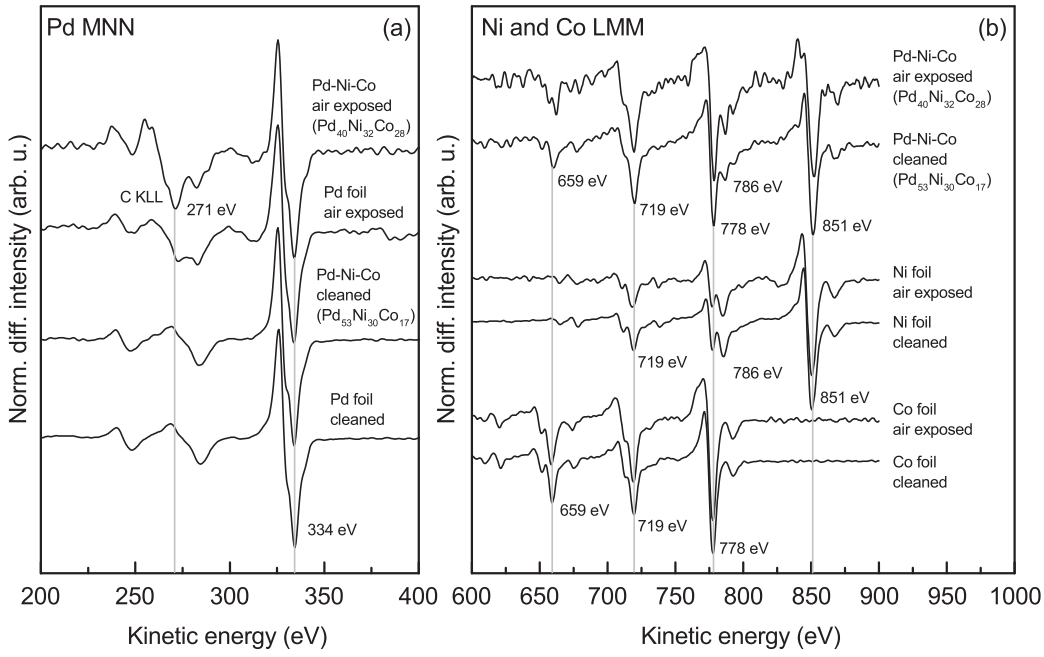

Figure 6.4: The corresponding differentiated Auger spectra (S9D5) of the Pd MNN (a) and Ni and Co LMM regions (b) shown in Figure 6.3.

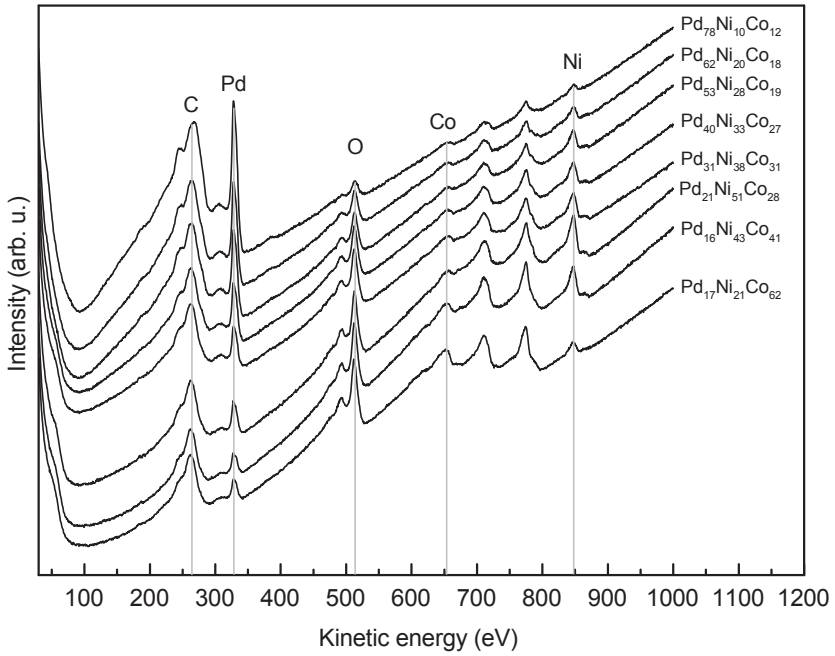

Figure 6.5: Auger survey spectra of Pd-Ni-Co alloy selection taken with a 5 keV electron beam and 20 nA beam current. All compositions were measured on an alloy library sample as received.

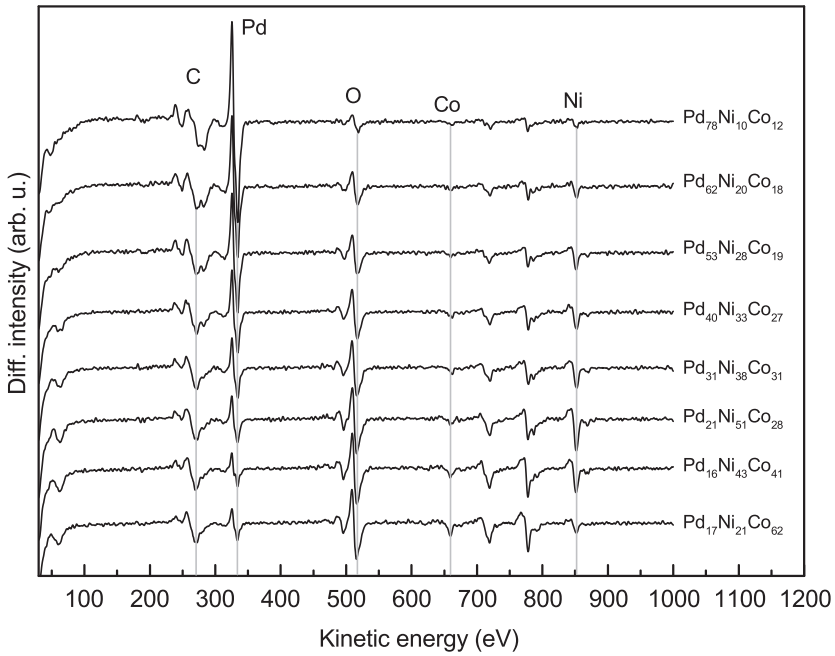

Figure 6.6: Corresponding derivative AES spectra (S9D5) of the alloy compositions shown in Figure 6.5.

A Pd-Ni-Co alloy selection, measured on a single sample deposited with setup 2 (Section 2.2), is shown in Figure 6.5 and in the derivative form in Figure 6.6. The compositions were calculated using the PHI ERSFS in Table 6.1. The high spatial resolution of electron excited AES allows to compare different alloy compositions within one alloy library to each other. This combinatorial approach was further optimized to perform high-throughput screening by AES and study Pd-Ni-Co alloys systematically. The Pd concentration decreases from 78 at.% to 16 at.%. The content of Ni increases from 10 at.% to 51 at.% and of Co from 21 at.% to 62 at.%. The Pd-Ni-Co alloy selection includes a Pd-rich, $\mathbf{Pd_{78}Ni_{10}Co_{12}}$, a Ni-rich, $\mathbf{Pd_{21}Ni_{51}Co_{28}}$, and a Co-rich, $\mathbf{Pd_{17}Ni_{21}Co_{62}}$, alloy. The survey spectra show the sample as received. Carbon and oxygen are clearly present on the sample surface. The intensity of oxygen increases with higher concentrations of Ni and Co and the intensity of carbon stays nearly constant over the whole range of concentrations. The Pd, Ni, Co peak shapes are not influenced by the alloy composition or by oxidation.

6.2 Quantitative analysis of a Pd-Ni-Co alloy by AES

An AES derivative (S9D5) survey spectrum in the range from 30 eV - 1000 eV of a Pd-rich Pd-Ni-Co alloy with unknown composition is shown in Figure 6.7 (a) after Ar^+-sputter cleaning. The intensities of the Ni and Co LMM transitions are quite low compared to the Pd MNN transitions. The LMM transitions of Co and Ni between 700 eV and 900 eV are overlapping except for the Co $L_3M_{2,3}M_{2,3}$ at 659 eV, which has significantly lower intensity than the Co $L_3M_{4,5}M_{4,5}$ transition at 778 eV. Figure 6.7 (b-d) show the selected regions of the Auger transitions of the alloy used for the quantitative analysis of the Pd-Ni-Co alloys. The reference spectra of the pure metals of Pd, Ni and Co taken from Ar^+-sputter cleaned foils are also shown in Figure 6.7 for comparison. The spectra of the pure Pd and Ni samples have a similar peak shape as the ones from the analyzed alloy. The peak shape of the Co $L_3M_{2,3}M_{2,3}$ region in Figure 6.7 (c) is influenced by the noise of the spectrum compared to the reference spectrum of pure Co. In the following the quantitative analysis of electron excited AES is performed and discussed for the Pd-Ni-Co alloy with unknown composition in Figure 6.7. For the quantification usually relative sensitivity factors (RSFs) are applied, which is described in Section 3.5. Relative sensitivity factors can be taken from handbooks [20], are given by the manufacturer [54] or can be determined experimentally. Table 6.1 shows different relative sensitivity factors for the selected Auger transitions of Pd, Ni and Co, which are valid for spectra measured with a 5 keV electron beam and intensities from APPHs

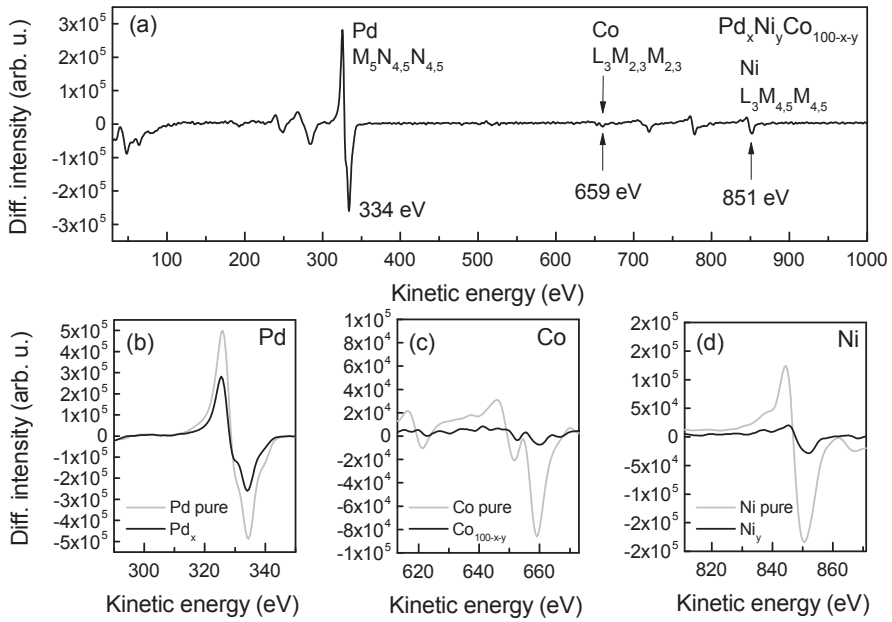

Figure 6.7: Derivative Auger electron spectrum (S9D5) of a Pd-Ni-Co alloy (a) with unknown composition and selected regions for quantitative analysis which are compared to reference spectra of the pure elements (b-d).

after 5-point differentiation. The PERSFs from the PHI AES Handbook are the most popular in AES literature and are used for basic quantitative analysis [20]. The ERSFs and AMRSFs from PHI are not officially published and are only given by the manufacturer with the instrument [54]. The PHI AMRSFs were calculated by the manufacturer from the PHI ERSFs with the matrix correction according to Equation 3.13. These three types of RSFs are implemented in the PHI MultiPak Software (Version 9.2) as databases. The BAM 6.8 PERSFs are based on the mea-

Element			Pd	Ni	Co
Auger transition			$M_5N_{4,5}N_{4,5}$	$L_3M_{4,5}M_{4,5}$	$L_3M_{2,3}M_{2,3}$
Auger kinetic energy			334 eV	851 eV	659 eV
PHI Handbook PERSFs	S_i^{Ep}	[20]	2.860	1.048	0.406
PHI ERSFs	S_i^{E}	[54]	0.768	0.281	0.109
PHI AMRSFs	S_i^{Av}	[54]	0.717	0.195	0.077
BAM 6.8 (2013) PERSFs	S_i^{Ep}		2.356	0.736	0.280

Table 6.1: Relative sensitivity factors available for the Pd, Ni and Co Auger transitions for 5 keV electron beam excitation: Pure Element RSFs, Element RSFs and Average Matrix RSFs.

surement of pure Pd, Ni and Co foils after Ar^+sputter cleaning. The intensities obtained from APPHs after 5-point differentiation were normalized to the APPH of the Cu $L_3M_{4,5}M_{4,5}$ Auger transition at 922 eV, which was set to unity. This procedure is analogue to the procedure given in the AES Handbook [20]. The results based on the experimental PERSFs from BAM 6.8 are expected to be more reliable than the ERSFs given by PHI, because the intensities were measured with the same experimental setup and under the same conditions as for sample analysis.

6.2.1 Application of the matrix correction of Sekine et al.

The procedure of the matrix correction, presented in Section 3.5 is applied to the Pd-Ni-Co alloy shown in Figure 6.7 [44]. The k-values, k_{Pd}, k_{Ni}, k_{Co}, according to Equation 3.14, are calculated from APPHs in Table 6.2.

Element		Pd	Ni	Co
Auger transition		$M_5N_{4,5}N_{4,5}$	$L_3M_{4,5}M_{4,5}$	$L_3M_{2,3}M_{2,3}$
Auger kinetic energy		334 eV	851 eV	659 eV
Pure Pd	I^0_{Pd}	987513		
Pure Ni	I^0_{Ni}		308398	
Pure Co	I^0_{Co}			117289
$Pd_xNi_yCo_{100-x-y}$	I_i	541765	48892	13894
k-values	I_i/I^0_i	0.5486	0.1585	0.1185

Table 6.2: AES Peak-to-peak heights (APPHs) of pure Pd (I^0_{Pd}), Ni (I^0_{Ni}), Co (I^0_{Co}) and a Pd-Ni-Co ($I_{i=Pd,Ni,Co}$) alloy taken at 5 keV electron beam voltage and 20 nA current and k-values calculated for the Pd-Ni-Co alloy in Figure 6.7

The k-values in Table 6.2 are used to calculate the 1^{st} approximation of the composition of the alloy, where the matrix correction factors for the three elements are $F_i = 1$ in Equation 3.16. The concentration of each element is given by its k-value divided by the sum of all k-values:

$$X_{Pd} = \frac{k_{Pd}}{k_{Pd} + k_{Ni} + k_{Co}} = 0.665 \tag{6.1}$$

$$X_{Ni} = \frac{k_{Ni}}{k_{Pd} + k_{Ni} + k_{Co}} = 0.192 \tag{6.2}$$

$$X_{Co} = \frac{k_{Co}}{k_{Pd} + k_{Ni} + k_{Co}} = 0.143 \tag{6.3}$$

The 1^{st} approximation of the alloy composition is $\mathbf{Pd_{66.5}Ni_{19.2}Co_{14.3}}$ (at.%) based on the calculated k-values. The next step is to calculate the atomic density of the alloy, N, the backscattering correction factors (BCFs) [47], R_{Pd}, R_{Ni}, R_{Co} and the inelastic mean free path (IMFP) [57], λ_{Pd}, λ_{Ni}, λ_{Co} for this specific alloy composition and the same Auger transitions used for the quantitative analysis. The atomic

Element	Pd	Ni	Co
Auger transition	$M_5N_{4,5}N_{4,5}$	$L_3M_{4,5}M_{4,5}$	$L_3M_{2,3}M_{2,3}$
N_i^0(atoms/cm^3)	6.791×10^{22}	9.091×10^{22}	9.095×10^{22}
R_i^0	2.062	1.672	1.700
λ_i^0 (Å)	7.977	13.301	11.310
1^{st} approximation		$\mathbf{Pd_{66.5}Ni_{19.2}Co_{14.3}}$	
N (atoms/cm^3)		7.562×10^{22}	
N_i^0/N	0.898	1.202	1.203
R_i	1.921	1.723	1.672
R_i^0/R_i	1.073	0.970	1.017
λ_i (Å)	6.602	12.417	10.278
λ_i^0/λ_i	1.208	1.071	1.100
F_i^{1st}	1.165	1.250	1.346
2^{nd} approximation		$\mathbf{Pd_{64.1}Ni_{19.9}Co_{16.0}}$	
N (atoms/cm^3)		7.617×10^{22}	
N_i^0/N	0.892	1.194	1.195
R_i	1.926	1.708	1.677
R_i^0/R_i	1.071	0.979	1.014
λ_i (Å)	6.609	12.432	10.290
λ_i^0/λ_i	1.207	1.070	1.099
F_i^{2nd}	1.152	1.250	1.330
3^{rd} approximation		$\mathbf{Pd_{64.0}Ni_{20.0}Co_{16.0}}$	

Table 6.3: The 1^{st}, 2^{nd} and 3^{rd} approximation of the composition of the alloy based on the matrix correction procedure of Sekine *et al.* [44]. The atomic densities, N, backscattering correction factors, R, IMFPs, λ, are given to calculate the matrix corrections factors, F_i.

density of the alloy is calculated by Equation 3.18. Further the values for the pure elements (atomic densities: N^0_{Pd}, N^0_{Ni}, N^0_{Co}, BCFs: R^0_{Pd}, R^0_{Ni}, R^0_{Co}, IMFPs: λ^0_{Pd}, λ^0_{Ni}, λ^0_{Co}) are necessary to calculate the correction factors, N^0_i/N, R^0_i/R_i, λ^0_i/λ_i, which lead to the matrix correction factors using Equation 3.17. The first set of matrix correction factors, F^{1st}_{Pd}, F^{1st}_{Ni}, F^{1st}_{Co}, and the k-values are used to calculate a 2^{nd} approximation of the alloy composition with Equation 3.16: $\mathbf{Pd}_{64.1}\mathbf{Ni}_{19.9}\mathbf{Co}_{16.0}$. The second set of matrix correction factors, F^{2nd}_i, can be calculated based on the second composition. Then the second set of matrix correction factors, F^{2nd}_i, together with the k-values lead to the 3^{rd} approximation of the composition of the alloy: $\mathbf{Pd}_{64.0}\mathbf{Ni}_{20.0}\mathbf{Co}_{16.0}$.

All values and the results of this procedure are given in Table 6.3. The matrix correction factors F_i for Pd, Ni and Co are around 1. The values for N, R and λ stayed almost the same after the second iteration and so the matrix correction factors change only slightly. The second set of matrix correction factors had almost no influence on the calculation of the 3^{rd} composition. No further iterations were done since the third composition is nearly identical to the second one. The 3^{rd}-alloy composition $\mathbf{Pd}_{64.0}\mathbf{Ni}_{20}\mathbf{Co}_{16.0}$ is considered as the final result of the Sekine *et al.* algorithm [44].

6.2.2 Comparison of the quantitative results

The quantitative analysis of a $Pd_xNi_yCo_{100-x-y}$ alloy with unknown composition is presented using the available relative sensitivity factors from PHI, experimental sensitivity factors from BAM 6.8 and application of the matrix correction procedure from Sekine *et al.* [44]. Table 6.4 shows the quantitative results based on the different relative sensitivity factors given in Table 6.1 and the matrix correction. The starting point of the comparison is the composition $\mathbf{Pd}_{70.0}\mathbf{Ni}_{17.3}\mathbf{Co}_{12.7}$ calculated with the PHI ERSFs which are used in the standard procedure for quantification of the Pd-Ni-Co alloys in this work. Surprisingly the PHI ERSFs give the same results as the PERSFs in the AES Handbook. The AMRSFs reduce the Pd concentration by about 6.3 at.%. The concentration of Ni increases by about 3.8 at.% and the concentration of Co is 2.5 at.% higher. The application of experimental PERSFs measured in the BAM 6.8 laboratory lowers the Pd concentration by about 3.5 at.%, whereas Ni and Co are increased by about 1.9 at.% and 1.6 at.%, respectively. The results of the matrix correction are in between those of the AMRSFs and the BAM PERSFs. The final alloy composition after matrix correction is $\mathbf{Pd}_{64}\mathbf{Ni}_{20.0}\mathbf{Co}_{16.0}$. Compared to the results of the PHI ERSFs the Pd concentration is 6 at.% lower,

Element		Pd	Ni	Co
Auger transition		$M_5N_{4,5}N_{4,5}$	$L_3M_{4,5}M_{4,5}$	$L_3M_{2,3}M_{2,3}$
Electron kinetic energy		334 eV	851 eV	659 eV
AES Handbook PERSFs	S_i^{Ep}	70.0	17.3	12.7
PHI ERSFs	S_i^{E}	70.0	17.3	12.7
PHI AMRSFs	S_i^{Av}	63.7	21.1	15.2
BAM 6.8 (2013) PERSFs	S_i^{Ep}	66.5	19.2	14.3
after matrix correction		64.0	20.0	16.0

Table 6.4: Comparison of the quantitative results (at.%) for the clean Pd-Ni-Co alloy shown in Figure 6.7. The matrix correction (based on BAM 6.8 PERSFs) was performed after Sekine *et al.* [44].

Ni is 2.7 at.% and Co 3.3 at.% higher. The PHI ERSFs seem to overrate the Pd concentration in the alloy. The uncertainty range of the PHI PERSFs can be estimated in relation to the results of the matrix correction. The concentrations found with the PHI ERSFs differ for Pd by about 9 rel.%, for Ni by about 16 rel.% and for Co by about 26 rel.%. The highest content of Ni is found with the AMRSFs and the highest content of Co is found after the matrix correction.

6.2.3 Conclusion

The influence of the experimental setup on the quantitative results is demonstrated by the BAM 6.8 PERSFs. The iterative matrix correction is extensive, but the results have probably the highest accuracy. The quality of the AMRSFs from PHI is unknown and has to be evaluated in further studies with certified reference materials. Nevertheless, the PHI ERSFs were used for the standard quantitative analysis of AES data in this thesis.

7 Thin film analysis by EDX/STRATAGEM

EDX is a microanalysis method which gives qualitative and quantitative information about the chemical composition at the scale of the excitation volume. The analysis of thin films by EDX is enabled by the STRATAGEM software package by SAMx (France) for quantitative X-ray microanalysis. In this thesis STRATAGEM (Version 2.6) is used for the simultaneous determination of composition and mass thickness of thin films on a substrate, more precisely for the determination of the composition as well as the nanoscaled film thickness of Pd-Ni-Co thin film alloys deposited on silicon wafers [63]. Beyond that, the procedure was optimized for high-throughput screening of Pd-Ni-Co thin film alloy libraries on Si.

7.1 Characterization of a Pd-Ni-Co alloy by EDX

A single alloy composition has been investigated within a Pd-Ni-Co thin film alloy library deposited on silicon with setup 1 (see Chapter 2, Figure 2.1). The EDX spectra in this thesis were taken with a Bruker XFlash 5010 SDD energy-dispersive X-ray spectrometer attached to a SEM Carl Zeiss Supra 40 (see Chapter 4).

A typical EDX spectrum taken at an electron beam energy of 15 keV is shown in the energy range from 0 keV - 8 keV in Figure 7.1 (a). The detailed regions of the Si Kα line of the substrate and Pd Lα, Ni Kα and Co Kα lines from the alloy layer are shown in Figure 7.1 (b-d). Here, the spectrum was analyzed using the EDXTOOLS software package as developed by Procop [90]. In Figure 7.1 (a) the calculated bremsstrahlung background is shown in gray. Solid lines represent positions and relative intensities of characteristic X-ray peaks of each element. The main features in the spectrum are the very intense Si Kα line at 1.74 keV emitted by the substrate and the intense Pd Lα line at 2.84 keV of the main component in the alloy within the Pd L-series. The X-ray lines Co Kα at 6.93 keV and Ni Kα at 7.48 keV have very low intensities because of their low concentrations in the alloy layer.

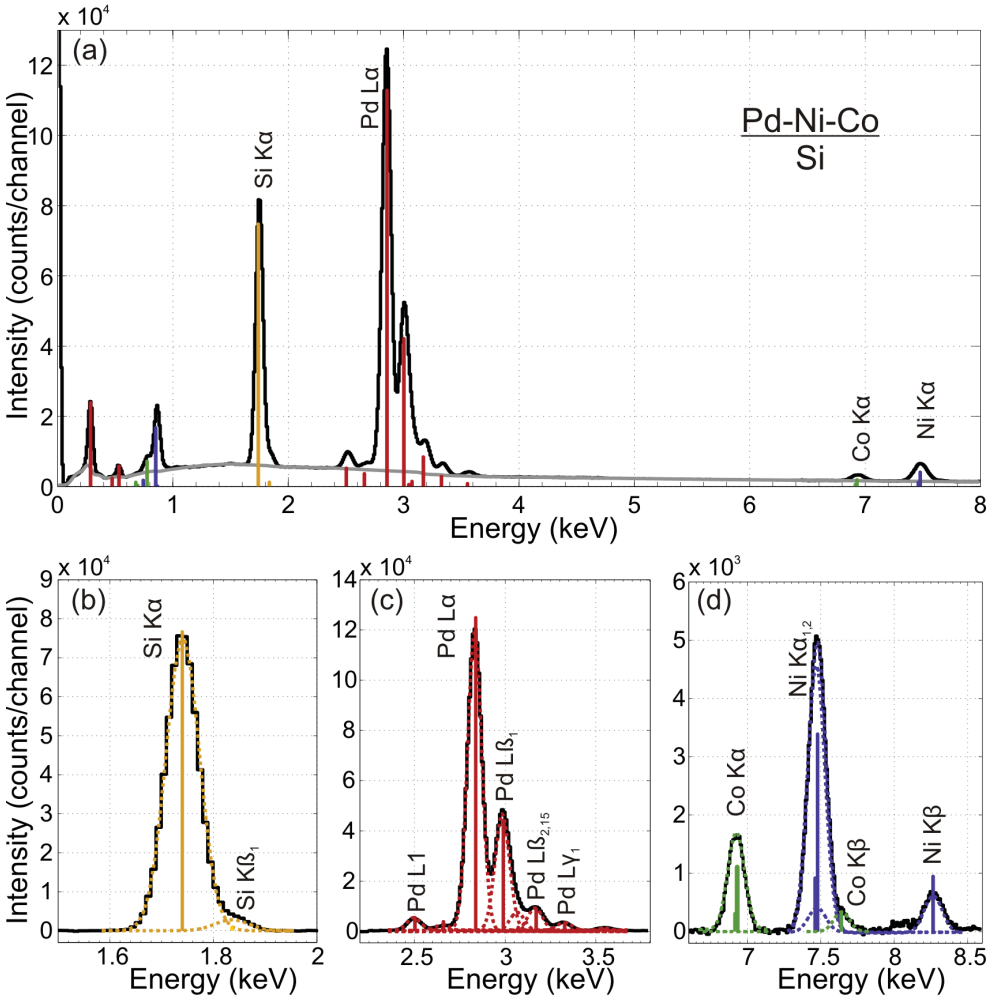

Figure 7.1: A typical EDX spectrum of a Pd-Ni-Co thin film alloy on silicon substrate acquired with 15 keV electron beam energy. (a) shows the overview spectrum and (b-d) show the regions of interest with the characteristic X-ray emission lines of the Si K-series (b), the Pd L-series (c), the Co K-series and Ni K-series (d) as deconvoluted after background subtraction.[1] The colored solid lines indicate the peak positions and relative peak intensities of each element.

X-ray lines below 1 keV have not been taken into account for elemental analysis and quantification. After background subtraction the intensities of the X-ray lines as net peak areas are used for the calculation of k-values for the quantitative analysis of a Pd-Ni-Co thin film alloy in the following Section 7.2.

[1] X-RAY DATA BOOKLET, http://xdb.lbl.gov (2015).

7.2 Application of the STRATAGEM software

The STRATAGEM fitting routine is based on the determination of experimental k-values, which were already introduced for the AES matrix correction procedure in Section 3.5. STRATAGEM needs k-values measured at different excitation energies, E_0, of the electron beam to calculate composition and mass thickness. In Equation 7.1 they are given by the ratio of the net intensity of an X-ray line of an element in the sample, I_i, to the net intensity of the X-ray line measured from the pure element, I_i^0, as the standard after normalization to live time and electron beam current.

$$k_i = \frac{I_i}{I_i^0} \tag{7.1}$$

The net intensity of an X-ray line is the peak area after background subtraction. The net intensities of the standards have been derived from polished pure Pd, Ni, Co foils and a Si-wafer. Here, the spectra were acquired with a live time of 600 s and the electron beam current was measured before and after spectrum acquisition. All spectra were measured under the exact same experimental conditions with the same instrumental settings. For the evaluation of the STRATAGEM data reduction k-values at six electron beam energies (10, 12, 15, 20, 25 and 30 keV) for Pd Lα, Ni Kα, Co Kα and Si Kα X-ray lines were determined. The calculated k-values are shown in Table 7.1.

E_0 (keV)	Pd Lα	Ni Kα	Co Kα	Si Kα
10	0.3947	0.1181	0.0319	0.3601
12	0.2473	0.0666	0.0148	0.5100
15	0.1673	0.0369	0.0081	0.5742
20	0.0969	0.0181	0.0042	0.6492
25	0.0748	0.0114	0.0029	0.6584
30	0.0503	0.0059	0.0007	0.6951

Table 7.1: Calculated k-values of a Pd-Ni-Co thin film alloy deposited on Si with unknown composition and film thickness for six electron beam energies.

The k-values of the alloy layer from Pd Lα, Ni Kα and Co Kα are decreasing while the k-values of Si Kα from the bulk substrate are increasing with electron beam energy. The k-values are getting very small at high electron beam energies, because of the lower contribution of the thin film to the signal intensity.

7.2.1 Simultaneous determination of composition and thickness

The k-values are entered into the STRATAGEM software corresponding to the experimental configuration. The calculation of the elemental mass thickness (μ/cm^2) is based on the work of Pouchou and Pichoir [91]. The physical approach of the procedure relies on the variation of the interaction volume of the electron beam within the sample, a thin film on a substrate, achieved by variation of the excitation energy. Therefore the X-ray depth distribution functions, $\phi(\rho z)$, are calculated based on the experimental k-values for different excitation energies. Thereby the matrix correction is achieved. Usually 4 to 10 iterations are necessary until the calculated data by STRATAGEM fits to the experimental data set. In detail k-values from Table 7.1 are plotted against the electron beam energy, E_0, and fitted with calculated k-values, where mass thickness and elemental composition are free parameters. In principal, only one set of experimental k-values of one excitation energy would be enough, but the more experimental k-values are used the higher is the degree of accuracy of the thin film analysis. Figure 7.2 shows the fitted k-values for Si Kα, Pd Lα, Ni Kα and Co Kα. They are in a good agreement with the experimental ones, but the fit for the Si Kα k-values shows a somewhat larger deviation at high excitation energies. Next to the composition STRATAGEM calculates the mass thickness of the film, here 73.9 μg/cm^2. With an assumed layer density of 12.0 g/cm^3, the thickness of the $\mathbf{Pd}_{74.2}\mathbf{Ni}_{21.0}\mathbf{Co}_{4.8}$ layer on Si is about 62 nm.

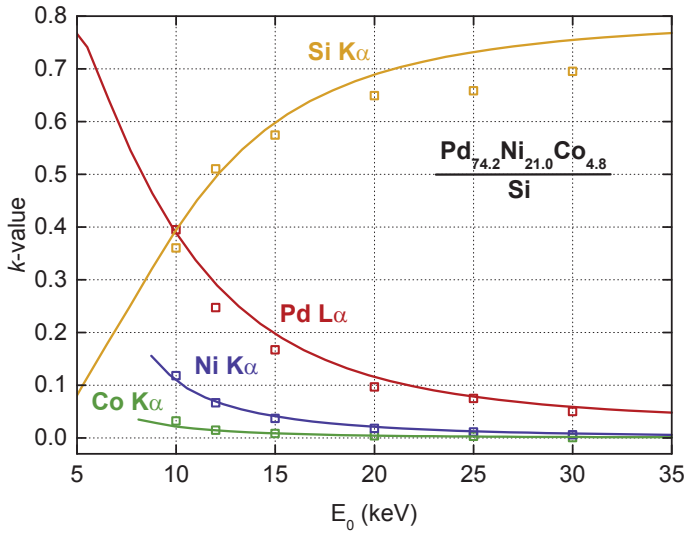

Figure 7.2: The experimental k-values from Table 7.1 were fitted by STRATAGEM. The composition of the Pd-Ni-Co thin film alloy layer on Si was determined as $\mathbf{Pd}_{74.2}\mathbf{Ni}_{21.0}\mathbf{Co}_{4.8}$.

7.2.2 Verification of the STRATAGEM results

The quantitative results from EDX/STRATAGEM of the complete layer are compared to the results from AES and XPS, which are shown in Table 7.2. They are in good agreement even if AES and XPS address the surface composition within a few nanometer. The AES results and the EDX/STRATAGEM results are very similar. Hence, the bulk and surface composition are almost equal here. The XPS data show a lower concentration of Ni and a slightly higher concentration of Co. A reason for that could be the use of the relative sensitivity factors for quantification. The given uncertainties were derived from References [92, 93].

Method	Pd (at.%)	Ni (at.%)	Co (at.%)
EDX (± 5 rel.%)	74.2	21.0	4.8
AES (± 7 rel.%)	73.9	21.0	5.1
XPS (± 7 rel.%)	74.9	16.6	8.5

Table 7.2: Comparison of the quantitative results in at.% of EDX/STRATAGEM with AES and XPS.

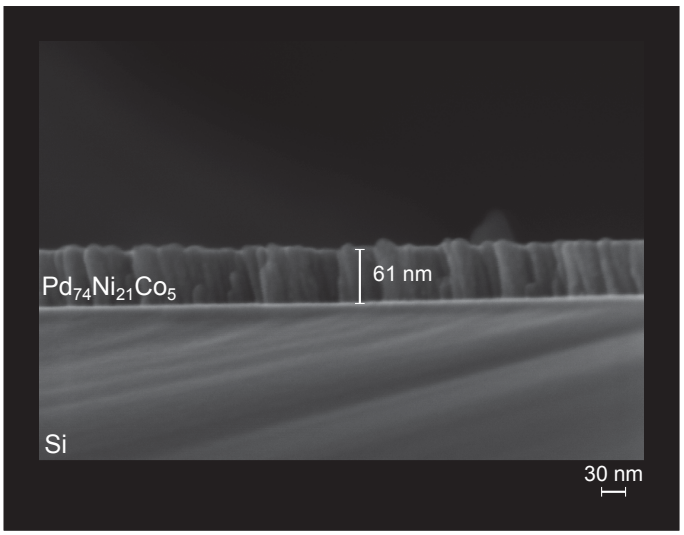

Figure 7.3: SEM micrograph of the cross section after fracture of the investigated Pd-Ni-Co thin film alloy on silicon with a thickness of about 61 nm.

AES spectra were taken at 5 keV electron beam energy and 20 nA beam current. The analyzed area was 5 x 5 μm^2. The MNN Auger electron transitions of Pd (334 eV) and the LMM transitions of Ni (851 eV) and Co (659 eV) were used for quantitative analysis together with the PHI ERSFs in Table 6.1.

XPS was performed using a VG Scientific ESCALAB 200X electron spectrometer using an Al Kα X-ray source with a spot size about 5 mm. For data analysis the intensities of the Pd $3d_{5/2}$, Ni $2p_{3/2}$ and Co $2p_{3/2}$ peaks were determined after Shirley background subtraction. The standard free quantification of the XPS data was realized by using the respective Thermo Avantage data system routine and embedded sensitivity factors.

The SEM micrograph in Figure 7.3 shows the cross section of the investigated sample after fracture. The film thickness, measured with the calibrated SEM, is about 61 nm. The interface between the alloy layer and the Si substrate is sharp and the film thickness is in excellent agreement with the EDX/STRATAGEM analysis results for the Pd-Ni-Co thin film.

7.2.3 High-throughput screening procedure

The quantitative EDX data analysis by STRATAGEM was applied for high-throughput screening (HTS) of ternary Pd-Ni-Co thin film alloy libraries. Next to the automation of EDX spectra acquisition, which was introduced later during the thesis with an upgrade of the spectrometer software, the data reduction had to be optimized. Therefore the number of electron beam energies was reduced to three (15, 20 and 25 keV). The Bruker Esprit Software (Version 1.9) was used for automated background subtraction and calculation of the net peak areas. The integrated intensities are normalized to the live time of 500 s and the electron beam current to get the net intensities to calculate the k-values. The net intensities of the pure bulk elements, I_i^0, were determined again.

In this way the bulk composition Pd-Ni-Co thin film alloy library was successfully characterized by HTS-EDX with 30 measurement points. The results are presented in Section 8.1, where the bulk composition is compared to the surface composition characterized by HTS-AES.

7.2.4 Conclusion

The elemental composition and thickness of ternary Pd-Ni-Co alloy thin films can be analyzed accurately by EDX/STRATAGEM based data reduction. The quantitative results of the thin film are in good agreement with those obtained from AES and XPS of the surface. The EDX/STRATAGEM thickness determination for a thin film of about 60 nm was validated by SEM micrograph of the cross section of the sample.

8 Surface segregation in Pd-Ni-Co thin film alloy libraries

In this chapter the results of the high-throughput screening (HTS) studies on two ternary thin film alloy libraries using AES and EDX/STRATAGEM are presented. Both techniques allow the determination of the local alloy composition in a thin film library because of the very high spatial resolution achieved by the focused electron beam. The option to run the instruments automatically was applied to raster the alloy libraries. Composition maps from the surface and the bulk of the alloy libraries are obtained to characterize surface segregation phenomena in the Pd-Ni-Co alloy system. A model alloy library with a wide composition range and an applied library with a very limited composition range and very high Pd content for hydrogen sensing purposes are presented. The goal of this study was the investigation of surface segregation phenomena in the ternary Pd-Ni-Co alloy system induced by the exposition of the samples to reactive gas atmospheres, such as ambient air, H_2 and H_2S, at room temperature and atmospheric pressure. In this study special interest is paid to the concentrations of oxygen and sulfur on the surface, which could be quantified by AES. Furthermore there is carbon on the sample surface, which could not be quantified due to the overlap with the Pd MNN Auger series. The surface contamination is related to the exposure of the sample to ambient air, which leads to the adsorption of hydrocarbons and carbon oxides.

Under inert conditions the enrichment of Pd would be expected on the surface, but due to the exposure of the alloy system to reactive gas atmospheres the surface segregation is reversed, which is discussed in Section 8.3. The surface and bulk chemical states of a Pd-Ni-Co thin film alloy related to air exposure and H_2S poisoning were investigated in detail by XPS and HAXPES (Section 9.2).

8.1 Model Pd-Ni-Co alloy library with a wide composition range

A model thin film alloy library with a wide composition range was deposited on a HF-etched Si wafer with the three sputter sources setup. Any ternary alloy composition can be achieved with that system by varying the deposition parameters. Here, the parameters of the three sputter sources setup were optimized until an alloy library with maximized composition range could be deposited on a single silicon wafer with a size of 30 × 25 mm^2 (see Section 2.2). The surface and bulk composition of the alloy library was analyzed in this experiment by AES and EDX to study the surface segregation phenomena in the Pd-Ni-Co alloy system. The EDX data sets were reduced using the STRATAGEM software [63].

High-throughput screening was performed with 30 (6 × 5) measurement points on the sample over an area of 25 × 20 mm^2. Surface and bulk composition maps were created from quantitative results based on AES and EDX/STRATAGEM. AES was performed with a 5 keV electron beam and 20 nA beam current. The quantitative AES results were calculated with the PHI ERSFs [54]. The data reduction procedure of EDX/STRATAGEM, which was presented in Chapter 7, was adapted for HTS purposes. Therefore three different electron beam energies (15, 20 and 25 keV) were chosen and the spectra taken with a live time of 500 s. The electron beam current was monitored before and after the measurement of the alloy library for each excitation energy. For both methods a combined uncertainty of $u_c = \pm$ 10 rel.% for the measurements was estimated based on expert knowledge.[1] The experiment was conducted as follows:

1. HTS-AES, HTS-EDX
2. **Hydrogen exposure:** pure H_2 for 5 h
3. HTS-AES, HTS-EDX
4. **Poisoning:** 500 ppm H_2S in dry syn. air for 2 h
5. AES-HTS, HTS-EDX

In step 1 the alloy library was analyzed in the air exposed as-received state. The sample was inevitably exposed to ambient air during mounting the sample for the different analytical instruments. In step 2 the alloy library was exposed to pure hydrogen under ambient conditions. In step 3 the alloy library was screened at the exact same measurement positions as in step 1. In step 4 the sample was poisoned by hydrogen sulfide with a concentration of 500 ppm in dry synthetic air under ambient conditions and in step 5 the poisoned state of the alloy library was analyzed.

[1] Personal communication with Dr. W. E. S. Unger

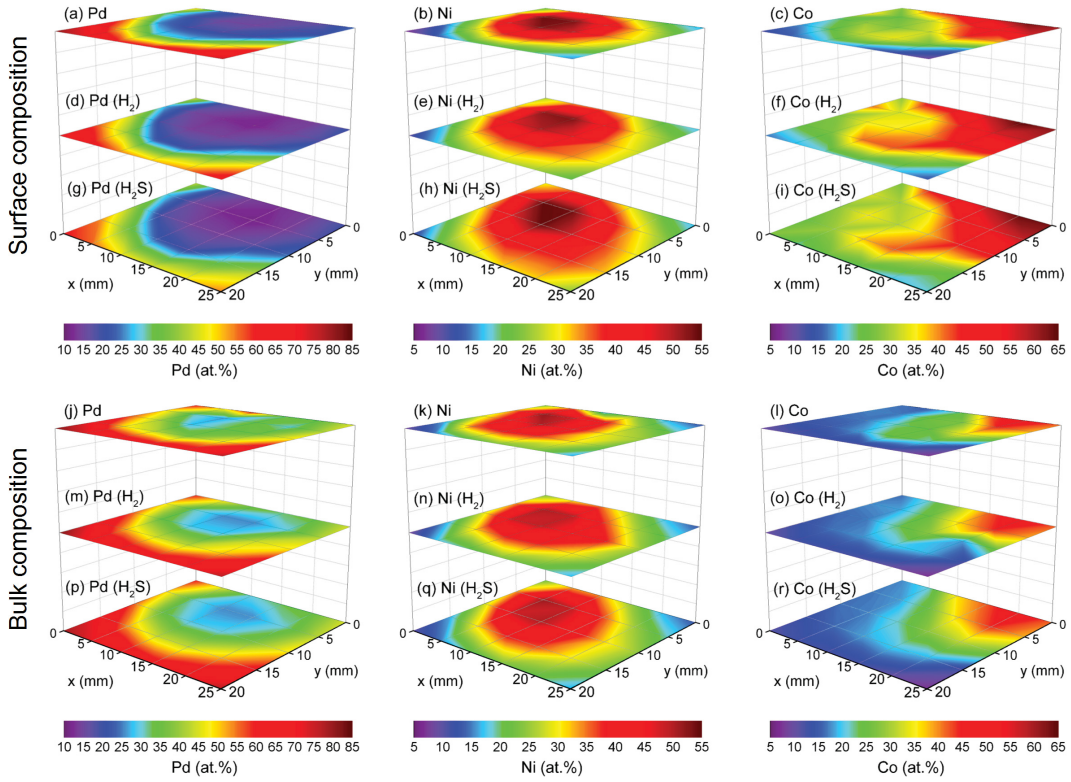

Figure 8.1: Surface and bulk composition maps (contour plots) of the Pd-Ni-Co model thin film alloy library based on a 6 x 5 pattern over an area of 25 × 20 mm^2. The surface composition by AES of the alloy library is shown as-received (a-c), after H_2-exposure (d-f) and after H_2S-poisoning (g-i). The bulk composition of the sample by EDX/STRATAGEM, taken analogue to the AES data, is shown as-received (j-l), after H_2-exposure (m-o) and after H_2S-poisoning (p-r).

Figure 8.1 shows the surface and bulk composition maps obtained from AES and EDX/STRATAGEM data, respectively. The maps illustrate the elemental distribution in the Pd-Ni-Co model alloy library. There are areas where the Pd, Ni and Co concentrations are very high, colored dark red, which correspond to the alloy compositions $\mathbf{Pd_{80}Ni_7Co_{13}}$, $\mathbf{Pd_{21}Ni_{54}Co_{25}}$ and $\mathbf{Pd_{17}Ni_{20}Co_{63}}$ on the surface. The areas where the concentration of an element is rather low, with respect to its composition range, it is colored violet-blue. As first step the alloy library was screened as-received. The concentration range of Pd is about 15 − 80 at.%, of Ni about 7 − 54 at.% and of Co about 9 − 63 at.%, see Figure 8.1 (a-c). The thin film alloy library has a rather steep compositional gradient. As second step in this experiment the sample was exposed ex-situ to pure hydrogen in a flow box at RT and

atmospheric pressure. The surface depletes of Pd and a simultaneous Ni and Co enrichment is observed in Figure 8.1 (d-f). As third step the sample was poisoned with H_2S in dry synthetic air for 2 h, whereby a further depletion of Pd on the surface and an inverse co-segregation of Ni and Co to the surface (g-i) were observed. Analogue to the HTS-AES measurements a HTS-EDX/STRATAGEM procedure was used to determine the bulk composition of the thin film alloy library exactly at the same positions where the surface composition by AES was measured before. So the alloys surface composition can be directly compared to their bulk compositions over the whole composition range. The HTS-EDX/STRATAGEM results are presented in Figure 8.1 (j-r). Compared to the surface composition maps a clear enrichment of Pd (j) in the bulk is found. The surface and bulk concentration of Ni (k) is similar. On the other hand there is a strong depletion of Co (l). The color code is the same as for the surface composition maps. After hydrogen treatment (m-o) and also after hydrogen sulfide poisoning (p-r) the bulk composition stays rather stable. The film thickness of the alloy library is in between 12 - 32 nm according to the STRATAGEM data reduction.

More detailed information are derived from surface vs. bulk composition plots in Figure 8.2. An up or down shift of the squares describes the change in the surface composition and a shift to the left or right describes changes in the bulk composition. The bisecting lines indicate where surface and bulk composition are equal. Figure 8.2 (a) shows that in the as-received state (blue) of the alloy library up to $X_{Pd} < 50\ at.\%$ the concentration of Pd at the surface is lower than in the bulk. If $X_{Pd}^{bulk} > 50\ at.\%$ the Pd surface and bulk concentrations are similar. After H_2-exposure (red) the surface concentrations decrease above $X_{Pd}^{bulk} > 50\ at.\%$ (bulk). Below that the Pd-concentrations decrease less. After H_2S-poisoning (green) the surface concentrations decrease further above $X_{Pd}^{bulk} > 50\ at.\%$. In the low concentration range the concentrations stay stable. As seen before in the surface composition maps the bulk concentration do not change significantly. The shifts corresponding to the bulk composition due to gas exposure are in general smaller compared to shifts corresponding to changes in the surface composition. In Figure 8.2 (b) the surface segregation plot of Ni is shown. In the as-received state (blue) of the alloy library the Ni surface concentrations with respect to the bulk concentrations in the range of $X_{Ni}^{bulk} > 40\ at.\%$ are slightly higher than compared to the range $X_{Ni}^{bulk} < 40\ at.\%$. After H_2-exposure (red) the Ni surface concentrations increase and are even more enriched after H_2S-poisoning (green) in the range $X_{Ni}^{bulk} < 40\ at.\%$. If $X_{Ni}^{bulk} > 40\ at.\%$ the surface concentrations are not changing significantly.

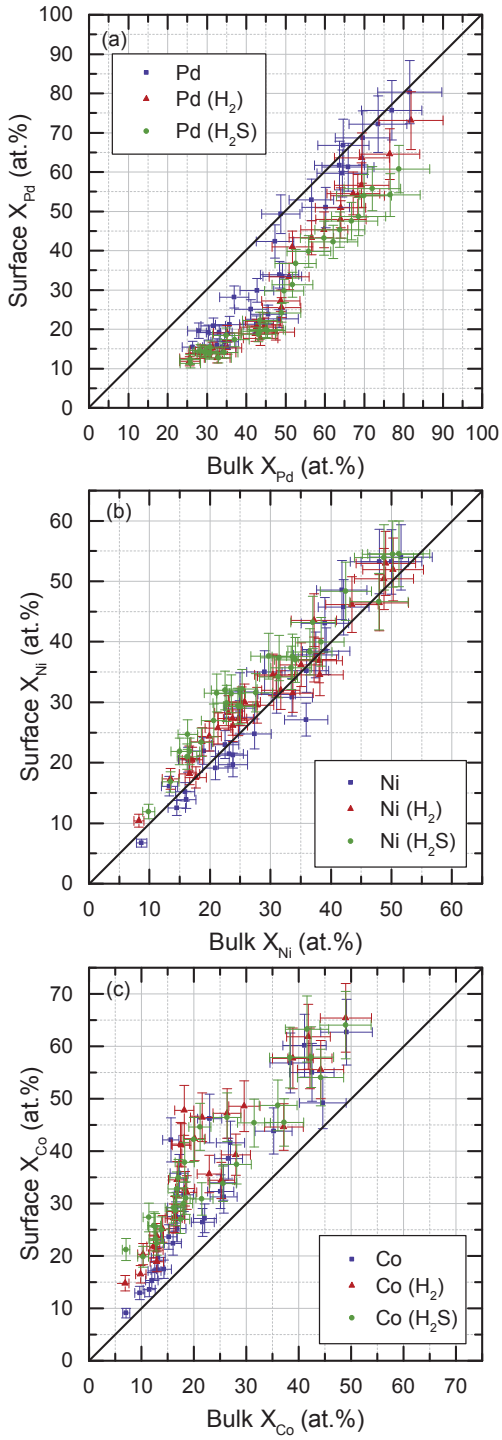

Figure 8.2: Surface segregation illustrated by surface (AES, $u_c = \pm$ 10 rel.%) vs. bulk concentration (EDX/STRATAGEM, $u_c = \pm$ 10 rel.%) plots of Pd (a), Ni (b) and Co (c) from the alloy library shown in Figure 8.1. In each plot blue indicates the as-received state, red the state after hydrogen exposure (H_2) and green the poisoned state (H_2S).

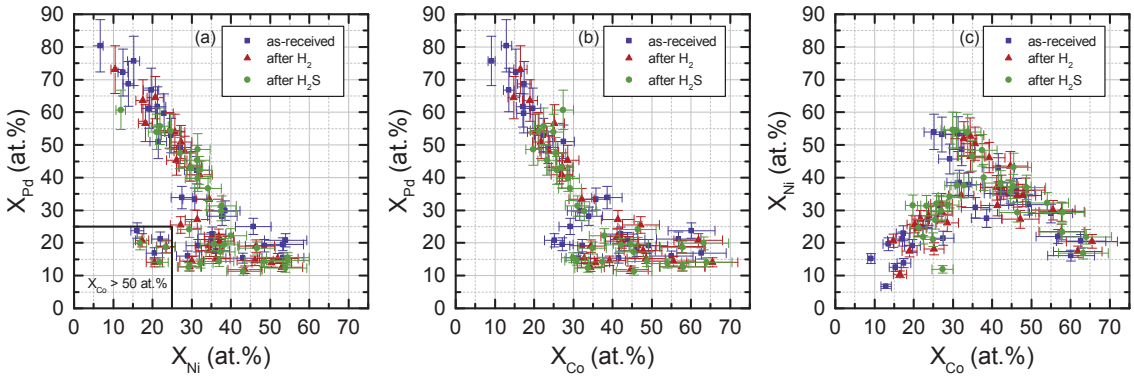

Figure 8.3: Surface concentrations based on AES data ($u_c = \pm$ 10 rel.%) of Pd, Ni and Co plotted against each other: (a) Pd vs. Ni, (b) Pd vs. Co, (c) Ni vs. Co.

Figure 8.2 (c) shows the surface segregation plot of Co. In the as-received state the alloy library already shows a Co-enriched surface over the whole concentration range. If $X_{Co}^{bulk} > 20$ *at.*% the surface is even more enriched with Co compared to the concentration range $X_{Co}^{bulk} < 20$ *at.*%. With the gas procedures (red and green) the surface enrichment of Co increases slightly.

Figure 8.3 shows the correlations of Pd, Ni and Co to each other on the surface and their change due to the reactive gas treatments. In Figure 8.3 the Pd concentrations are plotted against the Ni (a) and Co (b) concentrations. The Pd concentrations on the surface are going down with the increase of the Ni and Co concentrations. Both gas treatments lead to a decrease of the Pd concentration from $X_{Pd} = 80$ *at.*% to $X_{Pd} = 60$ *at.*%. If $X_{Pd} < 60$ *at.*%, the changes of the concentrations are only small. In Figure 8.3 (c) the Ni concentrations are plotted against the Co concentrations. The concentrations of Ni and Co are increasing in the range where $X_{Ni,Co} < 20$ *at.*%. At high Ni concentrations, where $X_{Ni} > 40$ *at.*% and $X_{Co} \approx 25$ *at.*%, an increase of the Co concentrations is observed after the gas treatments. The most reactive region on the surface of the alloy library is where $X_{Pd} > 60$ *at.*%. Furthermore composition changes were found for $X_{Ni} > 40$ *at.*%.

8.1.1 The presence of oxygen on the surface

As seen in the results of the as-received state, the alloy library shows already surface segregation phenomena due to air exposure. In addition to the alloy constituents oxygen is clearly present on the surface, which can also be quantified by AES. On the other hand the binding sites of oxygen could not be resolved by AES. There are

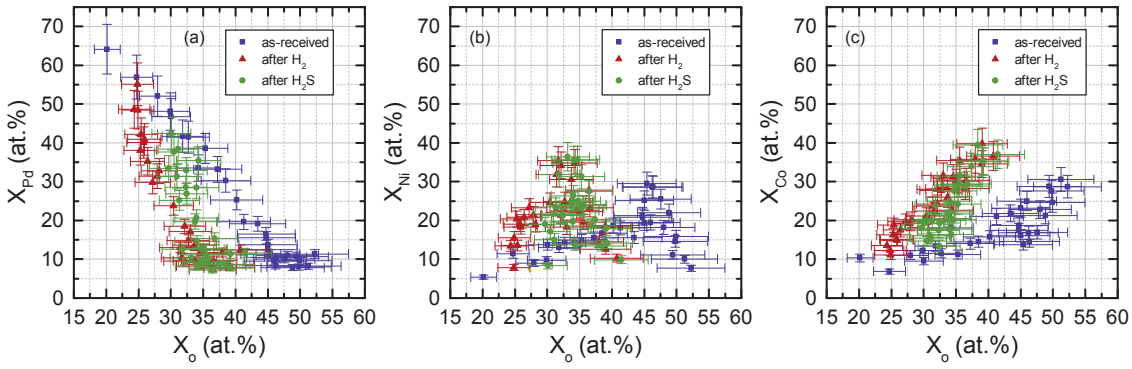

Figure 8.4: AES based surface concentration profiles ($u_c = \pm 10$ rel.%) of Pd, Ni and Co in relation to the oxygen concentration as-received, after hydrogen (H_2) and after sulfur poisoning (H_2S).

probably contributions from metal oxides and metal hydroxides to the oxygen signal arising from exposing the alloy library inevitable to ambient air, which has been kept as short as possible during the whole experiment. The oxygen concentration on the surface is in the range of $X_O = 20 - 52$ *at.*% and depends on the alloy composition.

In Figure 8.4 the concentrations of Pd, Ni and Co are plotted against the oxygen concentrations. In Figure 8.4 (a) the oxygen concentrations increase with an almost linear decrease of the Pd concentrations. In the as-received state the highest concentrations of oxygen, $X_O > 50$ *at.*%, are found where $X_{Pd} \approx 10$ *at.*%. After the hydrogen treatment the maximum Pd concentration is decreasing from $X_{Pd} = 64$ *at.*% to $X_{Pd} = 55$ *at.*%. After the sulfur poisoning the maximum Pd concentration decreases further to $X_{Pd} = 42$ *at.*%. At low Pd concentrations the oxygen concentrations are dropping by about 20 at.% after the hydrogen treatment. The oxygen concentration increases after the poisoning at $X_{Pd} > 20$ *at.*%. The alloy library was exposed to pure hydrogen, but poisoned with 500 ppm H_2S in synthetic air, which consists of oxygen and nitrogen. This is one of the reasons for the increase of the oxygen concentrations after poisoning, besides the exposition of the sample to ambient air. Figure 8.4 (b) shows the Ni concentrations in relation to the oxygen concentrations. In the as-received state the oxygen concentrations are increasing with the Ni concentrations from $X_{Ni} = 5$ *at.*% up to $X_{Ni} = 30$ *at.*%, where $X_O \approx 40$ *at.*%. If $X_O > 40$ *at.*%, the Ni concentrations are dropping and high Co concentrations show their influence on the oxygen concentrations. Both gas treatments result in an increase of Ni at the surface, while the changes after poisoning are smaller than after hydrogen exposure. The Ni concentration goes up to a maximum of $X_{Ni} = 36$ *at.*% after poisoning. In Figure 8.4 (c) the oxygen

concentrations are increasing together with the Co concentrations. The highest Co concentration in the as-received state is $X_{Co} = 30\ at.\%$ and increases after poisoning to $X_{Co} = 40\ at.\%$.

8.1.2 Sulfur poisoning by H_2S

As the forth step of the experiment the model alloy library was poisoned with 500 ppm hydrogen sulfide in dry synthetic air for 2h. In Figure 8.5 the differentiated Auger spectra show the measured regions of S, Pd, O, Co and Ni after hydrogen exposure and after poisoning at the spot with the highest sulfur concentration.

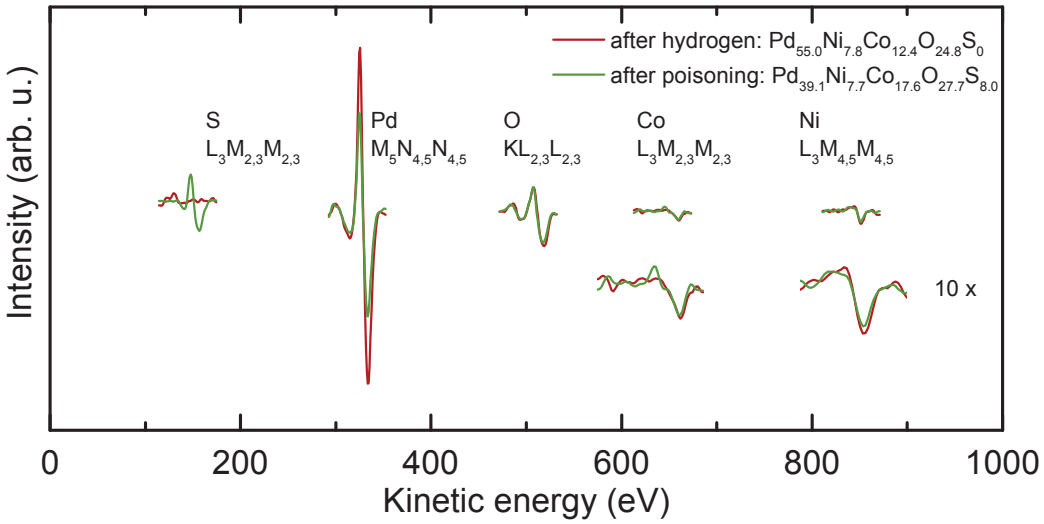

Figure 8.5: Differentiated Auger electron spectra of the regions of interest (S, Pd, O, Co, Ni) after the hydrogen treatment and after sulfur poisoning.

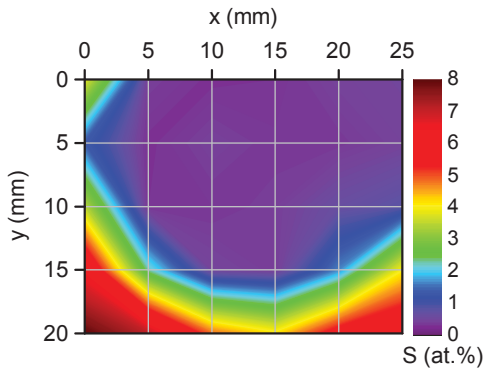

Figure 8.6: Surface composition map of sulfur by HTS-AES after H_2S-poisoning.

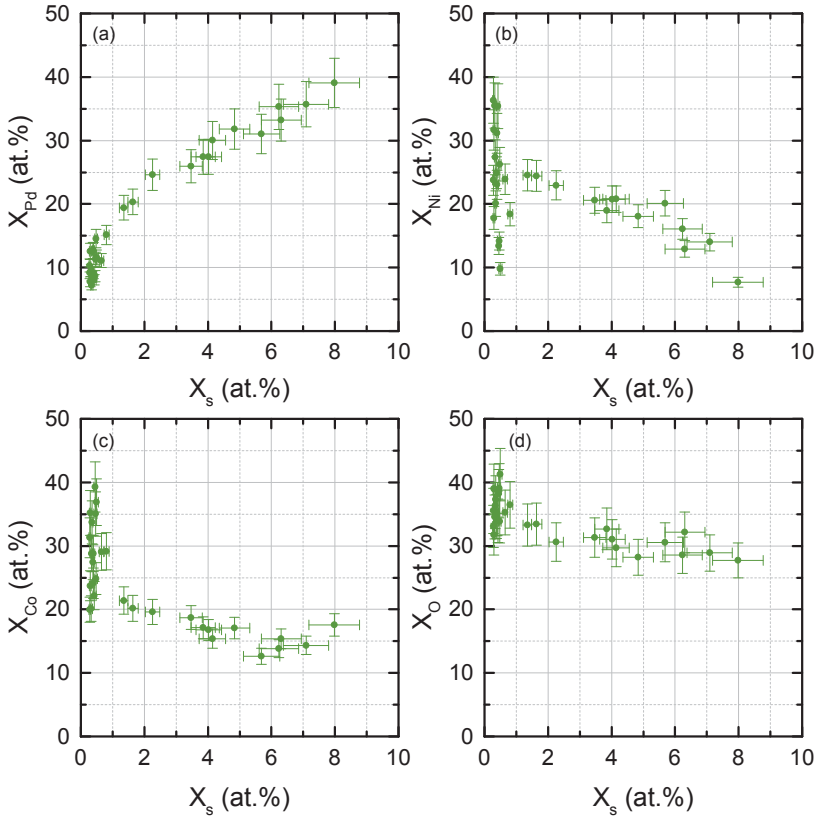

Figure 8.7: AES based surface concentration profiles ($u_c = \pm$ 10 rel.%) of Pd, Ni, Co and O in relation to the sulfur concentration after sulfur poisoning by H_2S.

The S $L_3M_{2,3}M_{2,3}$ peak is clearly present while the amplitude of the Pd $M_5N_{4,5}N_{4,5}$-transition decreases significantly. The quantitative analysis of the elements revealed a decrease of palladium, an increase of cobalt and oxygen and nickel stayed constant. The concentration of sulfur is about 8 at.%, which is the highest concentration of sulfur on the alloy library. The distribution of sulfur on the alloy library's surface is shown in Figure 8.6. The surface composition map shows a clear dependence of the sulfur concentration on the alloy composition.

Figure 8.7 summarizes the surface concentrations of Pd, Ni, Co, O and the development of the S concentrations. In Figure 8.7 (a) the sulfur concentrations are increasing with the Pd concentration in the alloy composition. While the Ni concentrations in Figure 8.7 (b) are decreasing the S concentrations are increasing. That is similar to the adsorption behavior of S with the decrease of the Co concentrations in Figure 8.7 (c). The sulfur concentrations are increasing with the decrease of the O concentrations on the surface in Figure 8.7 (d).

8.1.3 Conclusion

A model Pd-Ni-Co thin film alloy library was successfully characterized quantitatively by high-throughput screening with AES and EDX. An upscale of the number of investigated alloy compositions by a factor about ten was achieved by the combinatorial approach. Thereby surface segregation phenomena were identified already in the as-received state of the library at high Ni and Co concentrations, due to their oxidation caused by air exposure. The exposure to pure hydrogen and the poisoning of the alloy library by H_2S in synthetic air led to the co-segregation of Ni and Co to the surface and the depletion of Pd at the surface was observed. The Pd-Ni-Co bulk compositions of the alloy library remained unchanged. The oxygen concentrations on the surface correlate with the Ni and Co concentrations at the surface. The sulfur concentrations on the surface are correlated with the palladium concentrations at the surface. In general surface segregation could be tuned to suppress undesirable chemical reactions of Pd with reactive gases, which could also be attractive for the development of Pd-alloy based hydrogen separation membranes or catalysts. It can be concluded that the observed co-segregation of Ni and Co in the Pd-Ni-Co alloy system can prevent the poisoning of Pd in the bulk of the alloy, which can be useful for the development of resistant Pd-Ni-Co alloy compositions for hydrogen detection in ambient air.

8.2 Pd-Ni-Co alloy design for hydrogen sensor purposes

An Pd-Ni-Co thin film alloy library, which was deposited on the device-like multilayer substrate for hydrogen sensing purposes, was studied by HTS-AES. Therefore, the composition range of the alloy library was varied to higher Pd concentrations using the single sputter source setup. The distribution of the elements is determined by the position of the sample relative to the mosaic sputter target.[2] EDX/STRATAGEM could not be applied because of the multilayer substrate. The experiment was performed at room temperature and scheduled as follows:

1. HTS-AES
2. **Hydrogen exposure:** 1000 ppm H_2 in syn. air for 3 h
3. HTS-AES
4. **Poisoning:** 100 ppm H_2S in syn. air for 0.5 h
5. HTS-AES

In this study the alloy library was exposed to 1000 ppm H_2 in synthetic air and the exposition time was shorter compared the model alloy library. The poisoning procedure was also performed with a lower concentration of H_2S in synthetic air and shorter exposure time of 0.5 h. The gas treatments have been changed to match the conditions of hydrogen detection experiments [17–19]. The alloy library was screened with a pattern of 5 x 5 spots. The sample is screened then in x- and y- direction with a distance of 0.6 cm to another. In the end the alloy library is screened over an area of 2.4 x 2.4 cm^2 with 25 measured alloy compositions, which takes about four hours in total.

The results of the experiment are shown in Figure 8.8 as surface composition maps. The alloy library has a very smooth Pd gradient, with most of the alloy composition $X_{Pd} > 90 at.\%$. The surface composition maps of the alloy library as-received are shown in Figure 8.8 (a-c). In the as-received state the Pd range is X_{Pd} = 87 at.% - 97 at.%, the Ni range is X_{Ni} = 1 at.% - 11 at.% and the Co range is X_{Co} = 1 at.% - 6 at.%. As second step the sample was exposed to 1000 ppm hydrogen in dry synthetic air for 3 h and screened by AES afterwards (step 3). It has to be taken into account that synthetic air contains oxygen. Changes in the surface composition are described quantitatively by the surface composition maps in Figure 8.8 (d-f). The Pd concentrations are increasing and the concentrations of Ni and Co are decreasing. As fourth step in this experiment the alloy library was poisoned by 100 ppm H_2S in dry synthetic air for 0.5 h. The HTS-AES results

[2] see Chapter 2, Figure 2.1

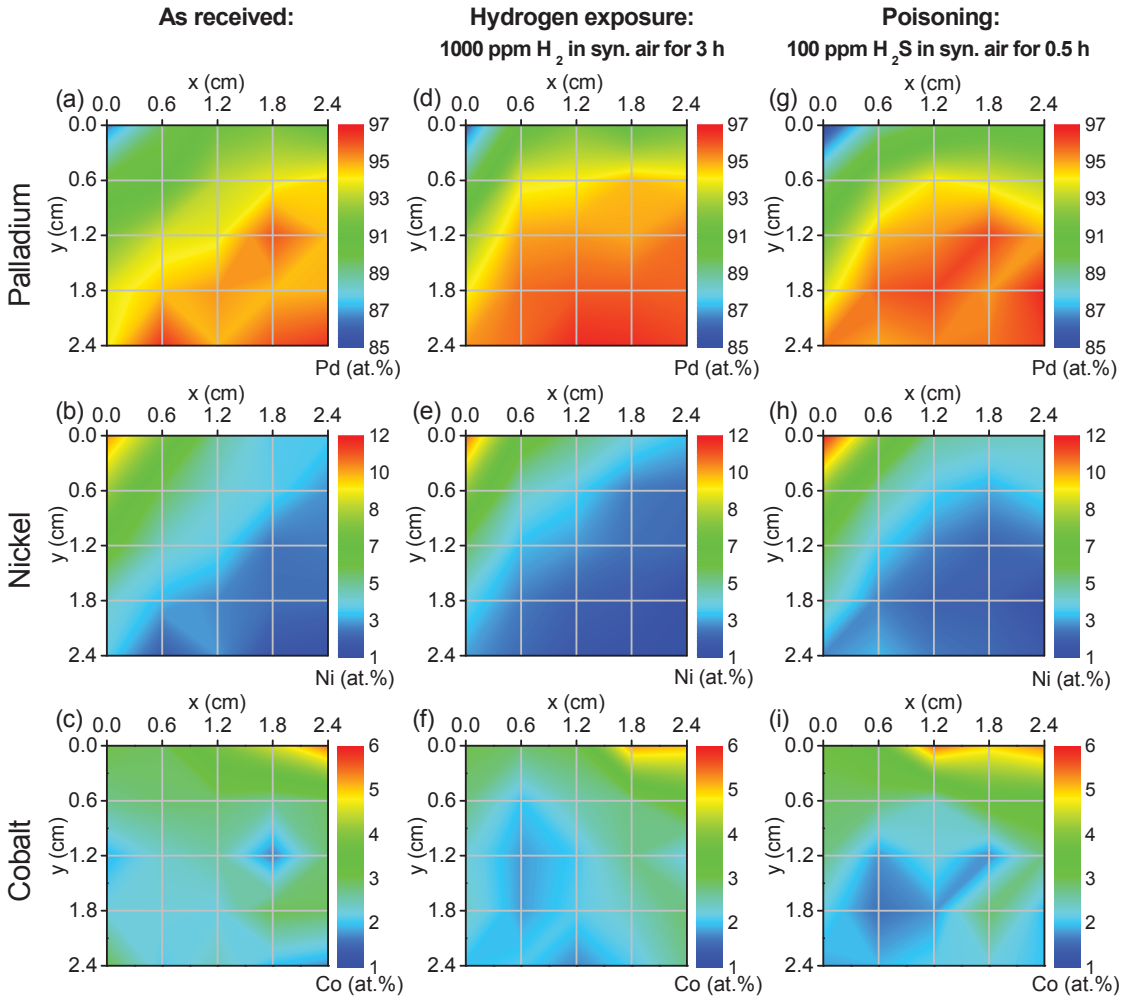

Figure 8.8: The surface composition maps of Pd, Ni and Co measured by HTS-AES with a pattern of 5 x 5 spots (grid) on an alloy library for hydrogen sensing purposes: as-received (a-c), after H_2 (d-f) and after H_2S (g-i).

in Figure 8.8 (g-i) show a decrease of Pd and increase of Ni and Co compared to the surface composition after the hydrogen treatment. The composition maps indicate an enrichment of Pd on the surface induced by the hydrogen treatment and a depletion of Pd on the surface after the hydrogen sulfide treatment. The co-segregation of Ni and Co is inverse to Pd. At Ni concentrations of $X_{Ni} > 10\ at.\%$ Ni increases after each gas treatment and the Pd concentration drops. The maximum of the Co concentrations is $X_{Co} \approx 5\ at.\%$ in the as-received state. At Co concentrations of $X_{Co} > 4\ at.\%$ the Pd concentrations are dropping after the gas treatments, while the Co concentrations increase. However, the Co concentrations in the alloy library are close to the detection limit and the signal to noise ratio of the measured Co peak is very poor.

8.2.1 The presence of oxygen on the surface

In addition to the development of the concentrations of Pd, Ni and Co in the ternary alloy system it has also been looked at the concentrations of oxygen. The highest oxygen concentration found on the surface in the as-received state is $X_O \approx 14$ *at.*%, which corresponds to the alloy composition of $\mathbf{Pd_{75}Ni_9Co_3O_{14}}$ and to the maximum of the Ni concentrations. In Figure 8.9 (a-c) the concentrations of Pd, Ni and Co are plotted against the O concentrations. Hereby the changes of the metal concentrations and oxygen concentrations can be followed.

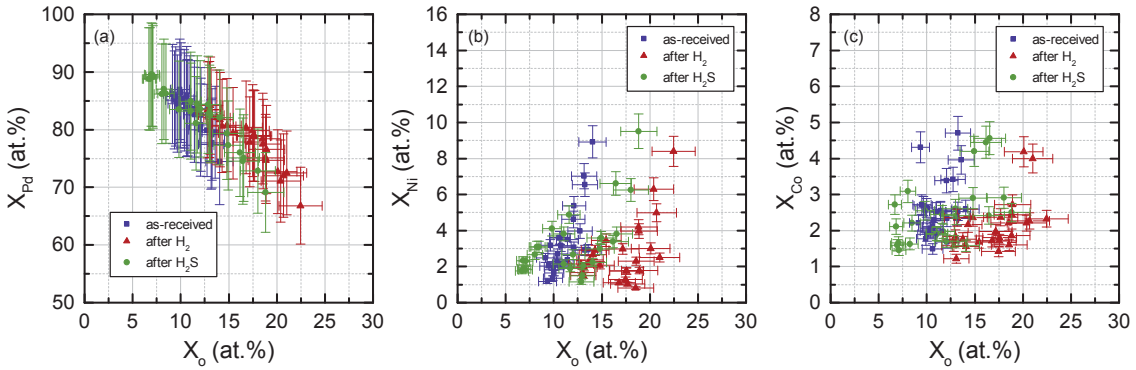

Figure 8.9: AES based surface concentration profiles ($u_c = \pm 10$ rel.%) of Pd, Ni and Co in relation to the oxygen concentration as-received, after hydrogen (H_2) and after sulfur poisoning (H_2S).

Figure 8.9 (a) shows the behavior of the Pd concentrations compared to the O concentrations on the surface. The oxygen concentrations increase from $X_O \approx 9$ *at.*% to $X_O \approx 14$ *at.*%. After the hydrogen treatment (1000 ppm H_2 in synthetic air) the oxygen concentrations reach a new maximum of $X_O \approx 23$ *at.*% at $\mathbf{Pd_{67}Ni_8Co_2O_{23}}$. After poisoning the oxygen concentrations reach a minimum of $X_O \approx 7$ *at.*% at $\mathbf{Pd_{89}Ni_2Co_3O_7}$, which is lower than the minimum O concentration of $X_O \approx 9$ *at.*% in the as-received state. Figure 8.9 (b) shows that the O concentrations are maximum where the Ni concentration is $X_{Ni} \approx 9$ *at.*% in the as-received state. The Ni concentrations in the alloy system increase from $X_{Ni} \approx 2$ *at.*% to $X_{Ni} \approx 9$ *at.*% which goes with an increase of the oxygen from $X_O \approx 10$ *at.*% to $X_O \approx 14$ *at.*%. After hydrogen exposure the Ni concentrations drop slightly, while the O concentrations increase. After poisoning the concentrations of Ni are increased again, while the O concentrations drop. The behavior of the Co concentrations in Figure 8.9 (c) is similar to the behavior of Ni. The changes of the oxygen treatments are strong compared to the changes of the Co concentrations on the alloy library surface.

8.2.2 Sulfur poisoning by H_2S

After exposing the alloy library to 1000 ppm hydrogen in dry synthetic air for 3 h and AES analysis the sample was exposed to 100 ppm H_2S in dry synthetic air for 0.5 h (poisoning) and analyzed again. In Figure 8.10 the differentiated Auger electron spectra (S, Pd, O, Co, Ni) of a single measurement position on the alloy library are shown before and after poisoning.

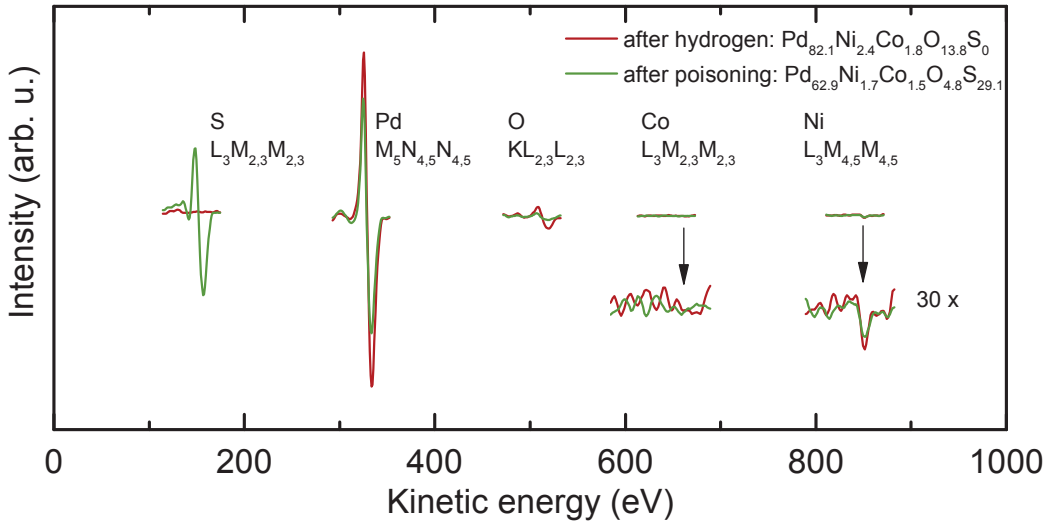

Figure 8.10: Differentiated Auger electron spectra of the regions of interest (S, Pd, O, Co, Ni) after the hydrogen treatment and after sulfur poisoning.

The spectra here represent the measurement position in the center of the alloy library acquired during high-throughput screening procedure. The estimated alloy composition is about $\mathbf{Pd_{95}Ni_3Co_2}$. In the spectra the intensity of palladium, nickel and oxygen are decreasing and the sulfur $K_3L_{2,3}L_{2,3}$ Auger transition appears at about 157 eV. The concentration of oxygen decreases by about $\approx$ 10 at.% and the concentration of sulfur is about $\approx$ 29 at.% with respect to Pd, Ni and Co. Sulfur is present everywhere on the surface.

Figure 8.11 summarizes the surface concentrations of Pd, Ni, Co, O vs. the development of the S concentrations. In Figure 8.11 (a) the sulfur concentration increases with the Pd concentration in the alloy composition. The minimum sulfur concentration is $X_S \approx 16$ at.% and the maximum is $X_S \approx 29$ at.%. which corresponds to $\mathbf{Pd_{58}Ni_8Co_2O_{16}S_{16}}$ and $\mathbf{Pd_{63}Ni_2Co_1O_5S_{29}}$, respectively. While in Figure 8.11 (b) the Ni concentrations decrease the S concentrations are increasing. That is similar to the adsorption behavior of S with the decrease of the Co concentrations in Figure 8.11 (c). The strongest dependency of the sulfur is related to O, which is shown in Figure 8.11 (d). The adsorption of sulfur due to H_2S poisoning is inverse

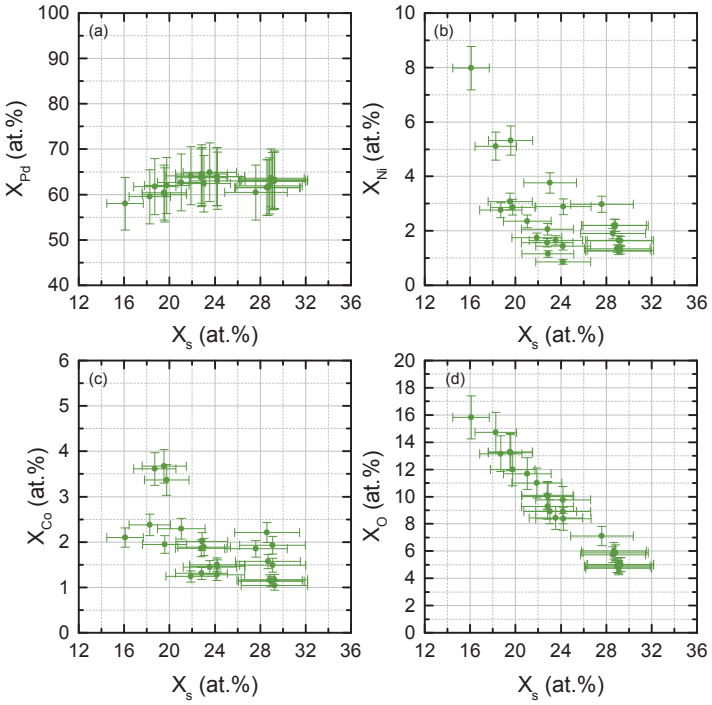

Figure 8.11: AES based surface concentration profiles ($u_c = \pm$ 10 rel.%) of Pd, Ni, Co and O in relation to the S concentration after sulfur poisoning with 100 ppm H_2S in syn. air for 0.5 h.

to the presence of oxygen on the surface. The sulfur concentrations are low at high O concentrations and vice versa. The decrease is linear from $X_O \approx 16$ at.% to $X_O \approx 5$ at.%.

8.2.3 Assumed consequences for a Pd-Ni-Co alloy hydrogen sensor

It was shown, that surface segregation is induced due to the contact of the alloy library to H_2 and H_2S, which changes the surface composition. Furthermore is was found that the surface oxidation by O_2 or H_2O (g) has a strong influence on the surface segregation of Ni and Co. In addition it is suspected that adsorbed carbon species, eg. CO, CO_2, cause surface segregation or poisoning. In summary all species from the gas phase of the environment cover the surface, block reactions sites for hydrogen, oxidize alloy components and change the surface composition. Surface contamination and oxidation are problematic for the long term performance, but cannot be avoided when the hydrogen sensor is used in ambient air.

By choosing the right alloy partner for Pd the surface segregation effects could lower the poisoning of Pd. Ni and Co showed similar segregation behavior, which caused the depletion of Pd on the surface. It is assumed that the co-segregation of Ni and Co to the surface reduces the oxidation and poisoning of Pd. The Ni and Co content influences the adsorption of sulfur, which is a positive effect on the alloy resistance against poisoning and could lead to a higher stability of the sensor response and an increase of the sensor life time.

On the other hand the surface concentration of Pd in the alloy is important for the hydrogen detection and probably the limiting factor for a fast sensor response. In the work of S. Linke it was pointed out that the Pd content in the alloy should be $X_{Pd} > 90$ at.% [19]. An increasing Ni concentration in the Pd-Ni-Co alloy library results in an exponential decay of the hydrogen sensitivity and different Co concentrations did not show an influence. After poisoning the sensor response was less affected in the concentration range of $X_{Ni} < 10$ at.%.

8.2.4 Conclusion

It was shown that in this ternary alloy system the surface segregation phenomena are related to the exposition into reactive gas atmospheres. The surface segregation is influenced by oxygen from ambient air and H_2 and H_2S in synthetic air. Higher concentrations of Ni and Co lead to a higher concentration of oxygen due to the oxidation of the elements. There the sulfur adsorption is hindered. From the findings it is proposed that the surface segregation of Ni and Co to the surface prevents Pd from oxidation and from poisoning if sulfur is present. Ni and Co are functioning as sacrificed metals.

8.3 Discussion of surface segregation in Pd-Ni-Co alloys

The difference between surface and bulk composition in alloys is called surface segregation. Surface segregation phenomena were often studied as a function of temperature on single crystalline binary alloys under UHV conditions. Here, surface segregation was studied on a polycrystalline ternary Pd-Ni-Co alloy system over a wide composition range, which was exposed to ambient air and to reactive gas atmospheres at room temperature and ambient pressure. In this section the observed surface segregation phenomena in the Pd-Ni-Co alloy system are discussed.

8.3.1 Experimental vs. theoretical surface segregation

In pure binary alloy systems of Pd-Ni and Pd-Co the segregation of Pd to the surface is predicted by density-functional theory (DFT) calculations of the surface segregation energies [94–96]. Ruban *et al.* pointed out that one should be careful when comparing theoretical results with experimental data. The surface composition of a transition metal alloy is very sensitive to external conditions of an experiment, due to the large difference in the reactivity of transition metals with gases such as O_2, H_2S, H_2, CO [94]. In ternary or multicomponent alloys the situation is more complex, because two or more species can segregate [97].

Thermodynamic predictions by semi-empirical theories, e.g. the regular solution theory, say that the component of the binary alloy with the lower heat of sublimation (or heat of vaporization) will segregate to the surface [98–100]. The heat of sublimation (equivalent to the heat of atomization) of Pd is 377 kJ/mol[3], of Ni is 431 kJ/mol[4] and of Co is 426 kJ/mol[5]. The value for Pd is much lower than those for Ni and Co. It is expected that the considerable difference in the heat of sublimation of the alloy constituents is the driving force for Pd surface segregation in a pure alloy system under vacuum conditions.

Experimental and theoretical surface segregation studies were carried out on binary Pd-Ni and Pd-Co alloys. Stoddart *et al.* explored the Pd-Ni alloy system under vacuum conditions over the composition range of X_{Ni} =5 - 80 at.% and detected the enrichment of Pd in the first atomic layer. In contrast air exposed Pd-Ni alloys showed an surface enrichment of Ni due to the formation of NiO on the surface [101]. Helfensteyn *et al.* found by Monte Carlo (MC) simulations a pronounced Pd segregation in Pd-Ni alloys for all compositions from 0 to 50 at.% and different crystal

[3]http://www.webelements.com/palladium/thermochemistry.html (2014)
[4]http://www.webelements.com/nickel/thermochemistry.html (2014)
[5]http://www.webelements.com/cobalt/thermochemistry.html (2014)

structures in the temperature range between 600 and 1000 K [102]. Krawczyk *et al.* investigated the surface composition under vacuum conditions of different polycrystalline Co-Pd alloys and found that Pd segregates to the surface above 300°C in $Pd_{70}Co_{30}$ and $Pd_{50}Co_{50}$ alloys [103]. Numerical calculations by Batirev *et al.* resulted also in the surface segregation of Pd to the surface in both binary alloy systems of Pd-Co and Pd-Ni [104].

8.3.2 Adsorbate-induced surface segregation

In his lecture about gas-solid interactions Green said: "The chemical binding of a gas molecule to a solid is obviously very complicated, impossible to generalize and full of surprises."[105] The adsorption, dissociation and chemical binding (chemisorption) of a molecule from the gas phase can have a strong influence on the surface composition of alloys. The difference in the reactivity of transition metals towards gases is large and the surface composition of a transition metal alloy is very sensitive to the external conditions. Thus, surface segregation can be induced by gas-solid interactions.

The study of the model Pd-Ni-Co alloy library revealed that the Pd surface composition is significantly different from the bulk composition, especially in the composition range of $X_{Pd} < 50$ at.%. The mean concentration gap between surface and bulk composition of Pd is about 11 at.% in the as-received state, where the surface of the alloy library is Pd depleted. In the composition range $X_{Pd} > 50$ at.% the surface and bulk composition are similar (cf. Figure 8.2). As the driving force for the surface segregation, here, the presence of oxygen from the ambient is proposed, which results in the co-segregation of Ni and Co due the formation of metal-oxygen bonds on the surface [101, 106]. The surface segregation in the alloy has direct consequences for the gas adsorption behavior, e.g. hydrogen sensitivity and adsorption of sulfur, and can be considered as an aging process of the alloy system. In the binary Ni-Co alloy system the preferential oxidation and segregation of Co takes place [107, 108].

The results of the surface segregation in the Pd-Ni-Co alloy system due to hydrogen exposure are ambiguous. The model alloy library with a surface composition of Pd between 15 at.% and 80 at.% was exposed to pure hydrogen and the Pd surface concentration decreased. In the hydrogen sensor-like library, which was exposed to 1000 ppm hydrogen in synthetic dry air and the Pd content of the alloy was between 87 at.% and 97 at.%, the concentration of Pd increased slightly. In both cases the alloy surface has already reacted with other gas molecules from ambient air. Hence

the adsorption of hydrogen on the pure alloy system cannot be considered anymore. The influence of hydrogen adsorption on the surface segregation of binary Pd-Ni or Pd-Co alloy systems have not been reported by now, but it was studied e.g. on the Pd-Ag alloy system. Løvvik and Opalka calculated that in the Pd-Ag alloy system, where Ag segregates to the surface under UHV conditions, the segregation is reversed due to hydrogen binding more strongly to Pd than to Ag [109]. This is in agreement with the findings of Padama *et al.* [110]. Svenum *et al.* calculated that the segregation is reversed due to the adsorption of hydrogen, carbon monoxide and oxygen in the Pd-Ag system [111].

The influence of poisoning to the alloy composition resulted in a depletion of Pd on the surface in all experiments presented in this thesis. The driving force of the surface segregation due to poisoning by H_2S is the formation of metal-sulfur bonds. It was shown (cf. Figure 8.7 and 8.11), that the adsorption of sulfur strongly depends on the alloy composition and amount of oxygen on the surface. The amount of oxygen depends on the concentration of Ni and Co in the alloy composition.

Miller *et al.* investigated the effect of adsorbed sulfur on a single polycrystalline $Pd_{70}Cu_{30}$ alloy and on a wide range of bulk alloy compositions [16, 112]. Adsorbed sulfur caused a reversal of the Cu enrichment of the topmost surface, resulting in a top layer that contained only Pd and S atoms.

In general, the expected response to adsorbates is that the more reactive alloy component (i.e. the one forming the strongest chemical bond with the adsorbates) segregates to the surface [114]. Nørskov *et al.* calculated the binding energies of adsorbed oxygen and hydroxyl groups based on the reaction from water (gas) on the transition metal surface (solid), from which can be seen that Co has the strongest

	$\Delta_f H^\circ$ (kJ/mol)		$\Delta_f H^\circ$ (kJ/mol)		$\Delta_f H^\circ$ (kJ/mol)
PdO	-85	NiO	-241	CoO	-238
		Ni_2O_3	-490		
				Co_3O_4	-891
				$Co(OH)_2$	-540
PdS	-75	NiS	-82	CoS	-83
				Co_2S_3	-147
		$NiSO_4$	-873	$CoSO_4$	-888

Table 8.3: Values of the standard molar enthalpy (heat) of formation, $\Delta_f H^\circ$, for several Pd-, Ni- and Co-oxygen and -sulfur compounds [113].

binding energy to O and OH with respect to Ni and Pd, that has the lowest [115]. As a first approximation of the reactivity of alloy constituents the standard molar enthalpies of several Pd-, Ni- and Co-oxygen and -sulfur compounds are given in Table 8.3.

The co-segregation of two alloy constituents is observed in this ternary transition metal alloy system. It is suspected that the adsorption of carbonaceous species, such as CO and C_xH_y, has an additional influence on the surface segregation. For a more detailed thermodynamical description of adsorbate-induced surface segregation processes more powerful computational methods have to be applied, such as Monte Carlo simulations or extended DFT calculations.

8.3.3 Conclusion

The surface co-segregation of Ni and Co is observed in the ternary Pd-Ni-Co alloy system due to oxygen adsorption from the ambient leading to the oxidation of Ni and Co. In a clean alloy system under vacuum conditions an enrichment of Pd on the surface would be expected from the theoretical predictions in binary systems. Here, the surface segregation is reversed due to chemisorption of molecules from the gas phase (ambient air, pure H_2 and H_2 in dry synthetic air, H_2S in dry synthetic air). The chemisorption of sulfur (poisoning) on the alloy surface, provided by H_2S, is irreversible and emphasizes the co-segregation of Ni and Co.

9 Depth profiling of a Pd-Ni-Co thin film alloy before and after poisoning

In this chapter the results of the non-destructive depth profiling study are presented. The goal was the acquisition of the composition profile of a Pd-Ni-Co alloy before and after poisoning. Out of a Pd-Ni-Co thin film alloy library deposited on Si with the triple source sputter setup a single alloy composition ("a book") was selected and investigated by AES, XPS, HAXPES and EDX/STRATAGEM. The HAXPES experiments have been performed using the HIKE end station at the KMC-1 beamline, Helmholtz-Zentrum Berlin (BESSY II, Germany), and were completed by the complementary thin film analysis methods AES, XPS and EDX at the BAM 6.8 laboratory. In the first part of this chapter the alloy composition is presented as a function of probing depth. In the second part the surface and bulk chemistry of the Pd-Ni-Co alloy system is presented and discussed based on the XPS and HAXPES data.

9.1 Compositional depth profiling by AES, XPS, HAXPES and EDX

The performance of HAXPES as a tool for non-destructive depth profiling has been shown in several studies in the field of materials chemistry [78, 116, 117]. Here, HAXPES data were evaluated quantitatively and combined with results from AES, XPS and EDX to reveal the composition profile of a catalytic active ternary alloy system on the nanometer scale. The air exposed Pd-Ni-Co alloy system was studied before and after hydrogen sulfide poisoning. The exposure time of the sample to ambient air was kept as short as possible, but oxidation of the as-received state could not be avoided completely. During transport between the laboratories the sample was carried under inert gas atmosphere. The experiment was conducted as follows:

1. AES, XPS, EDX of the air exposed alloy
2. HAXPES of the air exposed alloy
3. **Poisoning:** 100 ppm H_2S in syn. air for 1 h at RT
4. HAXPES
5. AES, XPS, EDX

Each method in this study provides a different probing depth, which is illustrated in Figure 9.1. On the left hand side the probing depth of AES, XPS, HAXPES and EDX is illustrated and on the right hand side the corresponding spectra are shown for each method. AES is most surface sensitive, while EDX is most bulk sensitive, even penetrating the substrate. The probing depth of electron excited AES was estimated by calculating the mean escape depth (MED) according to the inelastic mean free path (IMFP) depending on the electron kinetic energy of Pd $M_5N_{4,5}N_{4,5}$ Auger transition, as described in Section 3.3. Auger spectra were acquired with a 5 keV electron beam and 20 nA beam current. The AES data were quantified using elemental RSFs (ERSFs) given by the manufacturer, which was discussed in Section 6.2. The variation of the probing depth in case of XPS (monochromatic

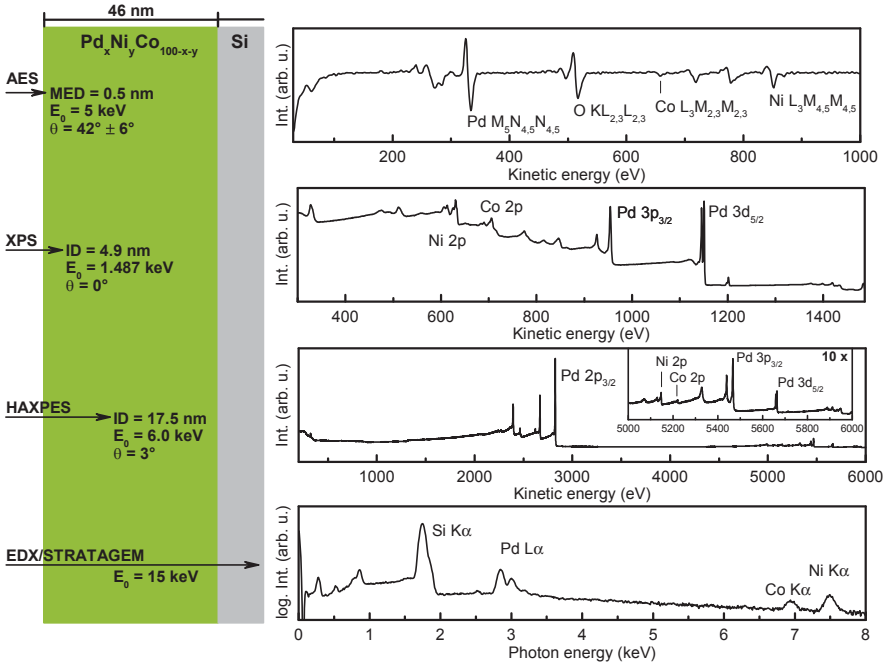

Figure 9.1: On the left the schematic drawing of the sample illustrates the probing depth of AES, XPS, HAXPES and EDX (see Table 9.2 for details). On the right the corresponding spectra for each method are shown before the poisoning of the air exposed alloy.

Method	E_0 (keV)	E_{kin}(Pd) (eV)	$\lambda(E_{kin})$ (nm)	Probing depth (nm)
AES	5.0	334	0.7	0.5
XPS $\theta = 60°$	1.487	1152	1.6	2.5
XPS $\theta = 0°$	1.487	1152	1.6	4.9
HAXPES	6.0	5665	5.8	17.5
EDX*	15, 20, 25		Film thickness:	46 nm

Table 9.2: The probing depth of AES (MED: $\lambda_{MED} = \lambda_{Pd(M_5N_{4,5}N_{4,5})}\cos(\theta)$), XPS and HAXPES (ID: $z_{95\%} = 3\lambda_{Pd(3d_{5/2})}\cos(\theta)$) based on the alloy bulk composition $\mathbf{Pd_{65}Ni_{25}Co_{10}}$ determined together with the film thickness of the Pd-Ni-Co alloy layer on Si from EDX data processed with *STRATAGEM.

Al Kα, 1487 eV) was achieved by variation of the angle of emission between 0° and 60°. In case of HAXPES the bulk sensitivity was realized by using a photon energy of 6000 eV. Details about the information depth, data acquisition and quantification of XPS and HAXPES data were given in Chapter 5. The probing depth of XPS and HAXPES was calculated according to IMFPs depending on the electron kinetic energy of Pd $3d_{5/2}$ core level. For the IMFP calculation (AES and PES) the bulk composition of the alloy layer, $\mathbf{Pd_{65}Ni_{25}Co_{10}}$, was used based on the EDX/STRATAGEM result. From the bulk composition an alloy layer density of about 10.9 g/cm^3 was calculated resulting in film thickness of about 46 nm. The EDX/STRATAGEM data reduction procedure was presented in Chapter 7. Here, k-values were determined at beam voltages of 15, 20 and 30 keV [63]. The net intensities of all spectra were normalized to live time (600 s) and beam current. The values of the probing depth are summarized in Table 9.2.

In Figure 9.2 the compositional depth profiles of Pd (a), Ni (b) and Co (c) based on AES, XPS, HAXPES and EDX/STRATAGEM data are shown as a function of probing depth before (closed squares) and after poisoning (open squares). The surface composition found by AES of the as received state is $\mathbf{Pd_{49}Ni_{35}Co_{16}}$. Compared to the bulk composition of $\mathbf{Pd_{65}Ni_{25}Co_{10}}$ Ni and Co are enriched on the surface. In Figure 9.2 (a) the concentration profile of Pd reveals a depletion in the outermost surface (X_{Pd} = 49 at.%) and an enrichment directly beneath the surface (X_{Pd} = 63 at.%). At about 5 nm the concentration is similar to the bulk composition given by HAXPES and EDX. After poisoning a depletion of Pd in the outermost surface (AES) of about 9 at.% is observed. According to the decrease of Pd surface concentration the Pd content is increased directly below the surface

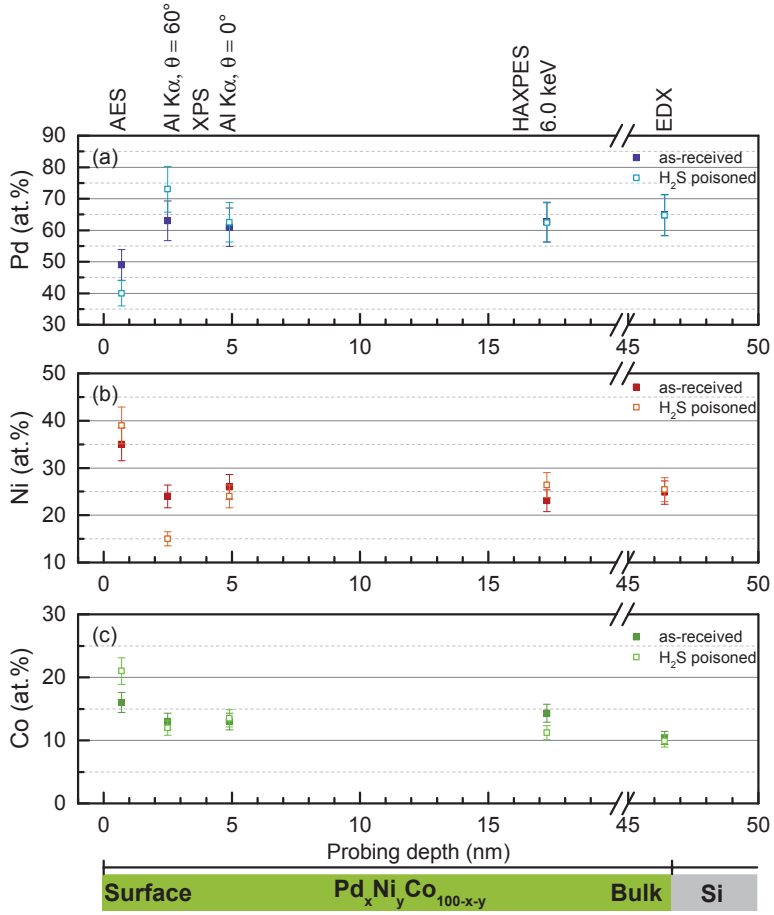

Figure 9.2: Non-destructive compositional depth profile based on AES, XPS, HAXPES and EDX quantitative data (at.%) of an air exposed Pd-Ni-Co thin film alloy on Si before and after poisoning by H_2S.

of about the same value. In Figure 9.2 (b) one can see that Ni is enriched on the surface (X_{Ni} = 35 at.%). The concentration profile shows a depletion of Ni beneath the surface, where Pd is enriched. The XPS data, taken at $\theta = 0°$, and the HAXPES data are in good agreement with the determined bulk concentration by EDX (X_{Ni} = 23 at.%). After poisoning the outermost surface shows an enrichment of Ni (X_{Ni} = 39 at.%), which is an increase of about 4 at.%. Therefore Ni is depleted in surface near region (X_{Ni} = 15 at.%). Beneath that the Ni concentration is unaffected after poisoning. In Figure 9.2 (c) the segregation profile of Co shows a slight enrichment of Co on the surface (X_{Co} = 16 at.%) compared to the bulk value (X_{Co} = 10 at.%). After poisoning, the enrichment of Co is observed on the surface (X_{Co} = 21 at.%), which is an increase about 5 at.%. The composition in the surface near region investigated by XPS and HAXPES did not change significantly. Overall the HAXPES data have shown nearly the same values after poisoning, from which a

good reproducibility of the experimental approach can be derived. The quantitative HAXPES approach, determining PERSFs experimentally, delivered alloy compositions in the range of the other methods. The bulk composition of $\mathbf{Pd_{65}Ni_{25}Co_{10}}$ derived by EDX/STRATAGEM remained unchanged. The results are in agreement with the observation of the surface and bulk high-throughput screening study presented in Section 8.1. In the literature the segregation of Ni and Co to the surface was reported in binary Pd-Ni and Pd-Co alloys due to the oxidation of Ni and Co after they were exposed to ambient air or oxygen [101, 106]. The surface segregation here is reversed compared to an alloy system kept under vacuum, where Pd would segregate to the surface. The co-segregation of Ni and Co is emphasized after exposition of the sample to the reactive atmosphere of hydrogen sulfide. This is in agreement with the high-throughput screening experiments presented in Chapter 8.

9.1.1 Conclusion

A composition profile of the alloy constituents was accomplished on the nanometer scale by combining AES, XPS, HAXPES and EDX experiments. In the as-received state of the Pd-Ni-Co alloy the surface was already enriched with Ni and Co with respect to the bulk composition due to oxidation from ambient air. The poisoning had consequences for the composition of the sample within the first ≈ 10 monolayers (2.5 nm) and induced significant surface segregation within the Pd-Ni-Co alloy. The co-segregation of Ni and Co to the surface after poisoning increased the depletion of Pd on the surface.

9.2 Chemical depth profiling by XPS and HAXPES

The surface and bulk chemistry of the Pd-Ni-Co alloy system in the as-received state and after poisoning was studied according to the acquired core level spectra of XPS and HAXPES. The information depth was varied by changing the angle of emission in case of XPS and by varying the photon excitation energy in case of HAXPES. The core levels of Pd 3d, Ni 2p and Co 2p are presented in detail in the following and discussed in terms of their chemical states. The alloy poisoning is discussed in terms of the S 2p and S 1s core level spectra. All information about the PES experiments and the data reduction were given in Chapter 5. A Shirley-type background was subtracted from the core level spectra and the intensities were normalized to the pure metallic peak to follow relative changes within the core level. The binding energy scale was calibrated by shifting the C 1s core level to E_{bin} = 285 eV. The information depth for XPS and HAXPES is estimated using to the Pd $3d_{5/2}$ core level photoemission.

9.2.1 Pd 3d, Ni 2p and Co 2p core level spectra of the Pd-Ni-Co alloy before and after poisoning

Palladium is the main component of the studied Pd-Ni-Co alloy. The Pd 3d spectra acquired by XPS and HAXPES before and after poisoning are shown in Figure 9.3. XPS was performed at two different angles of emission, $\theta = 60°$ and $\theta = 0°$, which corresponds to an information depth of 2.5 nm and 4.9 nm respectively. The information depth of HAXPES is in the range from 8.0 nm at 2.5 keV to 17.5 nm at 6.0 keV. In the XPS data of the alloy in the air exposed as-received state in Figure 9.3 (a) the Pd $3d_{5/2}$ signal is found at E_{bin} = 335.7 eV. The value is similar to that published for Pd-Ni alloys by Hillebrecht *et al.* [118]. The Pd $3d_{3/2}$ signal is found at 341.0 eV. After poisoning the Pd $3d_{5/2}$ signal is shifted about 0.3 eV to lower binding energies. On the higher binding energy side of the Pd $3d_{5/2}$ peak the formation of Pd-S bonds is suspected [119]. The corresponding HAXPES data of the Pd 3d core level are shown in Figure 9.3 (c, d). The observed peak broadening in the spectra has its origin in the loss of energy resolution of the Si (111) monochromator crystal from 0.3 eV to 1.4 eV at higher photon energies from 2.5 keV to 6.0 keV (cf. Figure 5.2). The peak position of the Pd $3d_{5/2}$ core level is at E_{bin} = 335.3 eV, also after poisoning. The peak shape of the Pd 3d core level from the Pd-Ni-Co alloy system is in agreement with the data found for metallic Pd in the literature [120, 121].

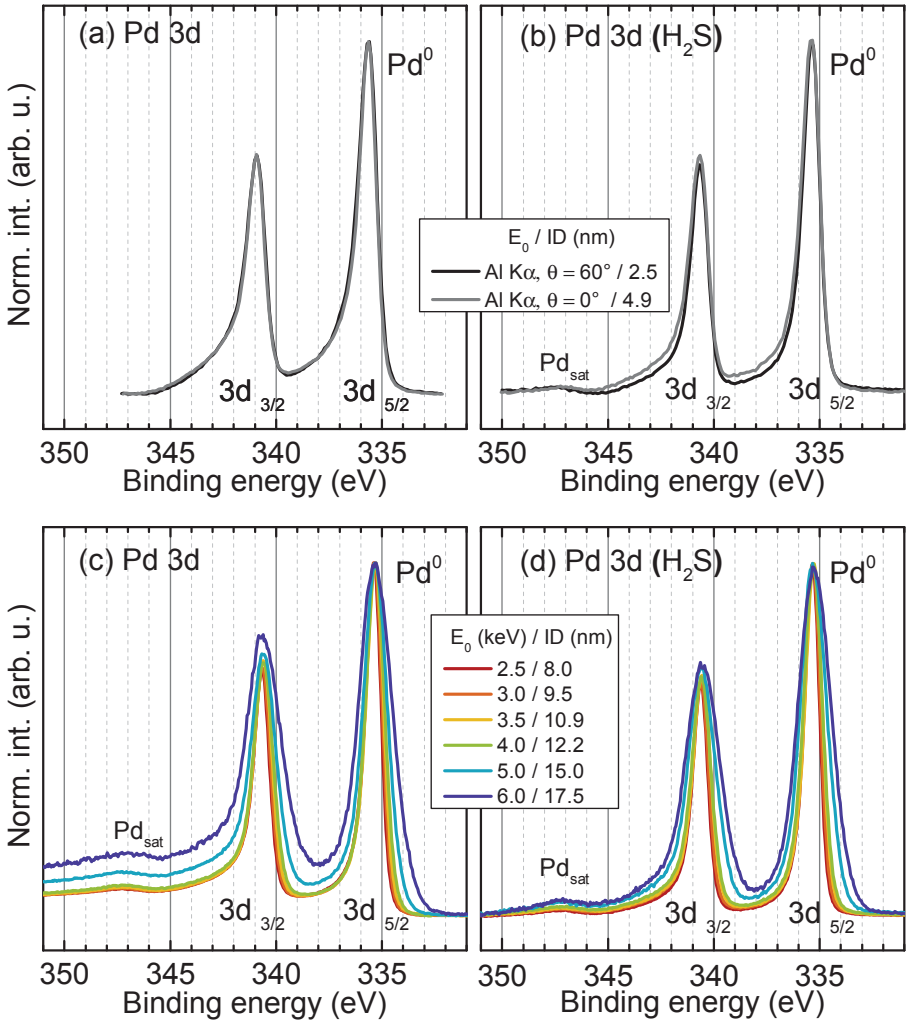

Figure 9.3: XPS Pd 3d core level before (a) and after poisoning (b) acquired at two different emission angles with monochromatic Al Kα radiation. HAXPES Pd 3d core level before (c) and after poisoning (d) acquired with six different excitation energies.

Figure 9.4 (a, b) shows the Ni 2p spectra of the Pd-Ni-Co alloy system measured with XPS. Metallic Ni^0 peak is identified at a binding energy of E_{bin} = 852.5 eV within the Ni $2p_{3/2}$ peak. Furthermore there are contributions of Ni^{2+} and Ni^{3+} to the higher binding energy side of the metallic peak. Ni in the Pd-Ni-Co alloy is oxidized on the surface and after poisoning the intensities of the Ni^{2+} and Ni^{3+} compounds are increased. In the hard X-ray photoemission spectra in Figure 9.4 (c), which are more bulk representative, the intensity of the Ni (0) state is higher than the oxidized Ni^{2+} and Ni^{3+} states. The intensities of the oxidized Ni states along the metallic peak to higher binding energies decrease with higher excitation energies. In contrast to the surface, these states are further decreased after poisoning, as shown

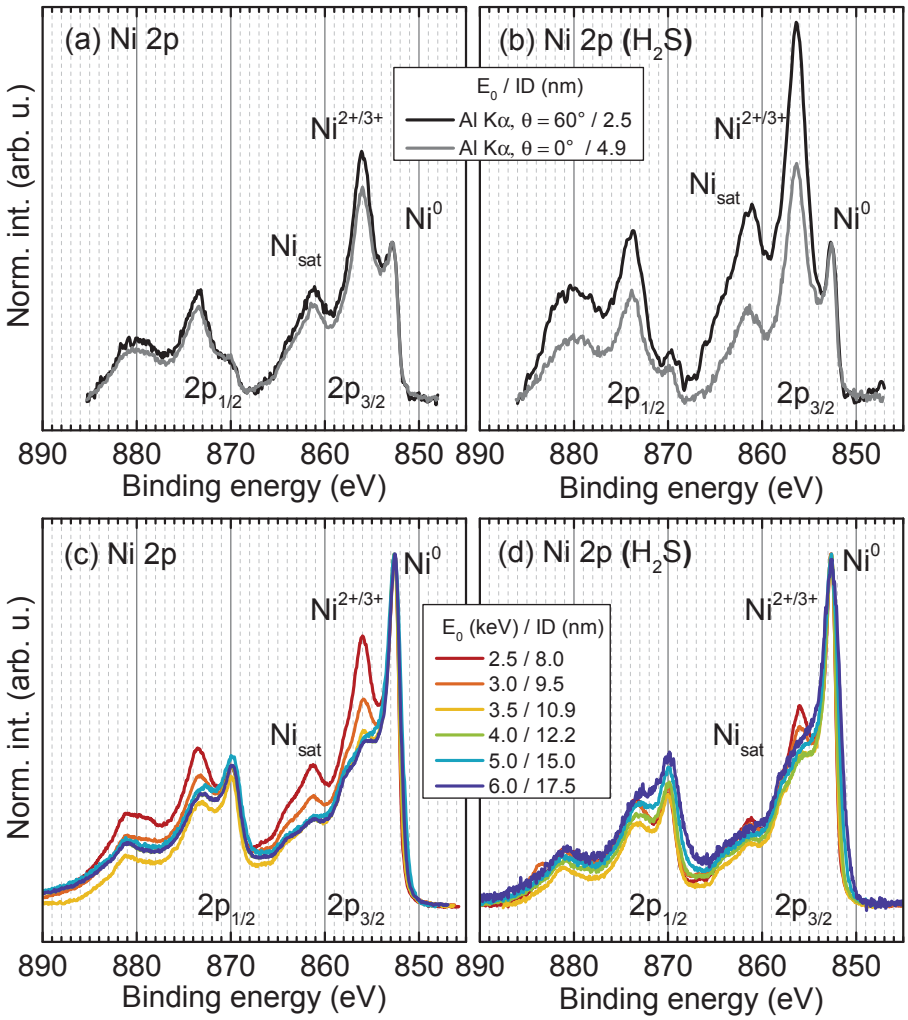

Figure 9.4: XPS Ni 2p core level before (a) and after poisoning (b) acquired at two different emission angles with monochromatic Al Kα radiation. HAXPES Ni 2p core level before (c) and after poisoning (d) acquired with six different excitation energies.

in Figure 9.4 (d). An increase at the surface, addressed by the XPS experiments, and a decrease in the surface near/bulk region, addressed by the HAXPES experiments, of the oxidized states of Ni due to the poisoning is revealed. Different Ni species related to the Ni 2p shape are proposed, such as of Ni (0), NiO (2+), $Ni(OH)_2$ (2+), NiO(OH) (3+), Ni_2O_3 (3+) due to contact to ambient air and to oxygen during poisoning in synthetic air. A mixed metal/oxide/hydroxide Ni phase in the first nanometers of the Pd-Ni-Co alloy system is found. Proposed surface chemical states of Ni, its oxides and hydroxides are inspired by detailed studies of Grosvenor *et al.*, Payne *et al.* and Biesinger *et al.* [122–126].

Figure 9.5 (a, b) shows the Co 2p core levels measured with XPS. The interpretation of the chemical states of Co is similar to that of Ni [127, 128]. According to the peak shape of the Co 2p core level chemical states of Co (0), CoO (2+), $Co(OH)_2$ (2+), CoO(OH) (3+) and Co_3O_4 (2+/3+) are proposed. The metallic Co peak is found at $E_{bin} = 778.1$ eV. Co is more oxidized than Ni in the Pd-Ni-Co alloy. In Figure 9.5 (b) the intensity of the oxidized states of Co is strongly increased. Figure 9.5 (c, d) show the hard X-ray photoemission spectra of the Co 2p core level. In Figure 9.5 (c) the oxidized states of Co have a higher intensity than the metallic state. In Figure 9.5 (d) the intensity changes are less significant compared to the Ni 2p spectra (cf. Figure 9.4). Law *et al.* reported the preferential oxidation of Co

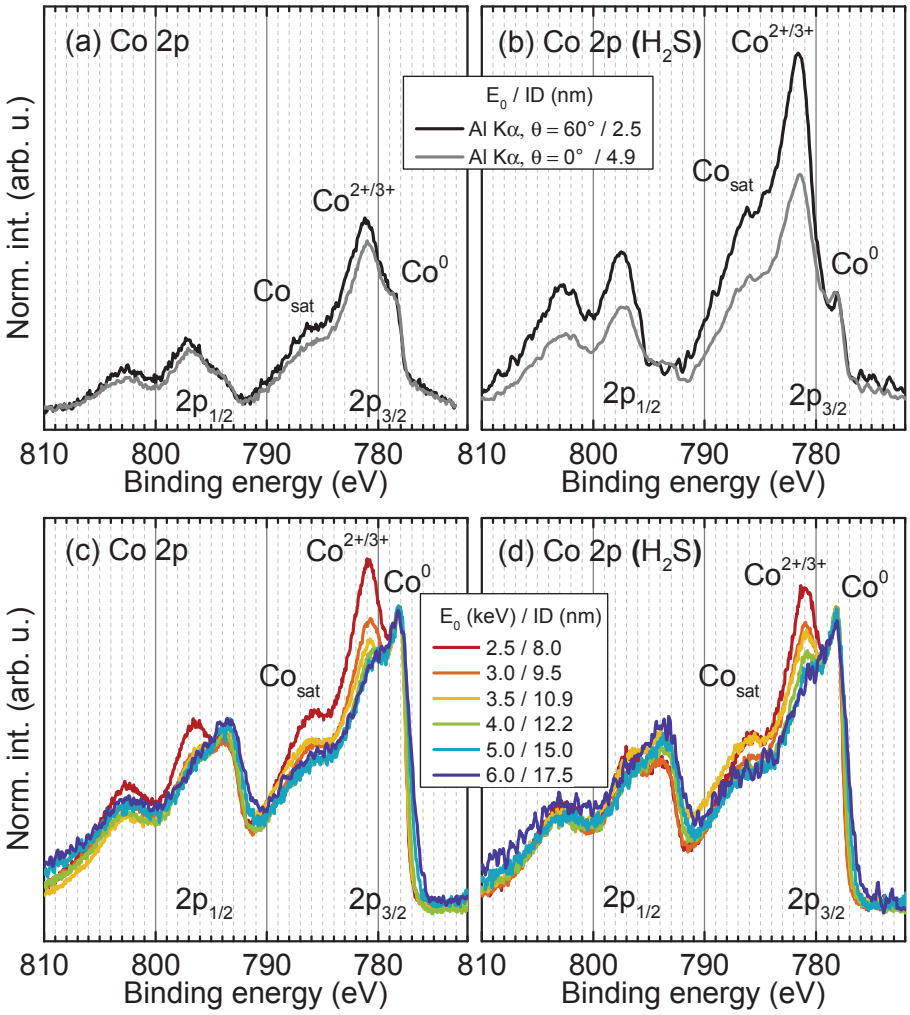

Figure 9.5: XPS Co 2p core level before (a) and after poisoning (b) acquired at two different emission angles with monochromatic Al Kα radiation. HAXPES Co 2p core level before (c) and after poisoning (d) acquired with six different excitation energies.

in the Ni-Co system, which can also be concluded here [108]. Furthermore a mixed oxide of Ni and Co is proposed for the Ni-Co alloy system. The same interpretation was suggested by M. C. Biesinger for the oxidized Pd-Ni-Co alloy system.[1]

9.2.2 Sulfur poisoning: S 2p and S 1s core level spectra

The Pd-Ni-Co alloy was poisoned by 500 ppm H_2S in synthetic air for of 1 h at room temperature and atmospheric pressure. A sulfur concentration on the surface of about 3 at.% on this particular alloy composition was determined by AES and XPS with respect to concentrations of Pd, Ni and Co. The S 2p (XPS) and S 1s (HAXPES) core level spectra are shown in Figure 9.6 (a, b).

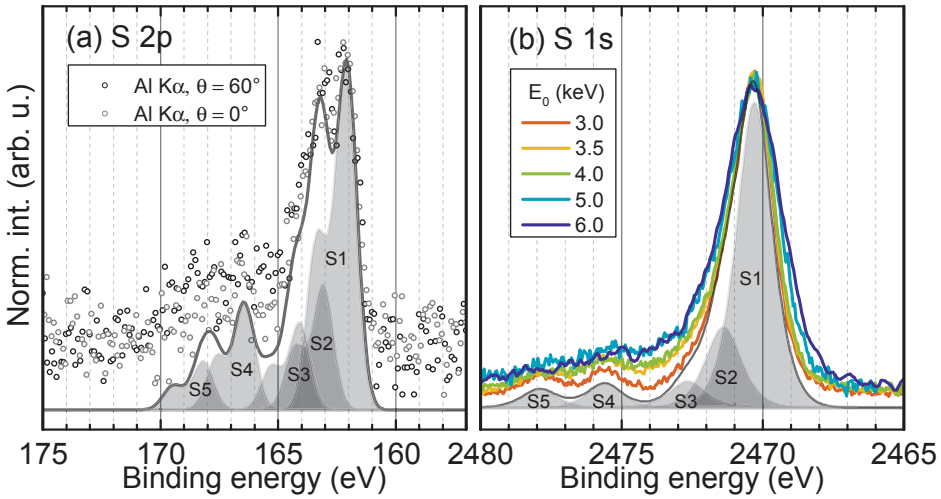

Figure 9.6: The sulfur core level spectra after H_2S exposure: (a) S 2p core level spectra acquired at two different emission angles with monochromatic Al Kα radiation. The S 2p core level taken at $\theta = 0°$ was fitted with 5 doublet peaks (FWHM = 1.0 eV). (b) S 1s core level acquired with five different excitation energies. The S 1s core level acquired at 3.0 keV was fitted with 5 singulet peaks (FWHM = 1.5 eV).

No signal was found for the S 2p core level in the hard X-ray regime because of the low sulfur concentration and the low photoionization cross section of the S 2p at higher photon energies. The S 1s singulett was fitted with five peaks (S1-S5), where the major component is the metal-sulfide state at E_{bin} = 2470.3 eV, which agrees well with the literature [129]. Related to the S 1s fit, the S 2p doublet was fitted also with five components (S1-S5). The main peak (S1) at E_{bin} = 162.0 eV and the second

[1]Personal communication (2013)

peak (S2) at E_{bin} = 163.0 eV are related to metal-sulfide states, e.g. PdS, NiS, CoS.[2] The other three components (S3-S5) are related to different chemical environments and oxidized states of sulfur. Here, different sulfur species are proposed on the surface, such as S^0 (S3, E_{bin} = 164.0 eV) SO_3^{2-} (S4, E_{bin} = 166.5 eV) and SO_4^{2-} (S5, E_{bin} = 168.3 eV) [6, 130]. The hydrogen sulfide gets decomposed by reacting with the transition metals of the alloy and with oxygen and hydroxide groups on the surface.

9.2.3 Conclusion

A mixed metal/oxide alloy system on the surface and in the surface near region was revealed in the as-received state of the Pd-Ni-Co alloy due to air exposure. In addition to H_2S more oxygen is served during the poisoning procedure, which results in a significant increase of the Ni and Co (2+) and (3+) states in the XPS data. In the HAXPES data these states are decreasing. In the S 2p and S 1s core levels the sulfide component was identified as the main contribution next to several other sulfur species related to the decomposition of H_2S.

[2]NIST X-ray Photoelectron Spectroscopy Database, http://srdata.nist.gov/xps/ (2015)

10 Summary and perspectives

In this thesis the composition and chemistry of the Pd-Ni-Co thin film alloy system was studied by using different surface and thin film analytical methods based on electron and X-ray spectroscopy. In focus was the synthesis and characterization of the Pd-Ni-Co thin film alloy system over a wide composition range and the investigation of compositional and chemical changes related to air, hydrogen and hydrogen sulfide exposure. Therefore a combinatorial approach was explored by preparing ternary thin film alloy libraries.

The composition range of the alloy libraries was extended step by step by varying the deposition parameters of two sputter setups and checking the compositions by AES. The quality of the thin film growth in terms of its physical morphology was ensured by SEM and TEM experiments. The single source sputter setup only provided a very limited composition range and delivered very Pd-rich alloys. The limitation of the composition range was overcome by commissioning a triple source sputter setup (Chapter 2). For the determination of the composition range of the deposited alloy libraries a high-throughput screening (HTS) strategy has been established for AES. In a rapid and efficient way alloy libraries with a maximum sample size of about 3×3 cm^2 can be screened. The possible ways of the matrix correction in AES for a ternary alloy system to improve the accuracy of quantification were discussed (Chapter 6). The size limitation of the alloy library for the EDX setup is the same as for AES. The capabilities of EDX combined with the STRATAGEM software determining simultaneously the bulk composition and the film thickness of the ternary Pd-Ni-Co alloy system on a substrate (Chapter 7) and the application for HTS (Chapter 8) were successfully demonstrated. The surface segregation in the Pd-Ni-Co alloy system was studied related to ambient air, the influence of hydrogen and hydrogen sulfide exposure (Chapter 8). Ni and Co are co-segregating on the surface driven by oxygen from ambient air, hydrogen and poisoning by sulfur. As a consequences of the surface segregation in the ternary alloy system undesirable chemical reactions of Pd with reactive gases are suppressed and the poisoning of Pd in the bulk of the alloy is prevented.

There is a trade-off between the combinatorial HTS and the conventional approach to study single alloy compositions. The conventional approach is more accurate and more methods can be applied to a single sample. This was done by studying the sulfur poisoning effects on a single alloy composition selected from an alloy library. AES, XPS, HAXPES and EDX were combined in one experiment to acquire a compositional depth profile from the outer most surface into the bulk before and after poisoning (Chapter 9). HAXPES experiments were performed at the HIKE end station at BESSY II. The experiment revealed the compositional depth profile on the nanometer scale. The reaction with hydrogen sulfide led to compositional changes within the first monolayers of the alloy sample, where a depletion of Pd was observed. A chemical depth profile from the air exposed and poisoned Pd-Ni-Co alloy system was obtained from soft and hard X-ray photoelectron spectra. A mixed metal/oxide alloy system on the surface and in the surface near region was revealed and after poisoning the sulfide state was found as the main component in the sulfur spectra.

For future studies on ternary thin film alloy systems the triple source sputter setup offers the possibility to deposit any other ternary transition metal alloy combinations with a desired composition range by changing a sputter target. The lessons learned from the HTS experiments with AES and EDX can be used now to study surface segregation phenomena in ternary alloy systems over a wide composition range. The capabilities of principal component analysis on HTS-AES data could be investigated to derive also chemical information about the alloy system, which would make HTS-AES more powerful. Other gases and their influence on the alloy compositions could be investigated as well, e.g. CO. The findings from surface and thin film analysis should be linked to hydrogen sensing experiments, to suggest a new alloy composition or a certain composition range, that has advances compared to a pure Pd based hydrogen sensor. The high-throughput screening sensor experiments help to understand the impact of alloying Pd with other transition metals on the hydrogen sensor performance.

In 2016 the Energy Materials in-situ laboratory (EMIL) at BESSY II will start operation. A dual beam line concept will provide soft and hard X-rays. Non-destructive compositional and chemical depth-profiling can be performed then from the outermost surface down to the bulk in one experiment without changing the experimental setup. The photon energy could be tuned in such a manner, that all photoelectrons have the same kinetic energy, which means that all arise from the same information depth. Segregation profiles of alloy systems could be investigated

more accurate. In further HAXPES studies the chemistry at the alloy/LaF_3 interface of the hydrogen sensor-like device could be addressed. In addition to soft and hard X-ray photoelectron spectroscopy, X-ray absorption and X-ray diffraction experiments will be available for studying the alloy system. In-situ gas exposure experiments can be performed directly at the beam line using the versatile sample preparation system. Nowadays so-called high pressure or near ambient XPS systems are available, which allow to study the gas-solid interactions in real time.

From the materials chemistry point of view one could start further thinking about other high-throughput screening experiments related to other applications, e.g. the investigation of compositional and chemical changes of an alloy system related to the working conditions of a hydrogen separation membrane. The concepts and results presented in this thesis are heading in a new direction for designing future Pd-alloys beyond their application as hydrogen sensor.

Publications

This project was a collaboration between the BAM 6.8 Surface Analysis and Interfacial Chemistry group of Dr. Unger and the Chemical Sensor group of PD Dr. Moritz from the HUB. The first part of the project (August 2010 - January 2012) was funded by the DFG under contracts UN 80/10-2 and MO 599/30-2 and continued with funding from the BAM PhD-program (February 2012 - July 2013).

Journals - peer reviewed

J. Kühn, V.-D. Hodoroaba, S. Linke, W. Moritz and W. E. S. Unger. Characterization of Pd-Ni-Co Alloy Thin Films by ED-EPMA with Application of the STRATAGEM Software. *Surface and Interface Analysis*, **44**, 1456 (2012).

Journals - in preparation

J. Kühn, A. Lippitz, M. Gorgoi, K. Nörthemann, W. Moritz and W. E. S. Unger. Sulfur poisoning of an air exposed Pd-Ni-Co alloy studied by XPS and HAXPES. *In preparation.*

J. Kühn, K. Nörthemann, W. Moritz and W. E. S. Unger. The influence of sulfur poisoning on the compositional depth profile of an air exposed Pd-Ni-Co thin film alloy. *In preparation.*

J. Kühn, K. Nörthemann, W. Moritz and W. E. S. Unger. The impact of H_2 exposure and H_2S poisoning on the surface segregation in an air exposed Pd-Ni-Co thin film alloy library. *In preparation.*

Journals - peer reviewed - other contributions

S. Malmgren, K. Ciosek, R. Lindblad, S. Plogmaker, J. Kühn, H. Rensmo, K. Edström, M. Hahlin. Consequences of air exposure on the lithiated graphite SEI. *Electrochimica Acta*, **105**, 83 (2013).

E. Darlatt, C. Traulsen, J. Poppenberg, S. Richter, J. Kühn, C. A. Schalley, W. E. S. Unger. Evidence of click and coordination reactions on a self-assembled monolayer by synchrotron radiation based XPS and NEXAFS. *Journal of Electron Spectroscopy and Related Phenomena*, **185**, 85 (2012).

E. Darlatt, A. Nefedov, C. Traulsen, J. Poppenberg, S. Richter, P. M. Dietrich, A. Lippitz, R. Illgen, J. Kühn, C. A. Schalley, Wolfgang E. S. Unger. Interpretation of experimental N K NEXAFS of azide, 1,2,3-triazole and terpyridyl groups by DFT spectrum simulations. *Journal of Electron Spectroscopy and Related Phenomena*, **185**, 621 (2012).

Conference proceedings

S. Linke, J. Kühn, K. Nörthemann, W. E. S. Unger and W. Moritz. Sensor high-throughput screening using photocurrent measurements in silicon.
Procedia engineering, **47**, 1195 (2012).

Talks

J. Kühn, A. Lippitz, M. Gorgoi. K. Nörthemann and W. E. S. Unger. Composition and chemistry of a ternary palladium thin film alloy studied by HAXPES, AES, XPS and EDX after hydrogen sulfide poisoning. *HAXPES 2013 - 5^{th} international conference on hard X-ray photoelectron spectroscopy*, Uppsala, Sweden, (2013).

J. Kühn, A. Lippitz, M. Gorgoi, K. Nörthemann and W. E. S. Unger. Composition and Chemistry of Pd-Ni-Co thin film alloy studied by HAXPES. *DPG-Frühjahrstagung der Sektion Kondensierter Materie (SKM), DS 30: Thin Film Characterization: Structure Analysis and Composition II*, Regensburg, Germany, (2013).

J. Kühn, T. Wirth, S. Linke, W. Moritz and W. E. S. Unger, High-throughput surface analysis of catalyst libraries based on ternary Pd thin film alloys. *PHI European Users Meeting 2012*, Eibelstadt, Germany (2012).

J. Kühn, S. Wasserroth, A. Lippitz, T. Gross, M. Gorgoi, S. Linke, W. Moritz and W. E. S. Unger. Chemical Depth Profiles of Ternary Pd alloys by HAXPES and first spectra simulations. 76. *Jahrestagung der DPG und DPG-Frühjahrstagung, DS 18: Thin Film Characterization: Structure Analysis and Composition (Spectroscopy)*, Berlin, Germany (2012).

Posters

J. Kühn, A. Lippitz, M. Gorgoi, K. Nörthemann, W. Moritz and W. E. S. Unger. Composition and Chemistry of a Pd-Ni-Co alloy studied by HAXPES. *15. JCF-Frühjahrsymposium*, Berlin, Germany (2013).

J. Kühn, A. Lippitz, M. Gorgoi, K. Nörthemann, W. Moritz and W. E. S. Unger. Composition and Chemistry of a Pd-Ni-Co alloy studied by HAXPES. HZB Users' Meeting, Berlin, Germany (2012).

S. Linke, J. Kühn, K. Nörthemann, W. E. S. Unger and W. Moritz, Sensor High-throughput screening using photocurrentmeasurements in silicon. *Eurosensors*, Krakau, Poland (2012).

J. Kühn, S. Wasserroth, . Wirth, S. Linke, W. Moritz, W. E. S. Unger. A comprehensive Auger electron spectroscopy study on a $Pd_xNi_yCo_{1-x-y}/LaF_3/SiO_2/Si$ multi-layer system for H_2 detection. *2. Berliner Chemie Symposium*, Berlin, Germany (2012).

J. Kühn, A. Lippitz, T. Gross, M. Gorgoi, S. Linke, W. Moritz and W. E. S. Unger. Chemical Depth Profiles of Ternary Pd Alloys by HAXPES and First Spectra Simulations. *HZB Users' Meeting*, Berlin, Germany (2011).

J. Kühn, A. Lippitz, M. Gorgoi, S. Linke, W. Moritz and W. E. S. Unger. A HAXPES Study of a Ternary Palladium Alloy Metal-Electrolyte-Insulator-Semiconductor System. *HAXPES 2011 - 4^{th} International Workshop on Hard-X-ray Photoelectron Spectroscopy*, Hamburg, Germany (2011).

J. Kühn, S. Linke, W. Moritz and W. E. S. Unger. Catalytic Properties of Pd-Ni-Co Alloy Thin Films used as Active Layer of a Hydrogen Sensor. *ECASIA 2011 - 14th Conference on Applications of Surface and Interface Analysis*, Cardiff, Wales (2011).

S. Linke, J. Kühn, W. Moritz and S. Krause. Catalytic properties of continuous gradient ternary palladium alloys. *SEMS Graduate Research Show*, London, Great Britain, (2011).

J. Kühn, V.-D. Hodoroaba, S. Linke, W. Moritz, W. E. S. Unger. Characterization of Pd-Ni-Co Alloy Thin Films by ED-EPMA and Data Reduction by the STRATAGEM Software. *IUMAS 2011 - 5th International Union of Microbeam Analysis Societies*, Seoul, South Korea (2011).

Posters - other contributions

E. Darlatt, J. Kühn, J. Poppenberg, S. Richter, C. Traulsen, C. A. Schalley and W. E. S. Unger. Buried interface characterization for a click chemistry-derivatized self assembled monolayer on gold, *HAXPES 2011 - 4th International Workshop on Hard-X-ray Photoelectron Spectroscopy*, Hamburg, Germany (2011).

Acknowledgements

Ich danke...

Prof. Thorsten Ressler für die Betreuung dieser Arbeit seitens der TU Berlin.
Dr. Wolfgang E. S. Unger für die Möglichkeit zur Doktorarbeit an der BAM.

Dr. Paul M. Dietrich (BAM) und Dr. Gerald V. Troppenz (HZB) für Motivation und die Korrektur des Manuskripts.

Dr. S. Linke (HUB) und Dr. K. Nörthemann (HUB) für die Herstellung und die Gasbehandlung der Legierungsbibliotheken.

Allen Kollegen der Arbeitsgruppe 6.8 für die freundliche Arbeitsatmosphäre.
Insbesondere den Gerätebetreuern T. Wirth (AES), D. Treu (XPS),
S. Benemann (SEM) und Dr. V.-D. Hodoroaba für die Einführung in EDX.

A. Lippitz (BAM) und Dr. M. Gorgoi (HZB) für die Unterstützung bei den HAX-PES Strahlzeiten. U. Banach (BAM) für Gasbehandlung von Proben und I. Dörfel (BAM) für die TEM-Studie. S. Wasserroth (FUB) für die engagierte Mitarbeit als Forschungspraktikant.

Meinen Weggefährten für die angenehme Zeit zusammen: Dr. Germar Eisenacher, DI Dr. Markus Holzweber und Prof. Pierre-Luc Girard-Lauriault.

Nele dafür, dass sie immer an mich geglaubt hat!

Eidesstattliche Versicherung

Hiermit versichere ich an Eides statt, dass ich die vorliegende Arbeit selbstständig verfasst und keine anderen als die in der Dissertation angegebenen Quellen und Hilfsmittel benutzt habe. Alle Ausführungen, die anderen veröffentlichten oder nicht veröffentlichten Schriften wörtlich oder sinnhaft entnommen wurden, habe ich kenntlich gemacht.

Die Arbeit hat in gleicher oder ähnlicher Fassung noch keiner anderen Prüfungsbehörde vorgelegen.

Julius Kühn

Berlin, den

Abbreviations and symbols

AES	Auger Electron Spectroscopy
AMRSF	Average matrix relative sensitivity factor
APPH	Auger peak-to-peak height
BAM	Bundestanstalt für Materialforschung und -prüfung
BCF	Backscattering Correction Factor
CMA	Cylindrical Mirror Analyzer
DFT	Density Functional Theory
E_{bin}	Binding energy (eV)
EBV	Electron Beam Voltage
ED-EPMA	Energy Dispersive - Electron Probe Microanalysis
EDX	Energy Dispersive X-ray Spectroscopy
ERSF	Elemental Relative Sensitivity Factors
ESCA	Electron Spectroscopy for Chemical Analysis
Eq.	Equation
FIB	Focused Ion Beam
Fig.	Figure
FRR	Fixed Retarding Ratio
FWHM	Full Width at Half Maximum
HAXPES	Hard X-ray Photoelectron Spectroscopy
HIKE	High Kinetic Energy
HTS	High-Throughput Screening
HUB	Humboldt-Universität Berlin
HZB	Helmholtz-Zentrum Berlin für Materialien und Energie
ID	Information Depth
IMFP	Inelastic Mean Free Path
ISO	International Organization for Standardization
MC	Monte Carlo
MED	Mean Escape Depth
MEIS	Metal Electrolyte Insulator Semiconductor

ML	MonoLayer
NIST	National Institute of Standards and Technology
PERSF	Pure Element Relative Sensitivity Factor
PES	Photoelectron Spectroscopy
RSF	Relative Sensitivity Factor
S9D5	9-point Savitzky-Golay Smooth and 5-point Differentiation.
SED	Secondary Electron Detector
SEM	Scanning Electron Microscopy
SESSA	Simulation of Electron Spectra for Surface Analysis
syn	synthetic
TEM	Transmission Electron Microscopy
u_c	combined uncertainty
UHV	Ultra-High Vacuum
XPS	X-ray Photoelectron Spectroscopy
X	atomic concentration (at.%)
Z	atomic number

References

[1] B. D. Adams and A. Chen. The role of palladium in a hydrogen economy. *Materials Today*, **14**, 282 (2011).

[2] S. Yun and S. Ted Oyama. Correlations in palladium membranes for hydrogen separation: A review. *Journal of Membrane Science*, **375**, 28 (2011).

[3] T. Peters, et al. Development of thin binary and ternary Pd-based alloy membranes for use in hydrogen production. *Journal of Membrane Science*, **383**, 124 (2011).

[4] A. M. Tarditi and L. M. Cornaglia. Novel PdAgCu ternary alloy as promising materials for hydrogen separation membranes: Synthesis and characterization. *Surface Science*, **605**, 62 (2011).

[5] L. Schlapbach and A. Zuttel. Hydrogen-storage materials for mobile applications. *Nature*, **414**, 353 (2001).

[6] S. Yagi, et al. Spectral studies on sulfur poisoning of Pd/Mg_6Ni by NEXAFS and XPS. *Applied Surface Science*, **267**, 45 (2013).

[7] E. Antolini. Palladium in fuel cell catalysis. *Energy & Environmental Science*, **2**, 915 (2009).

[8] B. Morreale, et al. Effect of hydrogen-sulfide on the hydrogen permeance of palladium-copper alloys at elevated temperatures. *Journal of Membrane Science*, **241**, 219 (2004).

[9] B. Howard, et al. Hydrogen permeance of palladium-copper alloy membranes over a wide range of temperatures and pressures. *Journal of Membrane Science*, **241**, 207 (2004).

[10] W. F. Maier, K. Stöwe, and S. Sieg. Combinatorial and High-Throughput materials science. *Angewandte Chemie International Edition*, **46**, 6016 (2007).

[11] R. Potyrailo, et al. Combinatorial and high-throughput screening of materials libraries: Review of state of the art. *ACS Comb. Sci.*, **13**, 579 (2011).

[12] S. Curtarolo, et al. The high-throughput highway to computational materials design. *Nature Materials*, **12**, 191 (2013).

[13] S. Guerin and B. E. Hayden. Physical vapor deposition method for the high-throughput synthesis of solid-state material libraries. *Journal of Combinatorial Chemistry*, **8**, 66 (2006).

[14] M. L. Green, I. Takeuchi, and J. R. Hattrick-Simpers. Applications of high throughput (combinatorial) methodologies to electronic, magnetic, optical, and energy-related materials. *Journal of Applied Physics*, **113**, 231101 (2013).

[15] D. Priyadarshini, et al. High-Throughput characterization of surface segregation in Cu_xPd_{1-x} alloys. *J. Phys. Chem. C*, **115**, 10155 (2011).

[16] J. B. Miller, D. Priyadarshini, and A. J. Gellman. Segregation at the surfaces of Cu_xPd_{1-x} alloys in the presence of adsorbed S. *Surface Science*, **606**, 1520 (2012).

[17] S. Linke, et al. Low energy hydrogen sensor. *International Journal of Hydrogen Energy*, **37**, 17523 (2012).

[18] W. Moritz, R. Werner, A. Tausche, G. Cherkaschinin, R. Molajew, T. Wirth, W. E. S. Unger and S. Linke. Alloys for Gas Sensors Investigated Using the Continuous Gradient - High Throughput Screening Macroscope CG-HTSM. *Sensor Letters*, **9**, 662 (2011).

[19] S. Linke. *Laser scanning system for microscopic and macroscopic investigations of chemical semiconductor-sensors, PhD-Thesis.* Queen Mary University London (2012).

[20] K. D. Childs, et al. *Handbook of Auger Electron Spectroscopy.* Physical Electronics, Inc., 3rd edition (1995).

[21] D. Briggs and M. P. Seah. *Practical Surface Analysis Volume 1 - Auger and X-ray Photoelectron Spectroscopy.* Wiley, 2nd edition (1990).

[22] D. Briggs and J. Grant. *Surface Analysis by Auger and X-ray Photoelectron Spectroscopy.* IM Publications (2003).

[23] J. C. Vickerman and I. S. Gilmore, editors. *Surface analysis: the principal techniques*. Wiley, 2nd edition (2009).

[24] S. Hofmann. *Auger- and X-Ray Photoelectron Spectroscopy in Materials Science*. Springer, 1st edition (2013).

[25] P. Auger. Secondary beta-rays produced in a gas by X-rays. *Comptes Rendus Hebdomadaires des Seances de l'Academie des Sciences*, **177**, 169 (1923).

[26] P. Auger. The compound photoelectric effect. *Journal de Physique et le Radium*, **6**, 205 (1925).

[27] P. Auger. Compound photoelectric effect. *Annales de Physique*, **6**, 183 (1926).

[28] P. Auger. The Auger effect. *Surface Science*, **48**, 1 (1975).

[29] L. Meitner. Das β-Strahlenspektrum von UX1 und seine Deutung. *Zeitschrift für Physik*, **17**, 54 (1923).

[30] M. Chung and L. Jenkins. Auger electron energies of the outer shell electrons. *Surface Science*, **22**, 479 (1970).

[31] W. Coghlan and R. Clausing. Auger catalog calculated transition energies listed by energy and element. *Atomic Data and Nuclear Data Tables*, **5**, 317 (1973).

[32] A. Jablonski. Quantification of surface-sensitive electron spectroscopies. *Surface Science*, **603**, 1342 (2009).

[33] *ISO 18115-1, Surface Chemical Analysis - Vocabulary, Part 1 - General Terms and Terms Used in Spectroscopy*. ISO International Organization for Standardization, Geneva (2010).

[34] C. J. Powell, et al. Surface sensitivity of Auger-electron spectroscopy and X-ray photoelectron spectroscopy. *Journal of Electron Spectroscopy and Related Phenomena*, **98-99**, 1 (1999).

[35] A. Jablonski and C. J. Powell. Information depth and the mean escape depth in Auger electron spectroscopy and X-ray photoelectron spectroscopy. *Journal of Vacuum Science & Technology A*, **21**, 274 (2003).

[36] S. Tanuma, C. J. Powell, and D. R. Penn. Calculations of electron inelastic mean free paths. IX. Data for 41 elemental solids over the 50 eV to 30 keV range. *Surface and Interface Analysis*, **43**, 689 (2011).

[37] M. P. Seah, et al. Quantitative AES V. practical analysis of intensities with detailed examples of metals and their oxides. *Surface and Interface Analysis*, **26**, 701 (1998).

[38] C. Chang. General formalism for quantitative Auger analysis. *Surface Science*, **48**, 9 (1975).

[39] P. Holloway. Quantitative Auger electron analysis of homogeneous binary alloys: Chromium in gold. *Surface Science*, **66**, 479 (1977).

[40] P. Hall, J. Morabito, and D. Conley. Relative sensitivity factors for quantitative Auger analysis of binary alloys. *Surface Science*, **62**, 1 (1977).

[41] P. Hall and J. Morabito. Matrix effects in quantitative Auger analysis of dilute alloys. *Surface Science*, **83**, 391 (1979).

[42] T. Wirth. Quantitative Auger electron spectroscopy of silicides by extended matrix correction using dN(E)/dE spectra. *Surface and Interface Analysis*, **18**, 3 (1992).

[43] H. Shimizu, M. Ono, and K. Nakayama. Quantitative Auger analysis of copper-nickel alloy surfaces after argon ion bombardment. *Surface Science*, **36**, 817 (1973).

[44] T. Sekine, K. Hirata, and A. Mogami. Matrix effect correction in quantitative Auger electron spectroscopy. *Surface Science*, **125**, 565 (1983).

[45] A. Jablonski and C. Powell. Dependence of the AES backscattering correction factor on the experimental configuration. *Surface Science*, **604**, 1928 (2010).

[46] R. Shimizu. Quantitative Analysis by Auger Electron Spectroscopy. *Japanese Journal of Applied Physics*, **22**, 1631 (1983).

[47] A. Jablonski and C. Powell. *NIST Backscattering-Correction-Factor Database for Auger Electron Spectroscopy: Version 1.0*. National Institute of Standards and Technology (2011).

[48] D. Bote, et al. Cross sections for ionization of K, L and M shells of atoms by impact of electrons and positrons with energies up to 1 GeV: Analytical formulas. *Atomic Data and Nuclear Data Tables*, **95**, 871 (2009).

[49] A. Jablonski, F. Salvat, and C. Powell. *NIST Electron Elastic-Scattering Cross-Section Database: Version 3.2* . National Institute of Standards and Technology (2010).

[50] A. Jablonski, S. Tanuma, and C. J. Powell. Modified predictive formula for the electron stopping power. *Journal of Applied Physics*, **103** (2008).

[51] E. Casnati, A. Tartari, and C. Baraldi. An empirical approach to K-shell ionisation cross section by electrons. *Journal of Physics B: Atomic and Molecular Physics*, **15**, 155 (1982).

[52] M. Gryzinski. Classical Theory of Atomic Collisions. I. Theory of Inelastic Collisions. *Physical Review*, **138**, A336 (1965).

[53] *ISO 18118, Surface Chemical Analysis - Auger electron spectroscopy and X-ray photoelectron spectroscopy - Guide to the use of experimentally determined relative sensitivity factors for the quantitative analysis of homogeneous materials.* ISO International Organization for Standardization, Geneva (2004).

[54] *PHI MultiPak^{TM} Software Manual Version 9.* ULVAC-PHI, Inc. (2010).

[55] K. J. Kim, et al. Inter-laboratory comparison: Quantitative surface analysis of thin Fe-Ni alloy films. *Surface and Interface Analysis*, **44**, 192 (2012).

[56] M. P. Seah and I. S. Gilmore. Quantitative AES. VIII: Analysis of Auger electron intensities from elemental data in a digital Auger database. *Surface and Interface Analysis*, **26**, 908 (1998).

[57] C. Powell. *NIST Database for the Simulation of Electron Spectra for Surface Analysis (SESSA): Version 1.3.* National Institute of Standards and Technology (2011).

[58] M. P. Seah and I. S. Gilmore. Simplified equations for correction parameters for elastic scattering effects in AES and XPS for q, β and attenuation lengths. *Surface and Interface Analysis*, **31**, 835 (2001).

[59] J. Goldstein, et al. *Scanning Electron Mircroscopy and X-ray Microanalysis.* Kluwer Academic / Plenum Publishers, 3rd edition (2003).

[60] R. Jenkins, et al. IUPAC-nomenclature system for X-ray spectroscopy. *X-Ray Spectrometry*, **20**, 149 (1991).

[61] D. Drouin, et al. CASINO V2.42 - A Fast and Easy-to-use Modeling Tool for Scanning Electron Microscopy and Microanalysis Users. *Scanning*, **29**, 92 (2007).

[62] V.-D. Hodoroaba, K. J. Kim, and W. E. S. Unger. Energy dispersive electron probe microanalysis (ED-EPMA) of elemental composition and thickness of Fe-Ni alloy films. *Surface and Interface Analysis*, **44**, 1459 (2012).

[63] J. Kühn, et al. Characterization of Pd-Ni-Co alloy thin films by ED-EPMA with application of the STRATAGEM software. *Surface and Interface Analysis*, **44**, 1456 (2012).

[64] W. Drube. Photoelectron spectroscopy with hard X-rays. *Nuclear Instruments and Methods in Physics Research Section A: Accelerators, Spectrometers, Detectors and Associated Equipment*, **547**, 87 (2005).

[65] C. Fadley. X-ray photoelectron spectroscopy: Progress and perspectives. *Journal of Electron Spectroscopy and Related Phenomena*, **178-179**, 2 (2010).

[66] H. R. Hertz. Über den Einfluss des ultravioletten Lichtes auf die elektrische Entladung. *Annalen der Physik*, **267**, 983 (1887).

[67] A. Einstein. Über einen die Erzeugung und Verwandlung des Lichtes betreffenden heuristischen Gesichtspunkt. *Annalen der Physik*, **322**, 132 (1905).

[68] J. Yeh and I. Lindau. Atomic subshell photoionization cross sections and asymmetry parameters: $1 < Z < 103$. *Atomic Data and Nuclear Data Tables*, **32**, 1 (1985).

[69] M. B. Trzhaskovskaya, V. I. Nefedov, and V. G. Yarzhemsky. Photoelectron angular distribution parameters for elements Z=1 to Z=54 in the photoelectron energy range 100-5000 eV. *Atomic Data and Nuclear Data Tables*, **77**, 97 (2001).

[70] M. B. Trzhaskovskaya, et al. Non-dipole second order parameters of the photoelectron angular distribution for elements Z = 1-100 in the photoelectron energy range 1-10 keV. *Atomic Data and Nuclear Data Tables*, **92**, 245 (2006).

[71] J. H. Scofield. *Theoretical photoinonization cross sections from 1-1500 keV*. Lawrence Livermore Laboratory (1973).

[72] C. Nordling, E. Sokolowski, and K. Siegbahn. Precision method for obtaining absolute values of atomic binding energies. *Physical Review*, **105**, 1676 (1957).

[73] N. Mårtensson, E. Sokolowski, and S. Svensson. 50 years anniversary of the discovery of the core level chemical shifts. The early years of photoelectron spectroscopy. *Journal of Electron Spectroscopy and Related Phenomena*, **193**, 27 (2014).

[74] K. Kobayashi, M. Kobata, and H. Iwai. Development of a laboratory system hard X-ray photoelectron spectroscopy and its applications. *Journal of Electron Spectroscopy and Related Phenomena*, **190, Part B**, 210 (2013).

[75] *ISO 15742, Surface chemical analysis - X-ray photoelectron spectrometers Calibration of energy scales*. ISO International Organization for Standardization, Geneva (2010).

[76] F. Schaefers, M. Mertin, and M. Gorgoi. KMC-1: A high resolution and high flux soft X-ray beamline at BESSY. *Review of Scientific Instruments*, **78**, 123102 (2007).

[77] M. Gorgoi, et al. The high kinetic energy photoelectron spectroscopy facility at BESSY progress and first results. *Nuclear Instruments and Methods in Physics Research Section A: Accelerators, Spectrometers, Detectors and Associated Equipment*, **601**, 48 (2009).

[78] W. Fredriksson, et al. Full depth profile of passive films on 316L stainless steel based on high resolution HAXPES in combination with ARXPS. *Applied Surface Science*, **258**, 5790 (2012).

[79] D. J. Miller, M. C. Biesinger, and N. S. McIntyre. Interactions of CO_2 and CO at fractional atmosphere pressures with iron and iron oxide surfaces: One possible mechanism for surface contamination? *Surface and Interface Analysis*, **33**, 299 (2002).

[80] *ISO 19318, Surface chemical analysis - X-ray photoelectron spectroscopy - Reporting of methods used for charge control and charge correction* . ISO International Organization for Standardization, Geneva (2004).

[81] Y. Takata, et al. Recoil effects of photoelectrons in a solid. *Physical Review B*, **75**, 233404 (2007).

[82] J. Vegh. The Shirley background revised. *Journal of Electron Spectroscopy and Related Phenomena*, **151**, 159 (2006).

[83] J. F. Moulder, et al. *Handbook of X-ray Photoelectron Spectroscopy*. Physical Electronics, Inc. (1995).

[84] N. Mårtensson, R. Nyholm, and B. Johansson. Chemical-shift effects and origin of the Pd 3d core-level satellite in CuPd alloys. *Physical Review Letters*, **45**, 754 (1980).

[85] S. Hüfner. *Photoelectron Spectroscopy - Principles and Applications*. Springer (2003).

[86] O. Karis, et al. High-kinetic-energy photoemission spectroscopy of Ni at 1s: 6-eV satellite at 4 eV. *Physical Review B*, **78**, 233105 (2008).

[87] R. Hesse, P. Streubel, and R. Szargan. Product or sum: comparative tests of Voigt, and product or sum of Gaussian and Lorentzian functions in the fitting of synthetic Voigt-based X-ray photoelectron spectra. *Surface and Interface Analysis*, **39**, 381 (2007).

[88] S. Doniach and M. Sunjic. Many-electron singularity in X-ray photoemission and X-ray line spectra from metals. *Journal of Physics C: Solid State Physics*, **3**, 285 (1970).

[89] J. H. Scofield. Hartree-slater subshell photoionization cross-sections at 1254 and 1487 eV. *Journal of Electron Spectroscopy and Related Phenomena*, **8**, 129 (1976).

[90] M. Procop. EDXTOOLS - Computer Programmes for the Determination of Critical EDX Spectrometer Parameters. *Mikrochimica Acta*, **132**, 527 (2000).

[91] J. L. Pouchou and F. Pichoir. *Electron Probe Quantitation*. (K. F. J. Heinrich and D. E. Newbury, eds.), Plenum Press, New York, p. 31 (1991).

[92] K. J. Kim, et al. Quantitative surface analysis of Fe-Ni alloy films by XPS, AES and SIMS. *Surface and Interface Analysis*, **39**, 665 (2007).

[93] K. J. Kim, et al. Final report on key comparison K67 and parallel pilot study P108: Measurement of composition of a thin Fe-Ni alloy film. *Metrologia*, **47**, 08011 (2010).

[94] A. V. Ruban, H. L. Skriver, and J. K. Nørskov. Surface segregation energies in transition-metal alloys. *Physical Review B*, **59**, 15990 (1999).

[95] O. Løvvik. Surface segregation in palladium based alloys from density-functional calculations. *Surface Science*, **583**, 100 (2005).

[96] J. H. Los, C. Mottet, and G. Treglia. Surface segregation trends in transition metal alloys. *Physical Review B*, **88**, 165408 (2013).

[97] J. Luyten, S. Helfensteyn, and C. Creemers. Segregation in ternary alloys: an interplay of driving forces. *Applied Surface Science*, **212-213**, 833 (2003).

[98] F. L. Williams and D. Nason. Binary alloy surface compositions from bulk alloy thermodynamic data. *Surface Science*, **45**, 377 (1974).

[99] A. Jablonski. The surface composition of binary metal alloys. The regular solution theory. *Advances in Colloid and Interface Science*, **8**, 213 (1977).

[100] H. Bonzel, editor. *Landolt Börnstein. Numerical data and Functional Relationships in Science and Technology. Group III: Condensed Mater. Volume 42: Physics of Covered Solid Surfaces. Subvolume A: Adsorbed Layers on Surfaces. Part 3: Surface Segregation and Adsorption on Surface*. Springer (2003).

[101] C. Stoddart, R. Moss, and D. Pope. Determination of the surface composition of palladium-nickel alloy film catalysts using Auger electron spectroscopy. *Surface Science*, **53**, 241 (1975).

[102] S. Helfensteyn, et al. Modeling surface phenomena in Pd-Ni alloys. *Applied Surface Science*, **212-213**, 844 (2003).

[103] M. Krawczyk, et al. Surface composition of the CoPd alloys studied by electron spectroscopies. *Surface and Interface Analysis*, **25**, 356 (1997).

[104] I. G. Batirev and J. A. Leiro. Surface segregation of PdRh, PdNi and PdCo alloys. *Journal of Electron Spectroscopy and Related Phenomena*, **71**, 79 (1995).

[105] M. Green. Lectures on gas-solid interactions. *Sensors and Actuators*, **1**, 379 (1981).

[106] M. Krawczyk. Oxygen adsorption on binary $Co_{50}Pd_{50}$ alloy surfaces. *Vacuum*, **63**, 23 (2001).

[107] J. Mingrong, et al. Oxygen adsorption on the $Co_{50}Ni_{50}(111)$ surface. *Applied Surface Science*, **55**, 203 (1992).

[108] Y. Law, T. Dintzer, and S. Zafeiratos. Surface oxidation of NiCo alloy: A comparative X-ray photoelectron spectroscopy study in a wide pressure range. *Applied Surface Science*, **258**, 1480 (2011).

[109] O. Løvvik and S. M. Opalka. Reversed surface segregation in palladium-silver alloys due to hydrogen adsorption. *Surface Science*, **602**, 2840 (2008).

[110] A. A. B. Padama, H. Kasai, and Y. W. Budhi. Hydrogen absorption and hydrogen-induced reverse segregation in palladium-silver surface. *International Journal of Hydrogen Energy*, **38**, 14715 (2013).

[111] I. H. Svenum, et al. Adsorbate-induced segregation in a PdAg membrane model system: $Pd_3Ag(111)$. *Catalysis Today*, **193**, 111 (2012).

[112] J. B. Miller, B. D. Morreale, and A. J. Gellman. The effect of adsorbed sulfur on surface segregation in a polycrystalline $Pd_{70}Cu_{30}$ alloy. *Surface Science*, **602**, 1819 (2008).

[113] D. R. Lide, editor. *Handbook of Chemistry and Physics*. CRC Press (2005).

[114] K. J. Andersson, et al. Adsorption-driven surface segregation of the less reactive alloy component. *Journal of the American Chemical Society*, **131**, 2404 (2009).

[115] J. K. Nørskov, et al. Origin of the overpotential for oxygen reduction at a fuel-cell cathode. *The Journal of Physical Chemistry B*, **108**, 17886 (2004).

[116] H. Mönig, et al. Surface Cu depletion of $Cu(In,Ga)Se_2$ films: An investigation by hard X-ray photoelectron spectroscopy. *Acta Materialia*, **57**, 3645 (2009).

[117] B. Philippe, et al. Nanosilicon Electrodes for Lithium-Ion Batteries: Interfacial Mechanisms Studied by Hard and Soft X-ray Photoelectron Spectroscopy. *Chem. Mater.*, **24**, 1107 (2012).

[118] F. U. Hillebrecht, et al. Electronic structure of Ni and Pd alloys. II. X-ray photoelectron core-level spectra. *Physical Review B*, **27**, 2179 (1983).

[119] W. Xu, et al. Tailoring supported palladium sulfide catalysts through H_2-assisted sulfidation with H_2S. *Journal of Materials Chemistry A*, **1**, 12811 (2013).

[120] M. Brun, A. Berthet, and J. C. Bertolini. XPS, AES and Auger parameter of Pd and PdO. *Journal of Electron Spectroscopy and Related Phenomena*, **104**, 55 (1999).

[121] L. Kibis, et al. X-ray photoelectron spectroscopy study of Pd oxidation by RF discharge in oxygen. *Applied Surface Science*, **255**, 9248 (2009).

[122] A. P. Grosvenor, et al. New interpretations of XPS spectra of nickel metal and oxides. *Surface Science*, **600**, 1771 (2006).

[123] B. P. Payne, et al. Structure and growth of oxides on polycrystalline nickel surfaces. *Surface and Interface Analysis*, **39**, 582 (2007).

[124] B. Payne, M. Biesinger, and N. McIntyre. The study of polycrystalline nickel metal oxidation by water vapour. *Journal of Electron Spectroscopy and Related Phenomena*, **175**, 55 (2009).

[125] B. Payne, M. Biesinger, and N. McIntyre. Use of oxygen/nickel ratios in the XPS characterisation of oxide phases on nickel metal and nickel alloy surfaces. *Journal of Electron Spectroscopy and Related Phenomena*, **185**, 159 (2012).

[126] M. C. Biesinger, et al. X-ray photoelectron spectroscopic chemical state quantification of mixed nickel metal, oxide and hydroxide systems. *Surface and Interface Analysis*, **41**, 324 (2009).

[127] J. Yang, et al. Synthesis and characterization of cobalt hydroxide, cobalt oxyhydroxide, and cobalt oxide nanodiscs. *The Journal of Physical Chemistry C*, **114**, 111 (2010).

[128] M. C. Biesinger, et al. Resolving surface chemical states in XPS analysis of first row transition metals, oxides and hydroxides: Cr, Mn, Fe, Co and Ni. *Applied Surface Science*, **257**, 2717 (2011).

[129] J. Sundberg, et al. Understanding the effects of sputter damage in W-S thin films by HAXPES. *Applied Surface Science*, **305**, 203 (2014).

[130] H. Yoshikawa, I. Matolinova, and V. Matolin. Practical chemical analysis of Pt and Pd based heterogeneous catalysts with hard X-ray photoelectron spectroscopy. *Journal of Electron Spectroscopy and Related Phenomena*, **190, Part B**, 268 (2013).